



© Copyright by Tian Gu 2016  
All Rights Reserved

# **Spatio-temporal Dynamics of Reaction Zones in Catalytic Monolith Reactors**

A Dissertation

Presented to

the Faculty of the Department of Chemical and Biomolecular Engineering

University of Houston

In Partial Fulfillment

of the Requirements for the Degree

Doctor of Philosophy

in Chemical Engineering

by

Tian Gu

August 2016

# **Spatio-temporal Dynamics of Reaction Zones in Catalytic Monolith Reactors**

---

Tian Gu

Approved:

---

Chair of the Committee  
Vemuri Balakotaiah, Professor,  
Chemical and Biomolecular Engineering

---

Co-Chair of the Committee  
Matthew A. Franchek, Professor,  
Mechanical Engineering

---

Co-Chair of the Committee  
Karolos Grigoriadis, Professor,  
Mechanical Engineering

Committee Members:

---

William Epling, Professor,  
Chemical and Biomolecular Engineering

---

Michael Nikolaou, Professor,  
Chemical and Biomolecular Engineering

---

Suresh K. Khator, Associate Dean,  
Cullen College of Engineering

---

Michael P. Harold, Professor and Chair  
Chemical and Biomolecular Engineering

## Acknowledgements

First and foremost, I would like to express my sincere gratitude to my advisors, Professors Vemuri Balakotaiah, Matthew Franchek and Karolos Grigoriadis, for their continued support and guidance during the course of this work. Prof. Balakotaiah has been extraordinarily generous with his time, providing not only his deep knowledge and rich experiences in reaction engineering, but also valuable life and career advices. Prof. Franchek has resourcefully provided fresh perspectives to help my research and shown me how to better communicate with people. With his strong expertise in control systems, Prof. Grigoriadis helps bring the research closer to practical applications.

I am thankful to the committee members, Professors William Epling and Michael Nikolaou, for taking the time off their busy schedule and offering valuable comments. I am also grateful to my internship supervisor, Dr. Syed Wahiduzzaman at Gamma Technologies for offering the opportunity and providing his generous help. I would like to acknowledge National Science Foundation and Qatar National Research Fund for the financial support. I am also thankful to the Graduate Coordinator, Miranda Vernon-Harrison, the staff of the Department of Chemical and Biomolecular Engineering, especially Patricia Cooks, Pamela Moses, Yolanda Thomas and My-Dung Lieu, for their patient help in administration.

I would like to thank all my past and present co-workers for all of their help and support. Especially, I wish to express my sincere thanks to Imran Alam for our innumerable lunches together which are always accompanied by intellectually stimulating discussions on every aspect of our lives. I am thankful to Arun Kota for sharing an office with me and answering too many questions of mine in a gentleman's

way. I would also like to thank Pankaj Kumar who patiently answered my questions through emails and helped me jump start my research and Ram Ratnakar who helped me prepare for interviews and provided valuable career advices. Other senior members of the group: Santhosh Gundlapally, Bijesh Shakya, Richa Raj and Priyank Maheshwari also deserve special appreciation for giving me suggestions about research and career. I also want to thank junior colleagues: Rama Krishna Dadi, Zhe Sun and Allen Ting for keeping a great atmosphere in the lab and for sharing their time with me.

During my Ph.D. study, I've lost two loved ones to diseases, my grandfather Fengxiang Gu and my dear friend Fu Zhao. I would not be who I am today without them. I will gratefully cherish the memories of them.

Finally, I would like to express my love and gratitude to my parents, Yunfeng Gu and Min Su, and other family members for their constant support and encouragement from the other side of the world. Words fail to express my gratitude towards my beloved girlfriend, Chi Zhang, who makes my world colorful and my life worthwhile.

# **Spatio-temporal Dynamics of Reaction Zones in Catalytic Monolith Reactors**

An Abstract

of a

Dissertation

Presented to

the Faculty of the Department of Chemical and Biomolecular Engineering

University of Houston

In Partial Fulfillment

of the Requirements for the Degree

Doctor of Philosophy

in Chemical Engineering

by

Tian Gu

August 2016

## Abstract

Catalytic monolith reactors are widely used in exhaust after-treatment systems. Unlike traditional chemical reactors which are commonly operated around certain steady-states, monolith reactors are almost always in transient states due to the nature of their applications. In this work, we studied the spatio-temporal dynamics of monolith reactors in three important cases, in order to provide guidance for improving the design and control of after-treatment systems.

In the first part, a physics-based one-dimensional transient model is proposed to study the spatio-temporal oxygen storage and release as well as the cold-start behavior of a three-way catalytic converter (TWC). As shown in this work, axial gradients in the temperature and stored oxygen profile cannot be neglected during cold-start, fast lean/rich cycling or sudden and significant changes in the inlet conditions to the TWC. By comparing the results of this model with the full washcoat diffusion–reaction model, we have also shown that the internal mass transfer coefficient approximation is valid for all practical purposes.

In the second part, we investigated in detail three main reasons for failure of scale-up in monolith reactors: mass dispersion, heat conduction and heat loss. Monolith reactors are often studied in laboratory experiments using samples of the same properties except for a smaller length compared to the full-scale reactor. The common practice of matching the space time in lab- and full-scale systems results in unmatched axial mass and heat Péclet numbers and heat loss coefficient. It is shown that the unmatched dimensionless groups can lead to qualitatively different ignition/extinction behaviors in different scales.

In the third part, the upstream creeping reaction zone in monolith reactors is studied. When front-end ignition is technologically difficult or economically impractical, back-end ignition followed by a fast upstream creeping reaction zone provides a feasible way to reduce cold-start emissions. In this work, the influence of various design parameters (e.g., solid thermal conductivity, heat capacity) and operating conditions (e.g., gas velocity, inlet temperature and concentrations) on the creep velocity is determined and summarized. In the pseudo-homogeneous limit, analytical criteria for reaction zones to creep upstream and correlations for the creep velocity are also presented.

# Table of Contents

Acknowledgements.....	v
Abstract .....	viii
Table of Contents .....	x
List of Figures .....	xiii
List of Tables .....	xix
Nomenclature.....	xx
<b>Low-dimensional Modeling of a Three-way Catalytic Converter.....</b>	<b>1</b>
CHAPTER 1 Introduction and Literature Review.....	2
CHAPTER 2 Spatio-temporal Dynamics of Oxygen Storage and Release in a Three-way Catalytic Converter.....	6
2.1 Mathematical Model.....	7
2.2 Mass and Heat Transfer Correlations .....	11
2.3 Kinetic Model .....	14
2.4 Experimental Validation .....	15
2.5 Detailed Model Validation.....	25
2.6 Oxygen Storage Dynamics .....	30
2.7 Summary.....	36
<b>Scale-up Analysis of Monolith Reactors .....</b>	<b>37</b>
CHAPTER 3 Introduction and Literature Review.....	38
CHAPTER 4 Model Development .....	41
4.1 Two-dimensional Monolith Model.....	42
4.2 Dimensionless Groups .....	45

4.3	Simplified Models.....	50
4.3.1	One-dimensional Two-phase Monolith Model.....	50
4.3.2	Pseudo-homogeneous Model.....	54
CHAPTER 5 Impact of Heat and Mass Dispersion and Thermal Effects on the		
	Scale-up of Monolith Reactors .....	58
5.1	Impact of Mass Dispersion .....	58
5.1.1	Linear Kinetics.....	58
5.1.2	Nonlinear Kinetics .....	59
5.1.3	Cycling Performance .....	63
5.1.4	Estimation of Kinetic Parameters from Light-off Curves.....	65
5.2	Impact of Heat Conduction and Adiabatic Temperature Rise .....	70
5.2.1	Linear Kinetics.....	70
5.2.2	Nonlinear Kinetics .....	80
5.2.3	Plots of Exit Conversion versus Mid-bed Temperature.....	80
5.3	Impact of Interphase Gradients.....	86
5.4	Impact of Heat Loss .....	89
5.5	Summary.....	93
	<b>Creeping Reaction Zones in Monolith Reactors.....</b>	<b>98</b>
CHAPTER 6 Introduction and Literature Review .....		
		99
CHAPTER 7 Model Development .....		
		102
7.1	Detailed Washcoat Diffusion Model .....	102
7.2	Dimensionless Groups .....	105
7.3	Simplified Models.....	108

4.3.1	One-dimensional Two-phase Monolith Model .....	108
4.3.2	Pseudo-homogeneous Model .....	109
CHAPTER 8 Analysis of Upstream Creeping Reaction Zones in Monolith		
	Reactors .....	111
8.1	Transient Behavior of Monolith Reactors .....	111
8.2	Parametric Studies on Creep Velocity .....	116
8.2.1	Adiabatic Temperature Rise .....	116
8.2.2	Solid Thermal Conductivity .....	116
8.2.3	Solid Heat Capacity .....	119
8.2.4	Substrate Material .....	119
8.2.5	Reactor Length .....	122
8.2.6	Nonlinear Kinetics .....	122
8.3	Criteria for Upstream Creeping Reaction Zones .....	124
8.4	Correlation for Creep Velocity .....	130
8.5	Summary .....	134
CHAPTER 9 Conclusions and Recommendations for Future Work .....		
9.1	Conclusions .....	135
9.2	Recommendations for Future Work .....	136
REFERENCES .....		139

## List of Figures

Figure 2.1 Total carbon balance in terms of mole fractions at the TWC inlet and exit during bag 1 of an FTP cycle. ....	9
Figure 2.2 Model validation for oxidant emission at idle speed.....	18
Figure 2.3 Model validation of reductant emission at idle speed .....	19
Figure 2.4 (a) Vehicle speed, (b) inlet temperature and feed gas velocity over bag1 of an FTP cycle.....	22
Figure 2.5 Cumulative reductant emission comparison between 1-D model and 0-D model during (a) the first 100 seconds of and (b) the entire bag 1 of an FTP cycle.....	23
Figure 2.6 Model comparison of FOS predictions during the first 500 seconds of an FTP cycle .....	24
Figure 2.7 Transient temperature profiles following the cold start .....	24
Figure 2.8 Model comparison of reductant conversions.....	28
Figure 2.9 Model comparison of oxidant conversions.....	28
Figure 2.10 Model comparison of mid-bed temperatures.....	29
Figure 2.11 Model comparison of FOS dynamics under cold start condition. ....	31
Figure 2.12 Spatial FOS profile under cold start condition. ....	32
Figure 2.13 Model comparison of FOS dynamics during fast lean-rich cycling.....	34
Figure 2.14 Spatial FOS profile during fast lean-rich cycling.....	35
Figure 3.1 Schematic diagrams of (a) a lab-scale reactor and (b) a full-scale reactor.....	40

Figure 4.1 Schematic diagram of the cross-section of (a) a single monolith channel and (b) axisymmetric approximation for modeling..	42
Figure 5.1 Plot of steady-state exit conversion versus inlet temperature in isothermal reactors with first-order kinetics and different axial mass Péclet numbers ( $Pe_m$ ). ( $E_a = 100$ kJ/mol, $Da_0 = 10^{10}$ ).	60
Figure 5.2 Bifurcation diagrams of steady-state exit conversion versus inlet temperature for isothermal reactors with Langmuir-Hinshelwood kinetics and different axial mass Péclet numbers ( $Pe_m$ ). ( $E_a = 100$ kJ/mol, $Da_0^{LH} = 10^{10}$ , $\kappa=2000$ , $X^{in}=0.02$ )	62
Figure 5.3 Hysteresis loci of isothermal reactors with Langmuir-Hinshelwood kinetics and different adsorption equilibrium constants ( $\kappa$ ) in the ( $X^{in}$ , $Pe_m$ ) plane ( $E_a =$ $100$ kJ/mol, $Da_0^{LH} = 10^{10}$ )	64
Figure 5.4 Bifurcation diagrams of steady-state exit conversion versus inlet mole fraction for isothermal reactors with Langmuir-Hinshelwood kinetics and different axial mass Péclet numbers ( $Pe_m$ ). ( $E_a = 100$ kJ/mol, $Da_0^{LH} = 10^{10}$ , $\kappa=2000$ , $T^{in}$ $= 470$ K)	66
Figure 5.5 Light-off curves of cycle averaged exit conversion versus inlet temperature for isothermal reactors with Langmuir-Hinshelwood kinetics. ( $E_a = 100$ kJ/mol, $Da_0^{LH} = 10^{10}$ , $\kappa=2000$ , $\epsilon = 0.1$ , $X^{in}=0.02$ , $\epsilon_c=1$ )	67
Figure 5.6 (a) Percentage error in the estimated activation energy by assuming a PFR model and fitting data from reactors with first-order kinetics and different $Pe_m$ . (b) PFR model fitting data generated from a reactor with $Pe_m = 1$ . ( $E_a = 100$ kJ/mol, $Da_0 = 10^{10}$ )	69

Figure 5.7 Steady-state axial temperature profiles of adiabatic reactors with first-order kinetics and different axial heat Péclet numbers ( $Pe_h$ ). ( $E_a = 100$ kJ/mol, $Da_0 = 10^{10}$ , $\Delta T_{ad} = 12$ K, $T^{in} = 600$ K, $Pe_m/Pe_h = 10$ ).....	71
Figure 5.8 Bifurcation diagrams of steady-state exit conversion versus inlet temperature in adiabatic reactors with first-order kinetics and different axial heat Péclet numbers ( $Pe_h$ ). ( $E_a = 100$ kJ/mol, $Da_0 = 10^{10}$ , $\Delta T_{ad} = 200$ K, $Pe_m/Pe_h = 10$ ) ...	73
Figure 5.9 Steady-state axial temperature (solid line) and conversion (dashed line) profiles of adiabatic reactors with first-order kinetics and small $Pe_h$ . ( $E_a = 100$ kJ/mol, $Da_0 = 10^{10}$ , $\Delta T_{ad} = 200$ K, $T^{in} = 400$ K, $Pe_m/Pe_h = 10$ ) .....	74
Figure 5.10 Ignition/extinction loci of adiabatic reactors with first-order kinetics and different axial heat Péclet numbers ( $Pe_h$ ). ( $E_a = 100$ kJ/mol, $Da_0 = 10^{10}$ , $Pe_m/Pe_h = 10$ ).....	75
Figure 5.11 Hysteresis loci of adiabatic reactors with first-order kinetics and different $Pe_m/Pe_h$ ratios in the $(\Delta T_{ad}, Pe_h)$ plane. ( $E_a = 100$ kJ/mol, $Da_0 = 10^{10}$ ) .....	77
Figure 5.12 Hysteresis loci of adiabatic reactors with first-order kinetics and different $Pe_m/Pe_h$ ratios in the $(\chi^{exit}, Pe_h)$ plane. ( $E_a = 100$ kJ/mol, $Da_0 = 10^{10}$ ).....	78
Figure 5.13 Hysteresis loci of adiabatic reactors with first-order kinetics and different $Pe_m/Pe_h$ ratios in the $(T^{in}, Pe_h)$ plane. ( $E_a = 100$ kJ/mol, $Da_0 = 10^{10}$ ).....	79
Figure 5.14 Bifurcation diagrams of steady-state exit conversion versus inlet temperature in adiabatic reactors with Langmuir-Hinshelwood kinetics and different axial heat Péclet numbers ( $Pe_h$ ). ( $E_a = 100$ kJ/mol, $Da_0^{LH} = 10^{10}$ , $\kappa=2000$ , $X^{in}=0.02$ , $Pe_m/Pe_h = 10$ ).....	81

Figure 5.15 Hysteresis loci of adiabatic reactors with Langmuir-Hinshelwood kinetics and different adsorption equilibrium constants ( $\kappa$ ) on the  $(X^{in}, Pe_h)$  plane. ( $E_a = 100$  kJ/mol,  $Da_0^{LH} = 10^{10}$ ,  $Pe_m/Pe_h = 10$ ) .....82

Figure 5.16 Bifurcation diagrams of steady-state exit conversion versus inlet temperature (solid) / mid-bed temperature (dashed) in adiabatic reactors with first-order kinetics and different axial heat Péclet numbers ( $Pe_h$ ). ( $E_a = 100$  kJ/mol,  $Da_0 = 10^{10}$ ,  $\Delta T_{ad} = 200$  K,  $Pe_m/Pe_h = 10$ ) .....84

Figure 5.17 Bifurcation diagrams of steady-state exit conversion versus inlet temperature (solid) / mid-bed temperature (dashed) in adiabatic reactors with first-order kinetics. ( $E_a = 100$  kJ/mol,  $Da_0 = 10^{10}$ ,  $\Delta T_{ad} = 200$  K,  $Pe_h = 0.1$ ,  $Pe_m = 1$ ) .....85

Figure 5.18 Steady-state axial temperature profiles of adiabatic reactors with first-order kinetics and different axial heat Péclet numbers ( $Pe_h$ ) at extinction temperatures. ( $E_a = 100$  kJ/mol,  $Da_0 = 10^{10}$ ,  $\Delta T_{ad} = 200$  K,  $Pe_m/Pe_h = 10$ ) .....87

Figure 5.19 Bifurcation diagrams of steady-state exit conversion versus inlet temperature in adiabatic reactors with first-order kinetics, different axial heat Péclet numbers ( $Pe_h$ ) and different transverse Péclet numbers ( $P_m$  and  $P_h$ ). ( $E_a = 100$  kJ/mol,  $Da_0 = 10^{10}$ ,  $\Delta T_{ad} = 200$  K,  $Pe_m = \infty$ ) .....88

Figure 5.20 Hysteresis loci of adiabatic reactors with first-order kinetics and different transverse Péclet numbers ( $P_m$  and  $P_h$ ) in the  $(\Delta T_{ad}, Pe_h)$  plane. ( $E_a = 100$  kJ/mol,  $Da_0 = 10^{10}$ ,  $Pe_m = \infty$ ) .....90

Figure 5.21 Bifurcation diagrams of steady-state exit conversion versus inlet temperature in reactors with first-order kinetics and different heat loss coefficients ( $\alpha$ ). ( $E_a = 100$  kJ/mol,  $Da_0 = 10^{10}$ ,  $\Delta T_{ad} = 200$  K,  $Pe_h = 1$ ,  $Pe_m = 10$ ) .....94

Figure 5.22 Ignition/extinction loci of reactors with first-order kinetics and different heat loss coefficients ( $\alpha$ ). ( $E_a = 100$ kJ/mol, $Da_0 = 10^{10}$ , $Pe_h = 1$ , $Pe_m = 10$ ) .....	95
Figure 5.23 Hysteresis loci of reactors with first-order kinetics, different axial heat Péclet numbers ( $Pe_h$ ) and heat loss coefficients ( $\alpha$ ). ( $E_a = 100$ kJ/mol, $Da_0 = 10^{10}$ , $Pe_m/Pe_h = 10$ ).....	96
Figure 8.1 Snapshots of transient conversion (a,c) and temperature (b,d) profiles after a step change in inlet temperature. Snapshots are taken every 10 s. [ $\langle u \rangle = 0.5$ m/s in (a) and (b), $\langle u \rangle = 2$ m/s in (c) and (d)] .....	113
Figure 8.2 Dimensionless lengths to achieve 10%, 50% and 90% conversions as a function of time. ( $\Delta T_{ad} = 285$ K, $T^{in} = 450$ K, $\langle u \rangle = 0.5$ m/s).....	114
Figure 8.3 Creep velocity as a function of (a) the gas velocity and (b) the inlet temperature. ( $\Delta T_{ad} = 285$ K). .....	115
Figure 8.4 Creep velocity as a function of (a) the gas velocity and (b) the inlet temperature with different adiabatic temperature rise. [ $T^{in} = 450$ K in (a), $\langle u \rangle = 1$ m/s in (b)].....	117
Figure 8.5 Creep velocity as a function of (a) the gas velocity and (b) the inlet temperature with different solid thermal conductivity. [ $\Delta T_{ad} = 285$ K, $T^{in} = 450$ K in (a), $\langle u \rangle = 1$ m/s in (b)]. .....	118
Figure 8.6 Creep velocity as a function of (a) the gas velocity and (b) the inlet temperature with different solid heat capacity. [ $\Delta T_{ad} = 285$ K, $T^{in} = 450$ K in (a), $\langle u \rangle = 1$ m/s in (b)]. .....	120

Figure 8.7 Creep velocity as a function of (a) the gas velocity and (b) the inlet temperature with different substrate materials. [ $\Delta T_{ad} = 285$ K, $T^{in} = 450$ K in (a), $\langle u \rangle = 1$ m/s in (b)]. .....	121
Figure 8.8 Creep velocity as a function of (a) the gas velocity and (b) the inlet temperature with different reactor length. [ $\Delta T_{ad} = 285$ K, $T^{in} = 450$ K in (a), $\langle u \rangle = 1$ m/s in (b)]. .....	123
Figure 8.9 Creep velocity as a function of (a) the gas velocity and (b) the inlet temperature with different kinetics. [ $X_{CO}^{in} = 0.03$ , $\Delta T_{ad} = 285$ K, $T^{in} = 450$ K in (a), $\langle u \rangle = 1$ m/s in (b)]. .....	125
Figure 8.10 Creep velocity and steady-state conversion as a function of the inlet temperature. [ $\Delta T_{ad} = 238$ K, $\langle u \rangle = 1$ m/s in (a), $\langle u \rangle = 3$ m/s in (b)]. .....	128
Figure 8.11 Plot of critical points and the bifurcation set. ( $\Delta T_{ad} = 238$ K). .....	129
Figure 8.12 Plot of critical points where the reaction zone creeps (a) upstream or (b) all the way to the inlet. .....	131
Figure 8.13 Validation of the correlation.....	132
Figure 8.14 Comparison of correlation predicted creep velocity with exact numerical results.....	133

## List of Tables

Table 1.1 LEV II Emission standards for passenger cars and light duty vehicles under 8500 lbs, g/mi .....	2
Table 2.1 Global kinetics .....	15
Table 2.2 Kinetic parameters for a Pd/Rh based TWC.....	16
Table 2.3 Numerical constants and parameters used in TWC simulation .....	16
Table 2.4 Kinetic parameters for a threshold Pd/Rh based TWC.....	20
Table 2.5 Simulation conditions .....	27
Table 2.6 Fast cycling conditions .....	33
Table 4.1 Characteristic scales.....	46
Table 7.1 Characteristic scales.....	105
Table 8.1 Parameter values .....	112
Table 8.2 Metallic monolith parameters .....	122

# Nomenclature

## Part I

<i>Latin symbols</i>	<i>Definition</i>
$a$	pore radius (m)
$a_c$	normalized catalyst activity
$A$	pre-exponential factor ( $\text{mol} \cdot \text{m}^{-3} \cdot \text{s}^{-1}$ )
$C_p$	specific heat capacity ( $\text{J} \cdot \text{kg}^{-1} \cdot \text{K}^{-1}$ )
$C_{Total}$	total concentration of gas phase species ( $\text{mol} \cdot \text{m}^{-3}$ )
$D$	diffusivity ( $\text{m}^2 \cdot \text{s}^{-1}$ )
$E$	activation energy ( $\text{J} \cdot \text{mol}^{-1}$ )
$h$	heat transfer coefficient ( $\text{W} \cdot \text{m}^{-2} \cdot \text{K}^{-1}$ )
$\mathbf{k}_{me}$	external mass transfer coefficient matrix ( $\text{m} \cdot \text{s}^{-1}$ )
$\mathbf{k}_{mi}$	internal mass transfer coefficient matrix ( $\text{m} \cdot \text{s}^{-1}$ )
$\mathbf{k}_{mo}$	overall mass transfer coefficient matrix ( $\text{m} \cdot \text{s}^{-1}$ )
$L$	length of the monolith channel (m)
$Le$	Lewis number
$M$	molecular mass ( $\text{g} \cdot \text{mol}^{-1}$ )
$N$	number of species
$Nu$	Nusselt number
$p$	pressure (Pa)
$P$	transverse mass Péclet number
$Pe_h$	axial heat Péclet number
$\mathbf{r}$	vector of reaction rates ( $\text{mol} \cdot \text{m}^{-3} \cdot \text{s}^{-1}$ )
$R$	gas constant ( $\text{J} \cdot \text{mol}^{-1} \cdot \text{K}$ )
$R_\Omega$	hydraulic radius of monolith channel (m)
$\mathbf{Sh}$	Sherwood number matrix
$\mathbf{Sh}_i$	internal Sherwood number matrix

<i>Latin symbols</i>	<i>Definition</i>
$t$	time (s)
$T$	temperature (K)
$TOSC$	total oxygen storage capacity ( $\text{mol}\cdot\text{m}^{-3}$ )
$\langle u \rangle$	average feed gas velocity ( $\text{m}\cdot\text{s}^{-1}$ )
$x$	axial coordinate (m)
$\mathbf{X}$	vector of mole fractions
$\mathbf{X}_{fm}$	vector of cup-mixing mole fractions in fluid phase
$\langle \mathbf{X}_{wc} \rangle$	vector of volume averaged mole fractions in washcoat
$\mathbf{X}_s$	vector of mole fractions at gas-solid interface
$y$	transverse coordinate (m)
$z$	dimensionless axial coordinate
<i>Greek symbols</i>	<i>Definition</i>
$\delta_w$	effective wall thickness (m)
$\delta_c$	washcoat thickness (m)
$\epsilon_w$	void fraction (porosity) of washcoat
$\theta$	fractional oxidation state of catalyst
$\lambda$	normalized air/fuel ratio
$\nu$	matrix of stoichiometric coefficients
$\rho$	density ( $\text{kg}\cdot\text{m}^{-3}$ )
$\tau$	tortuosity
$\Phi$	Thiele matrix
<i>Subscripts</i>	<i>Definition</i>
$i$	reaction index
$j$	gaseous component index
$f$	fluid phase
$s$	solid phase

<i>Subscripts</i>	<i>Definition</i>
$w$	wall/washcoat
<i>Superscripts</i>	<i>Definition</i>
$in$	inlet condition
0	initial condition

## Part II

<i>Latin symbols</i>	<i>Definition</i>
$a$	external heat transfer area per unit reactor volume ( $\text{m}^{-1}$ )
$A$	pre-exponential factor
$C$	concentration ( $\text{mol} \cdot \text{m}^{-3}$ )
$C_p$	specific heat capacity ( $\text{J} \cdot \text{kg}^{-1} \cdot \text{K}^{-1}$ )
$\widehat{C}_p$	molar heat capacity ( $\text{J} \cdot \text{mol}^{-1} \cdot \text{K}^{-1}$ )
$D$	molecular diffusivity ( $\text{m}^2 \cdot \text{s}^{-1}$ )
$Da_0$	Damköhler number
$E_a$	activation energy ( $\text{J} \cdot \text{mol}^{-1}$ )
$h$	heat transfer coefficient ( $\text{W} \cdot \text{m}^{-2} \cdot \text{K}^{-1}$ )
$\Delta H$	heat of reaction ( $\text{J} \cdot \text{mol}^{-1}$ )
$k$	thermal conductivity ( $\text{W} \cdot \text{m}^{-1} \cdot \text{K}^{-1}$ )
$k_m$	mass transfer coefficient ( $\text{m} \cdot \text{s}^{-1}$ )
$K_{ads}$	adsorption equilibrium constant ( $\text{m}^3 \cdot \text{mol}^{-1}$ )
$L$	reactor length (m)
$Le$	Lewis number
$\mathbf{n}$	outward unit normal vector
$Nu$	Nusselt number
$P$	transverse Péclet number
$Pe$	axial Péclet number

<i>Latin symbols</i>	<i>Definition</i>
$r$	transverse coordinate (m)
$R$	reaction rate ( $\text{mol} \cdot \text{m}^{-3} \cdot \text{s}^{-1}$ )
$R_g$	gas constant ( $\text{J} \cdot \text{mol}^{-1} \cdot \text{K}$ )
$R_\Omega$	hydraulic radius of flow channel (m)
$Sh$	Sherwood number
$t$	time (s)
$\hat{t}$	dimensionless time
$T$	temperature (K)
$\hat{T}$	dimensionless temperature
$\Delta T_{ad}$	adiabatic temperature rise (K)
$u$	fluid velocity ( $\text{m} \cdot \text{s}^{-1}$ )
$\bar{u}$	average fluid velocity ( $\text{m} \cdot \text{s}^{-1}$ )
$U$	heat transfer coefficient at the outer boundary ( $\text{W} \cdot \text{m}^{-2} \cdot \text{K}^{-1}$ )
$x$	axial coordinate (m)
$X$	mole fraction
$y$	dimensionless concentration
$z$	dimensionless axial coordinate
<i>Greek symbols</i>	<i>Definition</i>
$\alpha$	dimensionless heat loss coefficient
$\alpha_f$	thermal diffusivity of the fluid ( $\text{m}^2 \cdot \text{s}^{-1}$ )
$\beta$	dimensionless adiabatic temperature rise
$\delta$	thickness (m)
$\epsilon$	porosity or void volume fraction
$\varepsilon$	cycling amplitude
$\theta^{in}$	dimensionless inlet temperature
$\kappa$	dimensionless adsorption equilibrium constant

<i>Greek symbols</i>	<i>Definition</i>
$\xi$	dimensionless transverse coordinate
$\rho$	density ( $\text{kg} \cdot \text{m}^{-3}$ )
$\sigma$	heat capacity ratio
$\tau$	space time (s)
$\tau_h$	external heat transfer time (s)
$\chi$	conversion
$\omega$	cycling frequency ( $\text{s}^{-1}$ )
$\hat{\omega}$	dimensionless cycling frequency
$\Omega$	transverse domain
$\partial\Omega$	outer boundary of a transverse domain
<i>Operators</i>	<i>Definition</i>
$\nabla_{\perp}$	transverse gradient operator ( $\text{m}^{-1}$ )
$\hat{\nabla}_{\perp}$	dimensionless transverse gradient operator
$\nabla_{\perp}^2$	transverse Laplacian operator ( $\text{m}^{-2}$ )
$\hat{\nabla}_{\perp}^2$	dimensionless transverse Laplacian operator
<i>Subscripts</i>	<i>Definition</i>
$e$	external mass/heat transfer
$f$	fluid phase
$h$	heat transfer
$i$	internal mass/heat transfer
$m$	mass transfer
$s$	solid phase
$w$	substrate wall
$wc$	washcoat
<i>Superscripts</i>	<i>Definition</i>
0	initial condition

<i>Superscripts</i>	<i>Definition</i>
<i>exit</i>	exit
<i>in</i>	inlet condition
<i>LH</i>	Langmuir-Hinshelwood kinetics
<i>mid</i>	mid-bed

### Part III

<i>Latin symbols</i>	<i>Definition</i>
<i>A</i>	pre-exponential factor
<i>B</i>	Zel'dovich number
<i>C</i>	concentration ( $\text{mol} \cdot \text{m}^{-3}$ )
<i>C<sub>p</sub></i>	specific heat capacity ( $\text{J} \cdot \text{kg}^{-1} \cdot \text{K}^{-1}$ )
<i>D</i>	molecular diffusivity ( $\text{m}^2 \cdot \text{s}^{-1}$ )
<i>Da</i>	Damköhler number
<i>E<sub>a</sub></i>	activation energy ( $\text{J} \cdot \text{mol}^{-1}$ )
<i>h</i>	heat transfer coefficient ( $\text{W} \cdot \text{m}^{-2} \cdot \text{K}^{-1}$ )
$\Delta H$	heat of reaction ( $\text{J} \cdot \text{mol}^{-1}$ )
<i>k</i>	thermal conductivity ( $\text{W} \cdot \text{m}^{-1} \cdot \text{K}^{-1}$ )
<i>k<sub>m</sub></i>	mass transfer coefficient ( $\text{m} \cdot \text{s}^{-1}$ )
<i>K<sub>ads</sub></i>	adsorption equilibrium constant ( $\text{m}^3 \cdot \text{mol}^{-1}$ )
<i>L</i>	reactor length (m)
<i>Nu<sub>Ω</sub></i>	Nusselt number
<i>P</i>	transverse Péclet number
<i>Pe</i>	axial Péclet number
<i>R</i>	reaction rate ( $\text{mol} \cdot \text{m}^{-3} \cdot \text{s}^{-1}$ )
$\hat{R}$	dimensionless rate expression
<i>R<sub>g</sub></i>	gas constant ( $\text{J} \cdot \text{mol}^{-1} \cdot \text{K}$ )

<i>Latin symbols</i>	<i>Definition</i>
$R_{\Omega}$	hydraulic radius of flow channel ( m )
$Sh_{\Omega}$	Sherwood number
$t$	time ( s )
$\hat{t}$	dimensionless time
$T$	temperature ( K )
$\Delta T_{ad}$	adiabatic temperature rise ( K )
$\langle u \rangle$	average fluid velocity ( $\text{m} \cdot \text{s}^{-1}$ )
$v$	creep velocity ( $\text{m} \cdot \text{s}^{-1}$ )
$x$	axial coordinate ( m )
$X$	mole fraction
$y$	transverse coordinate ( m )
$z$	dimensionless axial coordinate
<i>Greek symbols</i>	<i>Definition</i>
$\alpha$	thermal diffusivity ( $\text{m}^2 \cdot \text{s}^{-1}$ )
$\gamma$	dimensionless activation energy
$\delta$	thickness ( m )
$\Lambda$	diffusivity ratio
$\epsilon$	porosity or void volume fraction
$\eta$	effectiveness factor
$\theta$	dimensionless temperature
$\kappa$	dimensionless adsorption equilibrium constant
$\xi$	dimensionless transverse coordinate
$\rho$	density ( $\text{kg} \cdot \text{m}^{-3}$ )
$\sigma$	heat capacity ratio
$\tau$	space time ( s )
$\phi_s^2$	Thiele modulus

<i>Greek symbols</i>	<i>Definition</i>
$\Phi^2$	modified Thiele modulus
$\chi$	conversion
<i>Subscripts</i>	<i>Definition</i>
<i>atw</i>	critical values for reaction zone to creep all the way to the inlet
<i>ext</i>	extinction
<i>f</i>	fluid phase
<i>h</i>	heat transfer
<i>ign</i>	ignition
<i>m</i>	mass transfer
<i>s</i>	solid phase
<i>up</i>	critical values for reaction zone to creep upstream
<i>w</i>	substrate wall
<i>wc</i>	washcoat
<i>Superscripts</i>	<i>Definition</i>
0	initial condition
<i>in</i>	inlet condition

# Part I

## Low-dimensional Modeling of a Three-way Catalytic Converter

# Chapter 1

## Introduction and Literature Review

The vehicle industry is facing increasingly challenging and diverse emissions requirements. Automobile emissions such as carbon monoxide (CO), hydrocarbons (HC) and nitrogen oxides (NO<sub>x</sub>) are regulated through the Clean Air Act. Shown in Table 1.1 is the LEV II emissions standards as followed by California Air Regulation Board (CARB). LEV III, to be phased-in over 2014-2022 introduces even stricter emissions standards. In addition to the new cutting-edge criteria pollutant regulations in California, large developing countries like China and Brazil are moving forward with their own regulations (Johnson, 2014). Adding to the challenge are the various fuel consumption or greenhouse gas regulations, fuel quality differences, and very-different market requirements.

Table 1.1: LEV II Emission standards for passenger cars and light duty vehicles under 8500 lbs, g/mi (CEPA, 2011)

Category	50,000 miles/ 5 years					120,000 miles / 11 years				
	NMOG	CO	NO <sub>x</sub>	PM	HCHO	NMOG	CO	NO <sub>x</sub>	PM	HCHO
LEV	0.075	3.4	0.05	-	0.015	0.09	4.2	0.07	0.01	0.018
ULEV	0.040	1.7	0.05	-	0.118	0.055	2.1	0.07	0.01	0.011
SULEV	-	-	-	-	-	0.01	1.0	0.02	0.01	0.004

Technologies to help meet these diverse emissions requirements are developing very quickly. Catalytic after-treatment systems are developed for both diesel and gasoline engine emissions, which include DOC (diesel oxidation catalyst), SCR (selective catalytic reduction system), LNT (lean NO<sub>x</sub> trap), etc. for diesel engines and TWC (three-way catalytic converter), HC traps, etc. for gasoline engines. Apart from emissions, the 1990 amendment to the Clean Air Act, also requires the vehicle to have a built-in On-Board Diagnostics (OBD) system. The OBD is a computer

based system designed to monitor the major engine equipment used to measure and control the emissions. Having an optimal fuelling controller for the catalytic after-treatment systems utilizing physics based models will play a major role in satisfying future low emission and OBD guidelines.

The TWC is a standard exhaust after-treatment unit commonly used in gasoline engines to simultaneously oxidize CO and HC to CO<sub>2</sub> and H<sub>2</sub>O while reducing NO<sub>x</sub> to N<sub>2</sub> provided the feed gas is controlled to an air-fuel ratio consistent with the state of the catalyst. The air-fuel mixture entering the TWC is often quantified using the normalized air to fuel ratio (A/F), defined as

$$\lambda = \frac{(A/F)_{actual}}{(A/F)_{stoichiometry}}.$$

Thus,  $\lambda > 1$  corresponds to a (fuel) lean operation while  $\lambda < 1$  corresponds to a rich operation. It is well known that there exists a narrow zone around stoichiometry ( $\lambda = 1$ ) where the TWC efficiency is simultaneously maximum for all the major pollutants (Heywood, 1988; Heck et al., 2009). Thus, gasoline engines are normally controlled to operate around stoichiometry. However, in real world operating conditions, slight excursions from the stoichiometric condition are often observed. Thus, ceria stabilized with zirconia is added in the TWC to act as a buffer for oxygen storage to help curb the breakthrough of emissions.

Traditionally, the TWC is controlled based on catalyst monitor sensors (CMS) set points, specifically universal exhaust gas oxygen sensor (UEGO) and heated exhaust gas oxygen sensor (HEGO) set points. While HEGO is a switch type oxygen sensor with sharp transition around stoichiometry, UEGO can be used to measure A/F over a wider range. Typically, UEGO is placed after the engine for more accurate A/F measurement while HEGO is preferred to measure A/F after the TWC because of its lower cost and faster response time. The inner loop controls the A/F to a set value

while the outer loop modifies the A/F reference to the inner loop to maintain the desired HEGO set voltage (around 0.6-0.7 V, depending on design and calibration) to achieve the desired catalyst efficiency. With this arrangement we rely on emissions breakthrough at the HEGO sensor to determine if the catalyst is saturated (lean) or depleted (rich) of oxygen storage and as such it imposes a limitation on the controller design.

If the oxidation state of the catalyst can be measured or modeled, then a model based approach to tighter control on breakthrough emissions would be feasible. Emission control then would be less dependent on sensor location and thus applicable for both partial and full volume catalyst systems. This can be achieved using a physics based model for the TWC. In the literature, most of the models for TWCs are represented by a set of partial differential equations (PDEs) in time and space (Oh and Cavendish, 1982; Siemund et al., 1996; Auckenthaler et al., 2004) and as such their discretization results in several hundreds of ordinary differential equations (ODEs) depending upon the number of grid points used for describing spatial variations and species considered. Although such models provide a good description of the actual system, they are computationally expensive for on-board implementation. On the other hand, the over-simplified control based oxygen storage models treat the TWC as a limited integrator and are usually empirically designed. Such models may not be accurate over a wide range of operating conditions encountered in a real system and are inadequate for tight emissions control.

In a recent publication (Kumar et al., 2012), a zero-dimensional TWC model (0-D model) comprising of seven ordinary differential equations (ODEs) was proposed. This fundamental-based model predicts the TWC's fractional oxidation state (FOS) and the total oxygen storage capacity (TOSC) which directly reflect the state and aging of the catalyst, helpful for accurate fueling control and TWC diagnostics. Using a simplified chemistry and an axial averaging method, the 0-D model is less compu-

tationally demanding, thus appropriate for real-time automotive applications. In this work we extend the model to include spatial variation and discuss the range of validity and limitations of the 0-D model. We also validate the internal mass transfer approximation and the seven partial differential equation (PDE) model by comparing the model predictions during cold start and fast cycling with the detailed solution. The model is observed to retain all the qualitative features and have a good quantitative agreement.

## Chapter 2

# Spatio-temporal Dynamics of Oxygen Storage and Release in a Three-way Catalytic Converter

A one-dimensional TWC model (1-D model) is derived from a detailed washcoat diffusion model by simplifying the mass transfer along the transverse direction by using internal and external mass transfer coefficients. In an earlier work by Joshi et al. (2009), a similar model was used and verified with the detailed three-dimensional PDE model solved using software such as COMSOL [version 3.3, Copyright 1994-2007 by COMSOL Inc.]. The model was observed to have an agreement with the detailed model. However, in that model a constant asymptotic Sherwood number was used to compute the internal mass transfer coefficient in the multiple reaction case. Also the ceria kinetics which include gas-solid reactions were not considered. Here, we present a more general approach and later verify it with both experimental data and detailed model results. An axially averaged version of the model presented here was used in Kumar et al. (2012), where the 0-D model was experimentally validated and was found adequate to predict the oxygen storage dynamics following the cold start. For more accurate predictions even during the temperature transients (cold start), the 1-D model is proposed.

## 2.1 Mathematical Model

In this model, we assume that the entire TWC can be represented by a single channel, which is divided into the fluid phase and the solid phase. The feed gas flows axially through the catalyst while mass and heat are transported in both axial and transverse directions by convection (in fluid phase) and diffusion (in solid phase). We utilize internal and external mass transfer coefficient concepts to capture the transport in the transverse direction (Balakotaiah, 2008) so that the model becomes one-dimensional. The equations are derived from species and energy balances in the two phases. Bold symbols are used to represent matrices and vectors.

The species balance in the fluid phase (for gas phase species) is given by

$$\frac{\partial \mathbf{X}_{fm}}{\partial t} = -\langle u \rangle \frac{\partial \mathbf{X}_{fm}}{\partial x} - \frac{\mathbf{k}_{mo}}{R_{\Omega}} (\mathbf{X}_{fm} - \langle \mathbf{X}_{wc} \rangle). \quad (2.1)$$

The species balance in the washcoat (for gas phase species) is

$$\epsilon_w \frac{\partial \langle \mathbf{X}_{wc} \rangle}{\partial t} = \frac{1}{C_{Total}} \boldsymbol{\nu}^T \mathbf{r} + \frac{\mathbf{k}_{mo}}{\delta_c} (\mathbf{X}_{fm} - \langle \mathbf{X}_{wc} \rangle). \quad (2.2)$$

Here, the column vectors,  $\mathbf{X}_{fm}$  and  $\langle \mathbf{X}_{wc} \rangle \in \mathbb{R}^N$ , represent the cup-mixing mole fractions in the fluid phase and the volume averaged mole fractions in the washcoat, respectively. The average feed gas velocity,  $\langle u \rangle$ , is computed using the measured air mass and known A/F ratio (or  $\lambda$ ) for given feed inlet temperature. The overall mass transfer coefficient matrix ( $\mathbf{k}_{mo}$ ) is given by

$$\mathbf{k}_{mo}^{-1} = \mathbf{k}_{me}^{-1} + \mathbf{k}_{mi}^{-1}, \quad (2.3)$$

where  $\mathbf{k}_{me}$  and  $\mathbf{k}_{mi}$  are the external and internal mass transfer coefficient matrices. Here,  $R_{\Omega}$  represents the hydraulic radius of the monolith channel,  $\epsilon_w$  and  $\delta_c$  are the

porosity and thickness of the washcoat, respectively. The vector  $\mathbf{r} \in \mathbb{R}^{Nr}$  is the reaction rate vector, where each element  $r_i$  represents the rate of the  $i^{th}$  reaction as shown in Table 2.1. The parameters  $N$  and  $Nr$  represent the total numbers of gaseous species and reactions, respectively. The stoichiometric matrix,  $\boldsymbol{\nu} \in \mathbb{R}^{Nr \times N}$ , is a matrix of stoichiometric coefficients with rows representing the reaction index while the columns representing species index. The total concentration ( $C_{Total}$ ) is computed at the channel inlet using the ideal gas law

$$C_{Total} = \frac{p}{RT_f^{in}(t)}. \quad (2.4)$$

Here,  $p$  represents the total gas pressure, assumed constant at 1 atm,  $T_f^{in}$  is the inlet gas temperature. The expression of Eqs. 2.1 and 2.2 in mole fractions is based on the assumption that  $C_{Total}$  is constant along the length of the channel. This assumption can be validated by performing total carbon mole balance at the inlet and exit of the TWC. Shown in Fig. 2.1 is the total carbon balance in terms of mole fractions at the TWC inlet (solid blue curve) and exit (dashed green curve), in which total carbon is defined as

$$Total\ Carbon = [CO] + [CH_y] + [CO_2].$$

As the total carbon mole fractions at the inlet and exit are practically the same, the constant  $C_{Total}$  assumption is valid.

The energy balance in the fluid phase is

$$\rho_f C_{p_f} \frac{\partial T_f}{\partial t} = -\langle u \rangle \rho_f C_{p_f} \frac{\partial T_f}{\partial x} - \frac{h}{R_{\Omega}} (T_f - T_s), \quad (2.5)$$

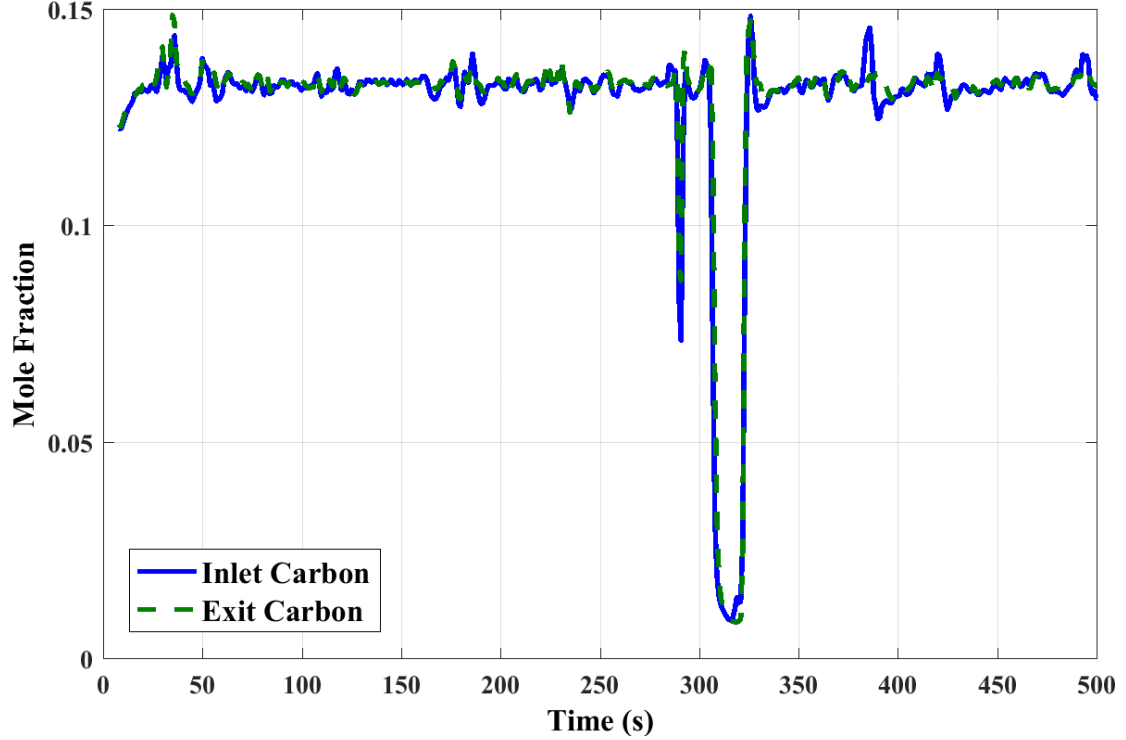


Figure 2.1: Total carbon balance in terms of mole fractions at the TWC inlet and exit during bag 1 of an FTP cycle.

and the energy balance for the solid phase is

$$\delta_w \rho_w C p_w \frac{\partial T_s}{\partial t} = \delta_w k_w \frac{\partial^2 T_s}{\partial x^2} + h (T_f - T_s) + \delta_c \mathbf{r}^T (-\Delta \mathbf{H}). \quad (2.6)$$

Here,  $T_f$  is the fluid temperature,  $\rho_f$  and  $C p_f$  are the density and specific heat capacity of the fluid phase.  $T_s$  is the solid temperature and  $\delta_w$  represents the effective wall thickness (defined as  $\delta_w = \delta_s + \delta_c$ , where  $\delta_s$  is the half-thickness of wall),  $\rho_w$  and  $C p_w$  are the effective density and specific heat capacity of the washcoat, respectively, defined as  $\delta_w \rho_w C p_w = \delta_c \rho_c C p_c + \delta_s \rho_s C p_s$  and  $\delta_w k_w = \delta_c k_c + \delta_s k_s$ , where the subscript  $s$  and  $c$  represent the support and catalyst washcoat, respectively;  $h$  in Eqs. 2.5 and 2.6 represents the local heat transfer coefficient.

To quantify the oxygen storage on ceria, we define the fractional oxidation state

(FOS),  $\theta$  of ceria as,

$$\theta = \frac{[Ce_2O_4]}{[Ce_2O_4] + [Ce_2O_3]}, \quad (2.7)$$

$$\frac{\partial \theta}{\partial t} = \frac{1}{2TOSC} (r_{store} - r_{release}), \quad (2.8)$$

or for the simplified kinetics used in this work,

$$\frac{\partial \theta}{\partial t} = \frac{1}{2TOSC} (r_2 - r_3), \quad (2.9)$$

where  $r_2$  and  $r_3$  are reaction rates for oxidation and reduction of ceria as defined in Table 2.1. Here  $TOSC$  is the total oxygen storage capacity.

The initial and boundary conditions are given by

$$\mathbf{X}_{fm}(x, 0) = \mathbf{X}_{fm}^0(x), \quad \langle \mathbf{X}_{wc}(x, 0) \rangle = \langle \mathbf{X}_{wc}^0(x) \rangle, \quad (2.10)$$

$$T_f(x, 0) = T_f^0(x), \quad T_s(x, 0) = T_s^0(x), \quad (2.11)$$

$$\theta(x, 0) = \theta^0(x), \quad (2.12)$$

$$\mathbf{X}_{fm}(0, t) = \mathbf{X}_{fm}^{in}(t), \quad T_f(0, t) = T_f^{in}(t), \quad \text{and} \quad (2.13)$$

$$\left. \frac{\partial T_s}{\partial x} \right|_{x=0} = \left. \frac{\partial T_s}{\partial x} \right|_{x=L} = 0. \quad (2.14)$$

The model proposed consists of two species balance equations (Eqs. 2.1 and 2.2) for each gaseous species, two energy balance equations (Eqs. 2.5 and 2.6) and a balance equation for ceria (Eq. 2.9). For the global kinetic model used in this work, the 1-D model involves two gaseous species and thus comprises of seven PDEs.

## 2.2 Mass and Heat Transfer Correlations

The gradients in the transverse direction are accounted by the use of internal and external mass transfer coefficients, computed using the Sherwood number ( $Sh$ ) correlations. The external mass transfer coefficient matrix  $\mathbf{k}_{me} \in \mathbb{R}^{N \times N}$  is defined by

$$\mathbf{k}_{me} = \frac{\mathbf{D}_f \mathbf{Sh}}{4R_\Omega}. \quad (2.15)$$

Assuming the gases to be diluted in nitrogen, the gas phase diffusivity matrix,  $\mathbf{D}_f \in \mathbb{R}^{N \times N}$  is a diagonal matrix with the  $j^{th}$  diagonal element representing the diffusivity of the  $j^{th}$  species in nitrogen. To compute the diffusivity as a function of temperature, we use the Lennard-Jones calculation for molecular diffusivity (Bird et al., 2002) over the temperature range of 300-900 K and then correlate as

$$D_f = 1.213 \times 10^{-9} T_f^{1.709}. \quad (2.16)$$

As the lumped species (reductant and oxidant) have similar molecular mass, a single value of diffusivity is used, i.e.  $\mathbf{D}_f = D_f \mathbf{I}$ , where  $\mathbf{I} \in \mathbb{R}^{N \times N}$  is the identity matrix.

Sherwood number matrix  $\mathbf{Sh}$  is also diagonal given by  $\mathbf{Sh} = Sh \mathbf{I}$ . We use a position dependent Sherwood number  $Sh$ , defined for fully developed flow with constant flux boundary condition (Gundlapally et al., 2011)

$$Sh = Sh_\infty + \frac{0.272(\frac{P}{z})}{1 + 0.083(\frac{P}{z})^{\frac{2}{3}}}, \quad (2.17)$$

where  $Sh_\infty = 3.2$  for rounded square channel,  $z = x/L$  is the dimensionless length and  $P$  is transverse mass Péclet number defined as

$$P = \frac{R_\Omega^2 \langle u \rangle}{LD_f}. \quad (2.18)$$

The internal mass transfer coefficient matrix is defined as (Balakotaiah, 2008)

$$\mathbf{k}_{mi} = \frac{\mathbf{D}_s \mathbf{Sh}_i}{\delta_c}. \quad (2.19)$$

In the washcoat, the effective diffusivity will be dominated by Knudsen diffusion. As each species diffuses independently in the Knudsen regime, the washcoat diffusivity ( $\mathbf{D}_s$ ) matrix becomes a diagonal matrix with the diagonal elements ( $D_{s,j}$ ) representing diffusivity of the  $j^{th}$  species,

$$D_{s,j} = \frac{\epsilon_w}{\tau} 97a \sqrt{\frac{T_s}{M_j}}, \quad (2.20)$$

where  $M_j$  is the molecular mass of the  $j^{th}$  species,  $\epsilon_w$  is the washcoat porosity,  $\tau$  is the tortuosity and  $a$  is the mean pore radius. The molecular mass of the reductant is taken as  $28 \text{ g} \cdot \text{mol}^{-1}$  while that for the oxidant is  $32 \text{ g} \cdot \text{mol}^{-1}$ .

The internal Sherwood number matrix,  $\mathbf{Sh}_i \in \mathbb{R}^{N \times N}$ , is evaluated as a function of the Thiele matrix ( $\Phi$ ) as (Balakotaiah, 2008)

$$\mathbf{Sh}_i = \mathbf{Sh}_{i,\infty} + (\mathbf{I} + \Lambda \Phi)^{-1} \Lambda \Phi^2. \quad (2.21)$$

For the case of a square channel with a rounded square flow area, the asymptotic internal Sherwood matrix is given by  $\mathbf{Sh}_{i,\infty} = Sh_{i,\infty} \mathbf{I}$  where  $Sh_{i,\infty} = 2.65$  and the constant  $\Lambda = 0.58$  (Joshi et al., 2009). The Thiele matrix,  $\Phi^2 \in \mathbb{R}^{N \times N}$ , is defined as

$$\Phi^2 = \delta_c^2 (\mathbf{D}_s)^{-1} \left( -\frac{1}{C_{Total}} \frac{d(\mathbf{R}(\mathbf{X}))}{d\mathbf{X}} \right)_{\mathbf{x}=\mathbf{x}_s}. \quad (2.22)$$

Here the column vector  $\mathbf{R}(\mathbf{X}) = \boldsymbol{\nu}^T \mathbf{r}(\mathbf{X})$  where each element  $R_j(\mathbf{X})$  represents the net rate of formation for the  $j^{th}$  species. The vector  $\mathbf{X}_s$  is the vector of mole fractions

at the fluid-solid interface, which for the 1-D model can be expressed as

$$\mathbf{X}_s = (\mathbf{k}_{me} + \mathbf{k}_{mi})^{-1} (\mathbf{k}_{me} \mathbf{X}_{fm} + \mathbf{k}_{mi} \langle \mathbf{X}_{wc} \rangle). \quad (2.23)$$

For computational simplification, we approximate  $\Phi^2$  by using an effective rate constant for each reactant species as

$$k_{j,eff} = - \frac{1}{C_{Total}} \frac{R_j(\mathbf{X})}{X_j} \Big|_{\mathbf{x}=\mathbf{x}_{fm}} \quad (2.24)$$

in which case,  $\Phi^2$  becomes a diagonal matrix with the diagonal terms defined as

$$\Phi_{jj}^2 = \frac{\delta_c^2}{D_{s,j}} k_{j,eff}. \quad (2.25)$$

More details about the derivation of  $\Phi$  and computation of  $Sh_i$  can be found in Kumar et al. (2012).

The heat transfer coefficient  $h$  in Eqs. 2.5 and 2.6 is computed using the Nusselt number ( $Nu$ ) correlation as

$$h = \frac{Nu k_f}{4R_\Omega}.$$

Similar to the previous calculation of the Sherwood number, we use a position dependent Nusselt number ( $Nu$ ) (Gundlapally et al., 2011)

$$Nu = Nu_\infty + \frac{0.272 \left( \frac{P}{zLe_f} \right)}{1 + 0.083 \left( \frac{P}{zLe_f} \right)^{\frac{2}{3}}},$$

where  $Nu_\infty = 3.2$  for rounded square channel and  $Le_f$  is the Lewis number for the fluid phase defined as

$$Le_f = \frac{k_f}{\rho_f C p_f D_f}.$$

## 2.3 Kinetic Model

The kinetic model has been adapted from an earlier work (Kumar et al., 2012) as shown in Table 2.1. The species are lumped into ‘pseudo-species’ defined as total reductant and total oxidant. We define the total reductant "A" as

$$[A] = (2 + \frac{y}{2})[CH_y] + [CO] + [H_2] + \frac{3}{2}[NH_3], \quad (2.26)$$

where  $[CH_y]$  represents the hydrocarbon present in the feed to TWC. In this work, we take  $y = 1.865$  corresponding to gasoline fuel. The total oxidant is defined as

$$[O_x] = [O_2] + \frac{1}{2}[NO]. \quad (2.27)$$

From here on, " $O_2$ " will be used to represent total oxidant unless specified otherwise.

The oxidation products are defined as

$$[AO] = [CO_2] + [H_2O]. \quad (2.28)$$

It may be noted that this lumping of species is valid only for the case of low concentration (diluted) mixtures. As  $N_2$  is present in excess in TWC operations, the above approximation holds. By lumping the species, one loses the flexibility of predicting individual species emissions in exhaust; however it makes the problem more manageable by significantly reducing the number of kinetic parameters to be estimated. The lower memory requirement and faster computation makes it an attractive choice for real time implementation.

The net rate of production of any species can be obtained by multiplying the reaction rate with the corresponding stoichiometric numbers, i.e.,  $\mathbf{R}(\mathbf{X}) = \boldsymbol{\nu}^T \mathbf{r}(\mathbf{X})$ . Ordering the species as  $A$  and  $O_2$ , we have

Table 2.1: Global kinetics

No.	Reaction	Reaction rate (mol·m <sup>-3</sup> ·s <sup>-1</sup> )
1	$A + 0.5O_2 \longrightarrow AO$	$r_1 = a_c \frac{A_1 \exp(\frac{-E_1}{RT}) X_{O_2} X_A}{T_s(1+K_{a1}X_A)^2}$
2	$Ce_2O_3 + 0.5O_2 \longrightarrow Ce_2O_4$	$r_2 = a_c A_2 \exp(\frac{-E_2}{RT}) X_{O_2} (1 - \theta) TOSC_{green}$
3	$A + Ce_2O_4 \longrightarrow Ce_2O_3 + AO$	$r_3 = a_c A_3 \exp(\frac{-E_3}{RT}) X_A \theta TOSC_{green}$

$$\boldsymbol{\nu}^T = \begin{bmatrix} -1 & 0 & -1 \\ -\frac{1}{2} & -\frac{1}{2} & 0 \end{bmatrix} \quad \text{and} \quad \mathbf{r} = \begin{bmatrix} r_1 & r_2 & r_3 \end{bmatrix}^T.$$

The  $TOSC$  represents the total oxygen storage capacity and is a function of aging. A green catalyst has a higher  $TOSC$  value as compared to an aged catalyst and this property can be used for TWC diagnostics.  $TOSC$  can be represented as

$$TOSC = a_c TOSC_{green}, \quad (2.29)$$

where  $a_c$  is the normalized catalyst activity. For a green or fresh catalyst  $a_c = 1$  and it reduces as the catalyst ages.  $TOSC_{green}$  is the maximum storage capacity observed for a green catalyst. For a given catalyst age, it is assumed that  $TOSC$  remains constant. The dependence of  $TOSC$  on temperature is indirectly incorporated through the reaction rate constants (pre-exponential factors and activation energies). For simplification, it is assumed that the catalyst sintering reduces both Pt/Pd/Rh and ceria kinetics by a similar factor  $a_c$  as shown in Table 2.1.

## 2.4 Experimental Validation

The 1-D model was validated using experimental results collected during various drive cycles. Details concerning the experimental setup and operating conditions can be found in Kumar et al. (2012). The kinetic parameters were identified using a genetic algorithm that generates an initial value for a MATLAB [version 7.14.0.739,

Table 2.2: Kinetic parameters for a Pd/Rh based TWC

No.	$A_i$		$E_i$ (kJ·mol <sup>-1</sup> )	$-\Delta H_i$ (kJ·mol <sup>-1</sup> )
1	$9.8 \times 10^{18}$	mol·m <sup>-3</sup> ·s <sup>-1</sup> ·K	105	283
2	$9.2 \times 10^{13}$	s <sup>-1</sup>	80	100
3	$1.8 \times 10^7$	s <sup>-1</sup>	75	183
<i>Adsorption constant</i>		$A_{a1}$	$E_a$ (kJ·mol <sup>-1</sup> )	
$K_{a1} = A_{a1} \exp(-E_a/RT)$		65.5	-7.99	
$TOSC_{green} = 200 \text{ mol} \cdot \text{m}^{-3}$ washcoat				

Table 2.3: Numerical constants and parameters used in TWC simulation

Constant	Value
$a$	$10 \times 10^{-9}$ m
$R_\Omega$	$181 \times 10^{-6}$ m
$\delta_c$	$30 \times 10^{-6}$ m
$\delta_w$	$63.5 \times 10^{-6}$ m
$L$	$7.85 \times 10^{-2}$ m
$k_f$	$0.0386 \text{ W} \cdot \text{m}^{-1} \cdot \text{K}^{-1}$
$k_w$	$1.5 \text{ W} \cdot \text{m}^{-1} \cdot \text{K}^{-1}$
$Cp_f$	$1068 \text{ J} \cdot \text{kg}^{-1} \cdot \text{K}^{-1}$
$Cp_w$	$1000 \text{ J} \cdot \text{kg}^{-1} \cdot \text{K}^{-1}$
$\rho_w$	$2000 \text{ kg} \cdot \text{m}^{-3}$
$\epsilon_w$	0.41
$\tau$	8
$Sh_\infty$	3.2
$Nu_\infty$	3.2
$Sh_{i,\infty}$	2.65
$\Lambda$	0.58

Copyright 1984-2012 by The MathWorks, Inc.] inbuilt constrained optimization program "fmincon". The kinetic parameters used are shown in Table 2.2. The constants used in the simulation are shown in Table 2.3.

Shown in Fig. 2.2 and 2.3 are the instantaneous oxidant and reductant emissions, respectively, during an idle operation (vehicle speed=0 mph). An open loop lean-rich modulation of feed gas A/F ratio was performed. The dash-dotted black curve represents the feed gas composition while the solid red and dashed green curves represent the model estimated TWC exhaust emissions with 1-D and 0-D model. The dotted blue curve represents the measured emissions. The reductant emission shows

a much better fit with the 1-D model than with the 0-D model. The oxidant emission performances for both models are similar. The model achieved a root mean squared error (RMSE) of 0.05 for reductant emission while a RMSE of 0.11 was obtained for oxidant emission.

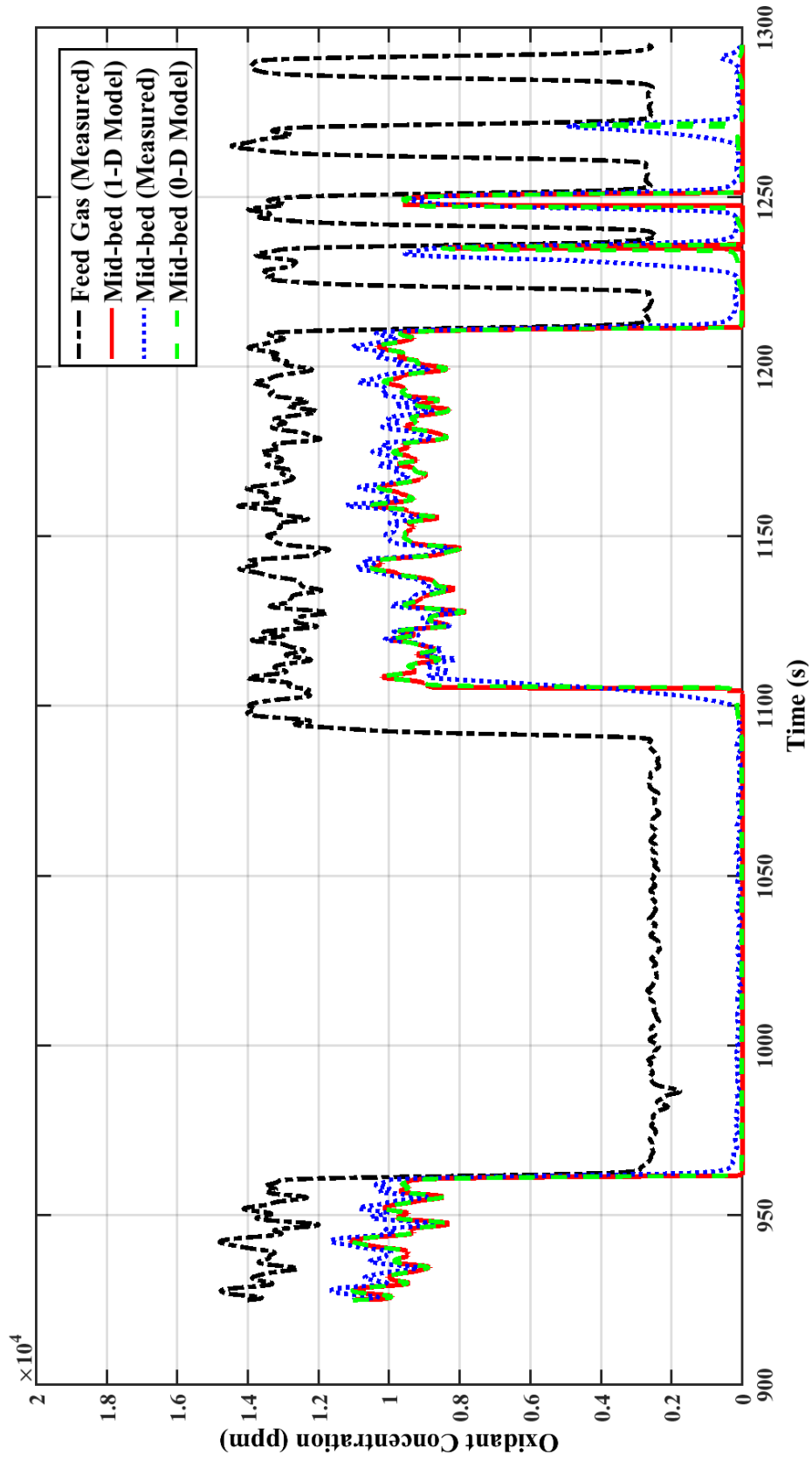


Figure 2.2: Model validation for oxidant emission at idle speed.

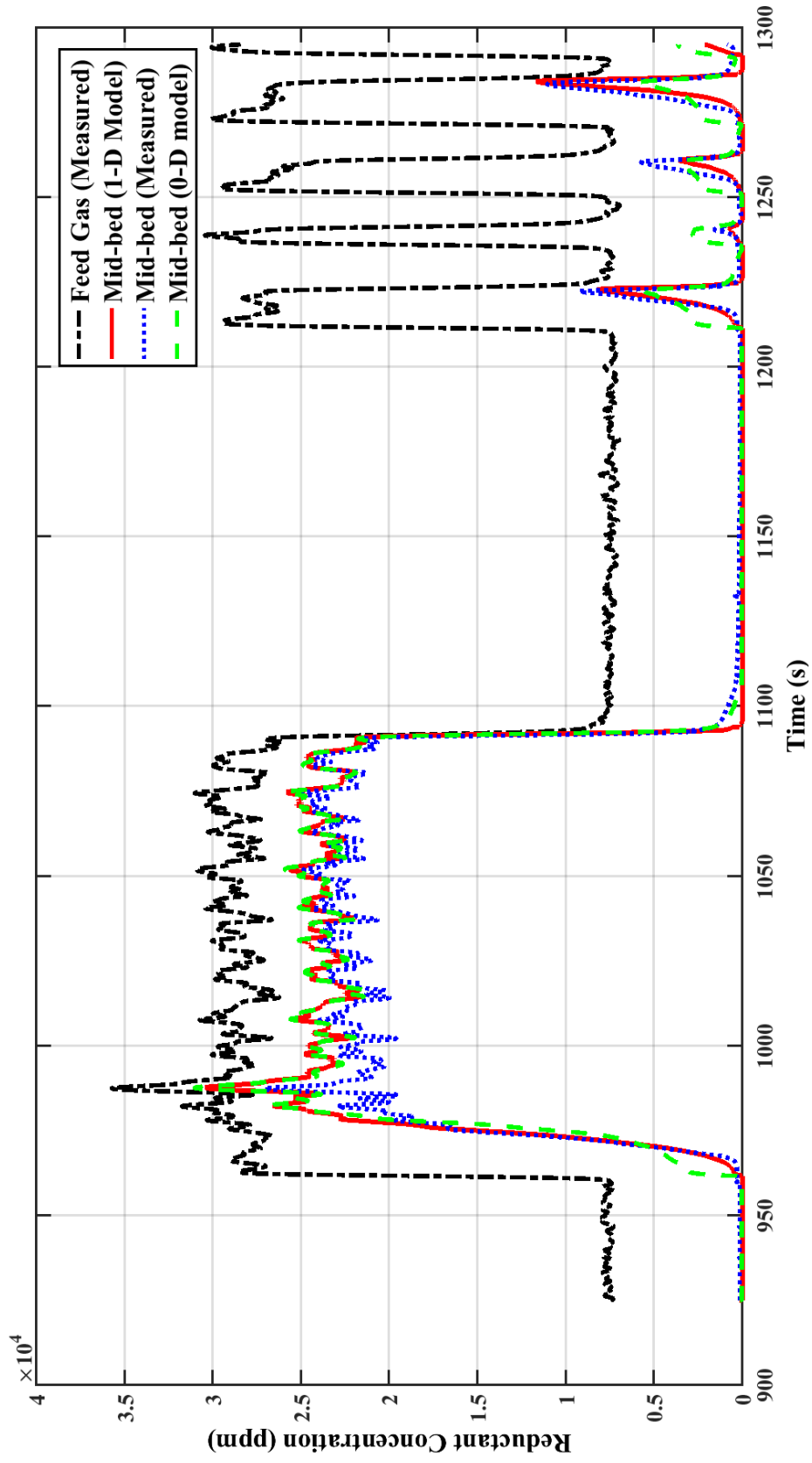


Figure 2.3: Model validation of reductant emission at idle speed.

Table 2.4: Kinetic parameters for a threshold Pd/Rh based TWC

No.	$A_i$		$E_i$ (kJ·mol <sup>-1</sup> )	$-\Delta H_i$ (kJ·mol <sup>-1</sup> )
1	$4.3 \times 10^{19}$	mol·m <sup>-3</sup> ·s <sup>-1</sup> ·K	105	283
2	$9.2 \times 10^{15}$	s <sup>-1</sup>	80	100
3	$4.6 \times 10^6$	s <sup>-1</sup>	75	183
<i>Adsorption constant</i>		$A_{a1}$	$E_a$ (kJ·mol <sup>-1</sup> )	
$K_{a1} = A_{a1} \exp(-E_a/RT)$		65.5	-7.99	
$TOSC_{green} = 10 \text{ mol} \cdot \text{m}^{-3}$ washcoat				

It is interesting to observe that the step change response in oxidant emission (Fig. 2.2) is much sharper as that compared to reductant emission (Fig. 2.3) implying that the ceria reduction is slower than oxidation at the operating conditions of the experiment. Another possible reason for such a behavior is that by switching from lean to rich feed, the feed temperature drops and the observed reaction rate decreases, while step change from rich to lean increases the feed temperature thus enhances the kinetics. The model performance is also compared at other operating conditions and good match was observed.

EPA Federal Test Procedure (commonly known as FTP-75 for city driving cycle) is a series of standardized tests used for measuring tailpipe emissions. Shown in Fig. 2.4 are the vehicle speed, inlet temperature and feed gas velocity over bag 1 of an FTP cycle. Shown in Fig. 2.5 (a) is the model validation over bag 1 of an FTP cycle for the first 100 seconds. The kinetic parameters used are shown in Table 2.4. The solid blue curve represents the measured cumulative reductant emission, while dash-dotted green and dashed red curves denote the model predicted mid-bed emissions as computed using the 0-D model and the 1-D model, respectively. The dotted black curve shows the feed condition going into the catalyst for reference. The use of the 1-D model improved the prediction accuracy. The 0-D model predicts a delayed light-off as compared to the 1-D model. Once ignited, however, both models exhibit similar performances as shown in Fig. 2.5 (b) comparing the model predictions over the entire bag 1 of an FTP cycle. The two curves (dashed green and solid red) could be seen

moving parallel to each other. Similar performance was observed with cumulative oxidant emissions. Shown in Fig. 2.6 is the comparison of the length averaged FOS profiles as obtained using 0-D (dashed green curve) and 1-D model (solid red curve), respectively. Both the models have a similar qualitative profile. The 1-D model, however, shows a relatively slower transient or a filtered response as compared to the 0-D model.

Depending on how many grid points are used, the computational demand of the 1-D model can vary. For all the cases discussed in this part, 40 grid points are enough for practical purposes resulting in 280 ODEs. Considering the computational complexity and the increase in accuracy achieved, the 0-D model could be sufficient for controller design in real-time applications where memory and computational time are the major constraints. Also for the first 30-40 seconds when the 0-D model is not accurate, the controller usually operates in open loop as the HEGO sensor takes about the same amount of time to provide meaningful observation. However, for offline TWC outer loop controller design and validation, the 1-D model is a better alternative since it takes spatial effects into account and hence is a more accurate representation of the real system.

Shown in Fig. 2.7 is the catalyst brick temperature profile at different time during the cold start. The ignition occurs in about 20 seconds at the front and in about 70 seconds the entire catalyst becomes ignited. Thus for the first 30-40 seconds because the temperature gradient is significant, the axially averaged 0-D model will be inaccurate. The temperature gradient can also occur during sudden acceleration or deceleration of a vehicle and during prolonged engine stop as encountered in modern stop and go hybrid engine vehicles. The width of the temperature front can be estimated using the effective heat Péclet number correlation, (Gundlapally and

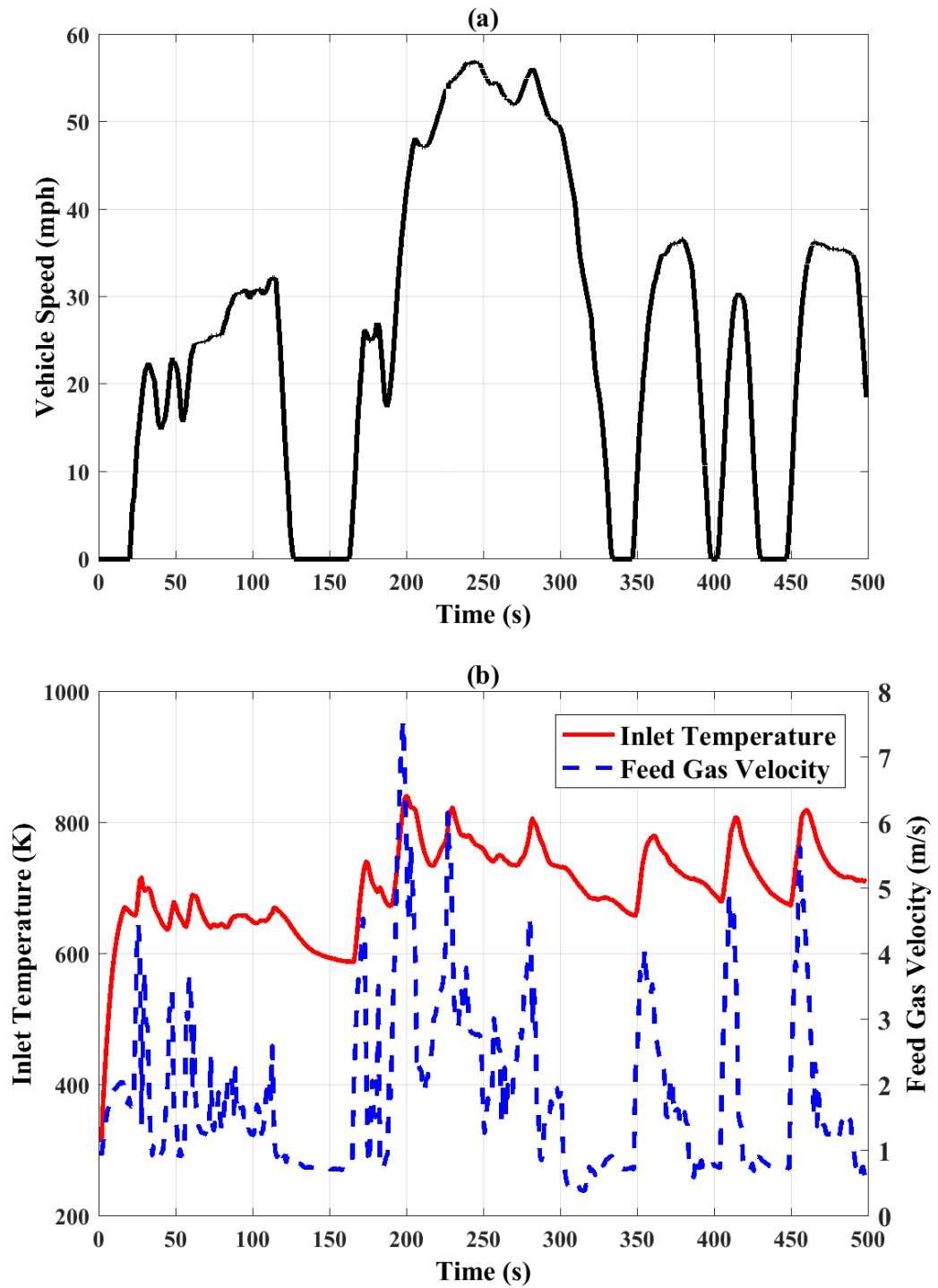


Figure 2.4: (a) Vehicle speed, (b) inlet temperature and feed gas velocity over bag1 of an FTP cycle.

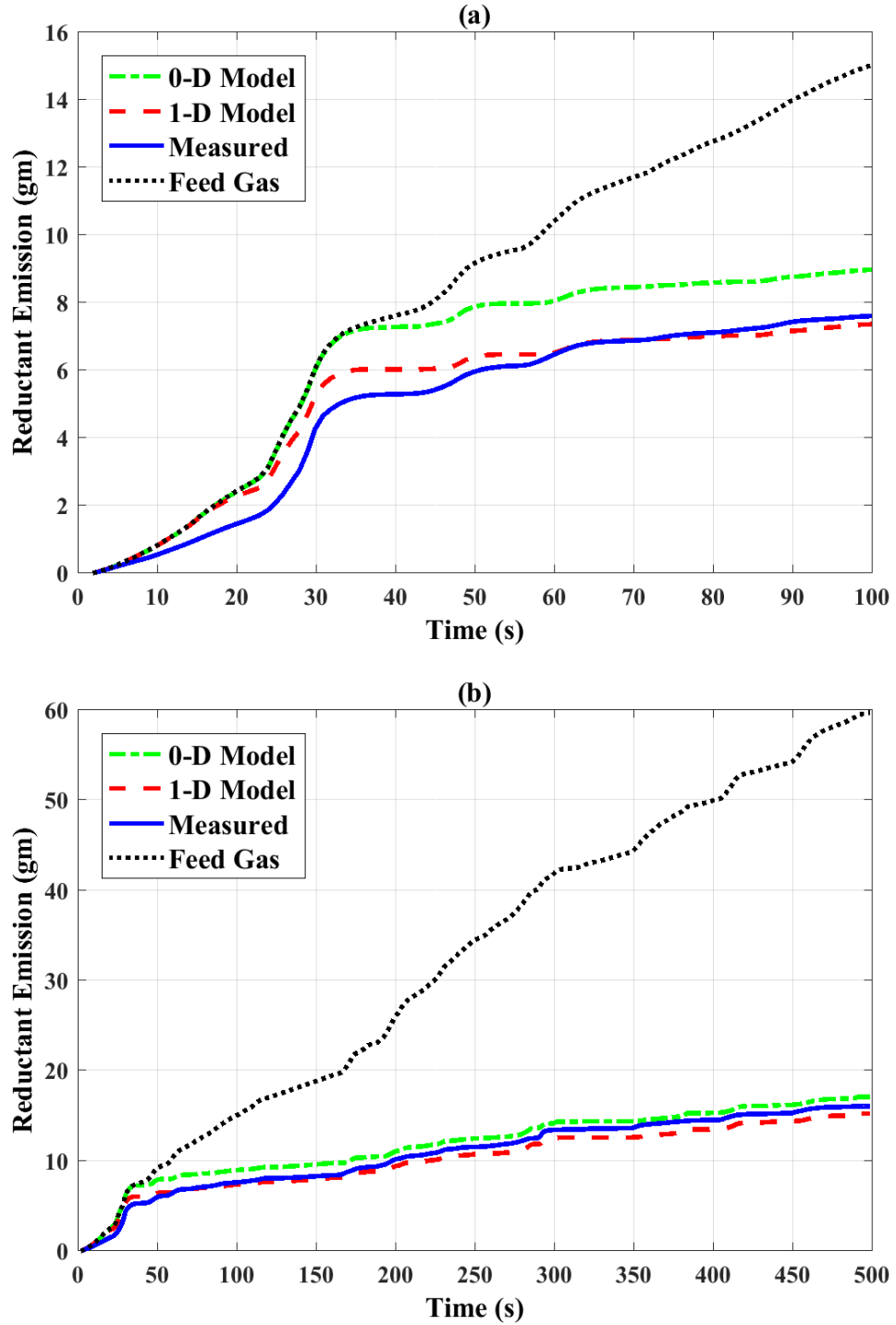


Figure 2.5: Cumulative reductant emission comparison between 1-D model and 0-D model during (a) the first 100 seconds of and (b) the entire bag 1 of an FTP cycle.

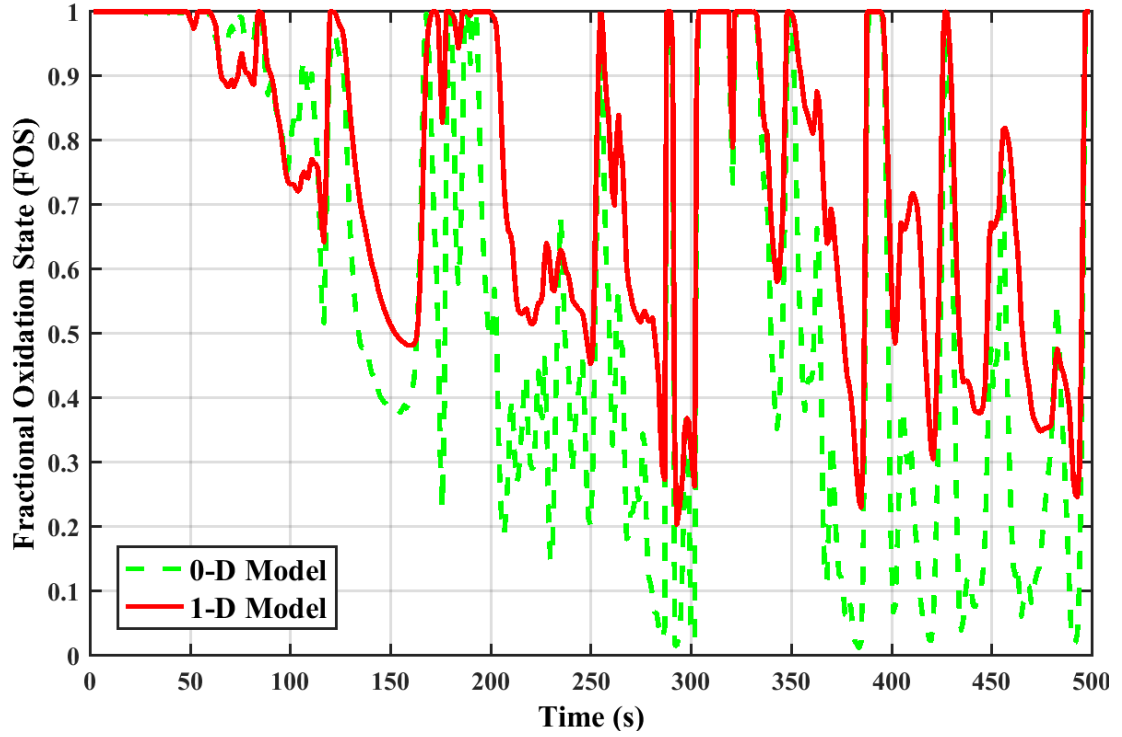


Figure 2.6: Model comparison of FOS predictions during the first 500 seconds of an FTP cycle.

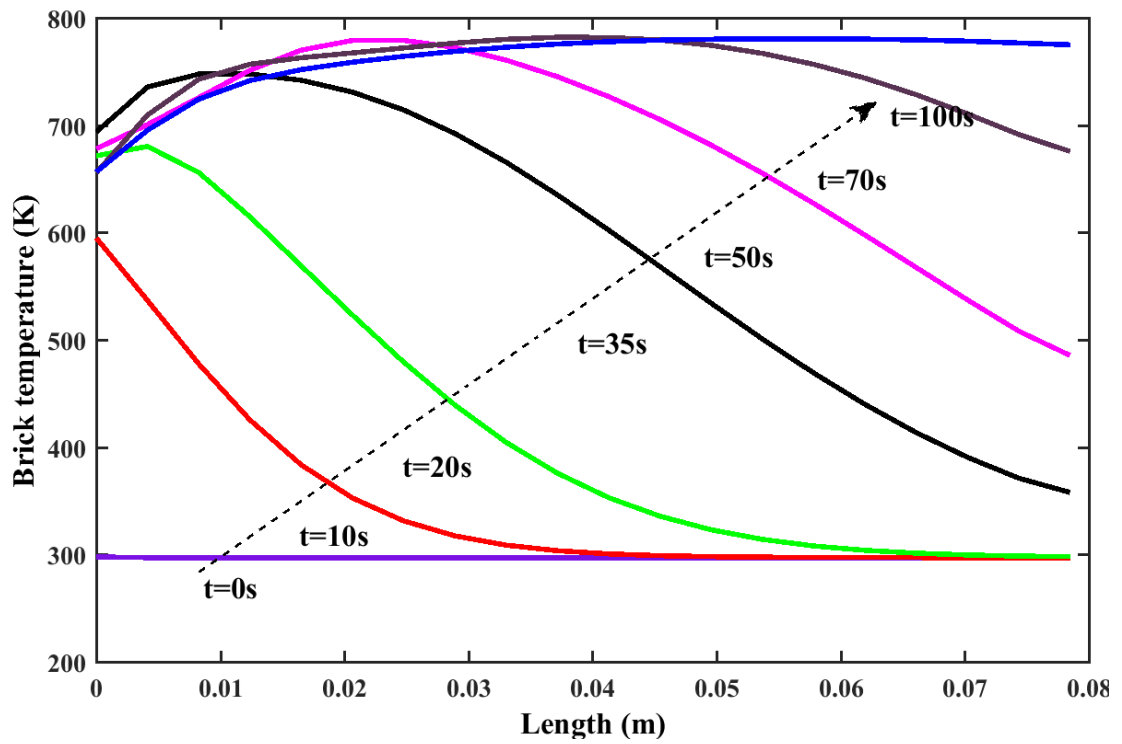


Figure 2.7: Transient temperature profiles following the cold start.

Balakotaiah, 2013; Yu et al., 2013)

$$\Delta z = 2\sqrt{\frac{2}{Pe_{h,eff}}}, \quad (2.30)$$

where  $\Delta z$  is the dimensionless width of the temperature front and  $Pe_{h,eff}$  is the effective heat Péclet number.  $Pe_{h,eff}$  depends on both axial and transverse Péclet numbers as

$$\frac{1}{Pe_{h,eff}} = \frac{1}{Pe_h} + \frac{4P}{NuLe_f}, \quad (2.31)$$

where  $Pe_h$  is the axial heat Péclet number defined as

$$Pe_h = \frac{\langle u \rangle L \rho_f C p_f R_\Omega}{k_w \delta_w}. \quad (2.32)$$

Using Eq. 2.30, constants from Table 2.3, conditions from Table 2.5 and a asymptotic Nusselt number  $Nu_\infty = 3.2$ , we can calculate that  $P = 0.0107$ ,  $Pe_h = 173$ ,  $Pe_{h,eff} = 46.6$ , thus the width of the temperature front is estimated to be about 41% of the entire length, which is consistent with Fig. 2.7.

## 2.5 Detailed Model Validation

The one-dimensional model is further validated by comparing with a detailed model in which diffusion-reaction equations in the washcoat are solved. The species balance equation in the fluid phase (for gas phase species) is given by

$$\frac{\partial \mathbf{X}_{fm}}{\partial t} = -\langle u \rangle \frac{\partial \mathbf{X}_{fm}}{\partial x} - \frac{\mathbf{k}_{me}}{R_\Omega} (\mathbf{X}_{fm} - \mathbf{X}_s), \quad (2.33)$$

where  $\mathbf{k}_{me}$  is the external mass transfer coefficient as defined by Eq. 2.15 and  $\mathbf{X}_s$  is the mole fractions at the fluid-solid interface, defined for the detailed model as

$$\mathbf{k}_{me} (\mathbf{X}_{fm} - \mathbf{X}_s) = -\mathbf{D}_s \left. \frac{\partial \mathbf{X}_{wc}}{\partial y} \right|_{y=0}. \quad (2.34)$$

The species balance in the washcoat (for gas phase species) is

$$\epsilon_w \frac{\partial \mathbf{X}_{wc}}{\partial t} = \frac{1}{C_{Total}} \boldsymbol{\nu}^T \mathbf{r} + \mathbf{D}_s \frac{\partial^2 \mathbf{X}_{wc}}{\partial y^2}. \quad (2.35)$$

The energy balance in the fluid phase is given by

$$\rho_f C_{p_f} \frac{\partial T_f}{\partial t} = -\langle u \rangle \rho_f C_{p_f} \frac{\partial T_f}{\partial x} - \frac{h}{R_\Omega} (T_f - T_s). \quad (2.36)$$

The solid temperature is assumed to be relatively uniform along the washcoat thickness and an averaged value is used. Thus the energy balance for the solid phase is

$$\delta_w \rho_w C_{p_w} \frac{\partial T_s}{\partial t} = \delta_w K_w \frac{\partial^2 T_s}{\partial x^2} + h (T_f - T_s) + \int_0^{\delta_c} \mathbf{r}^T (-\Delta \mathbf{H}) dy. \quad (2.37)$$

Ceria balance is given by

$$\frac{\partial \theta}{\partial t} = \frac{1}{2TOSC} (r_2 - r_3). \quad (2.38)$$

The initial and boundary conditions are

$$X_{fm,j}(x, 0) = X_{fm,j}^0(x), \quad X_{wc,j}(x, y, 0) = X_{wc,j}^0(x, y), \quad (2.39)$$

$$T_f(x, 0) = T_f^0(x), \quad T_s(x, 0) = T_s^0(x), \quad (2.40)$$

$$\theta(x, y, 0) = \theta^0(x, y), \quad (2.41)$$

$$X_{fm,j}(0, t) = X_{fm,j}^{in}(t), \quad T_f(0, t) = T_f^{in}(t), \quad (2.42)$$

Table 2.5: Simulation conditions

Variable	Value
$u$	$2 \text{ m} \cdot \text{s}^{-1}$
$T_f^0$	300 K
$T_s^0$	300 K
$\theta^0$	0
$X_{f,A}^{in}$	2%
$X_{f,O_2}^{in}$	1%
$T_f^{in}$	650 K

$$\left. \frac{\partial T_s}{\partial x} \right|_{x=0} = 0, \quad \left. \frac{\partial T_s}{\partial x} \right|_{x=L} = 0, \quad \text{and} \quad (2.43)$$

$$\mathbf{X}_{wc}|_{y=0} = \mathbf{X}_s, \quad \left. \frac{\partial \mathbf{X}_{wc,j}}{\partial y} \right|_{y=\delta_c} = \mathbf{0}. \quad (2.44)$$

As shown above, the 1-D model is helpful especially in cold start where axial temperature gradient is significant. In order to validate the model's cold start predictions, simulation conditions are selected to be approximately the average values during the first 60 seconds of an FTP cycle, shown below in Table 2.5. The kinetic model used is shown in Table 2.4.

Shown in Fig. 2.9, 2.8 and 2.10 are the comparisons between the results of the detailed model, the 1-D model using different approximations of internal mass transfer coefficient and the 0-D model proposed in Kumar et al. (2012). The solid black curve represents the result of the detailed model. The solid pink curve shows the result of the 0-D model, which gives significant error for the selected conditions. The dotted red curve represents the 1-D model using asymptotic internal Sherwood number of 2.6 for  $k_{mi}$ . Shown by the dash-dotted green curve is the infinite  $k_{mi}$  case, which implies no washcoat diffusion limitation. This leads to  $k_{mo} = k_{me}$  in Eqs. 2.1 and 2.2, which is commonly used in the literature where washcoat diffusion is not considered. The dashed blue curve represents the case where the internal mass transfer coefficient is estimated using the method proposed in Eqs. 2.19-2.25, which is the most accurate approximation for the detailed model comparing to the other cases.

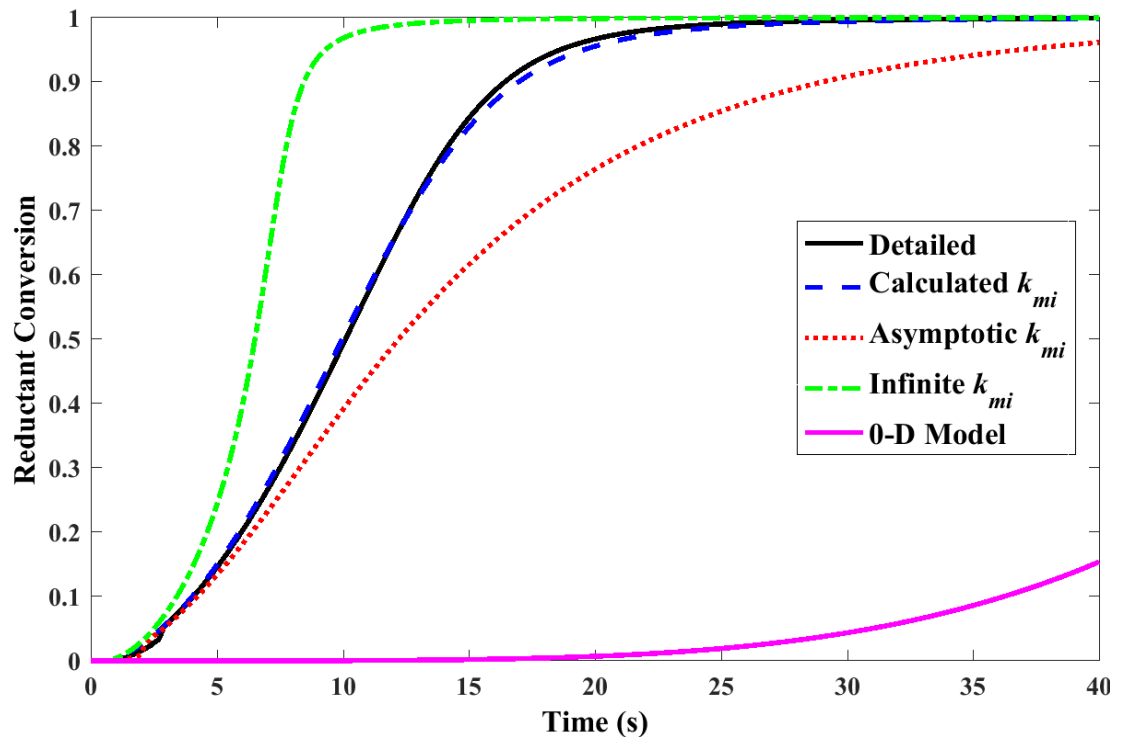


Figure 2.8: Model comparison of reductant conversions.

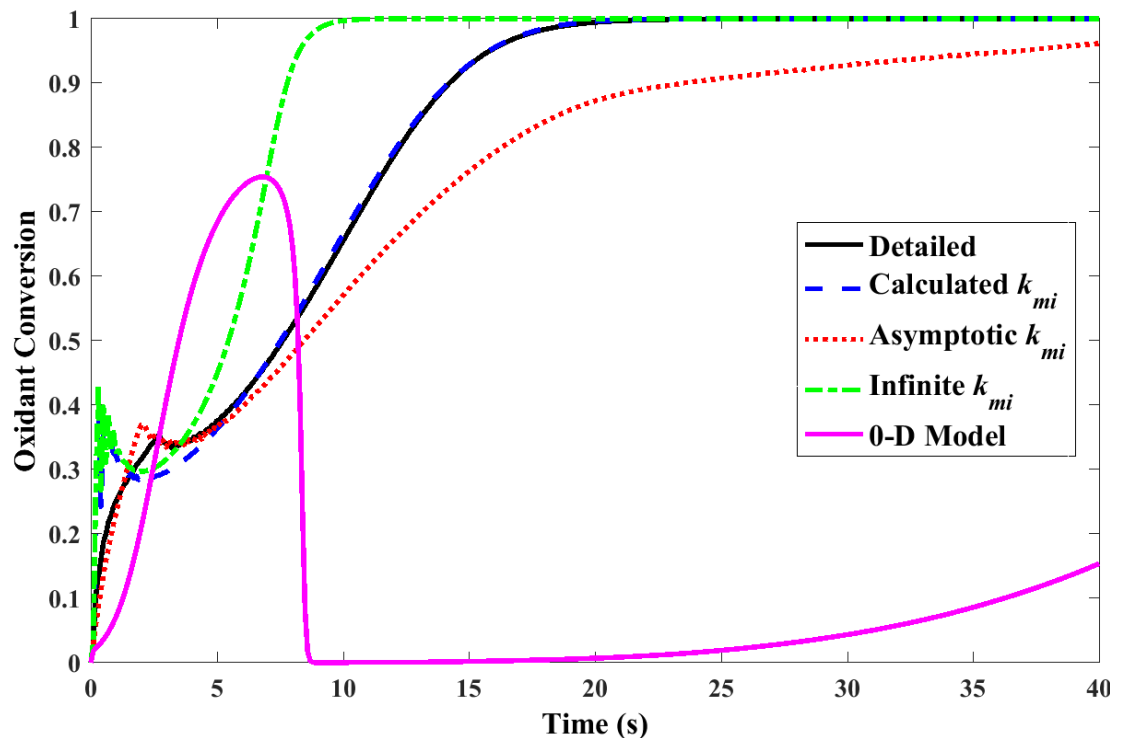


Figure 2.9: Model comparison of oxidant conversions.

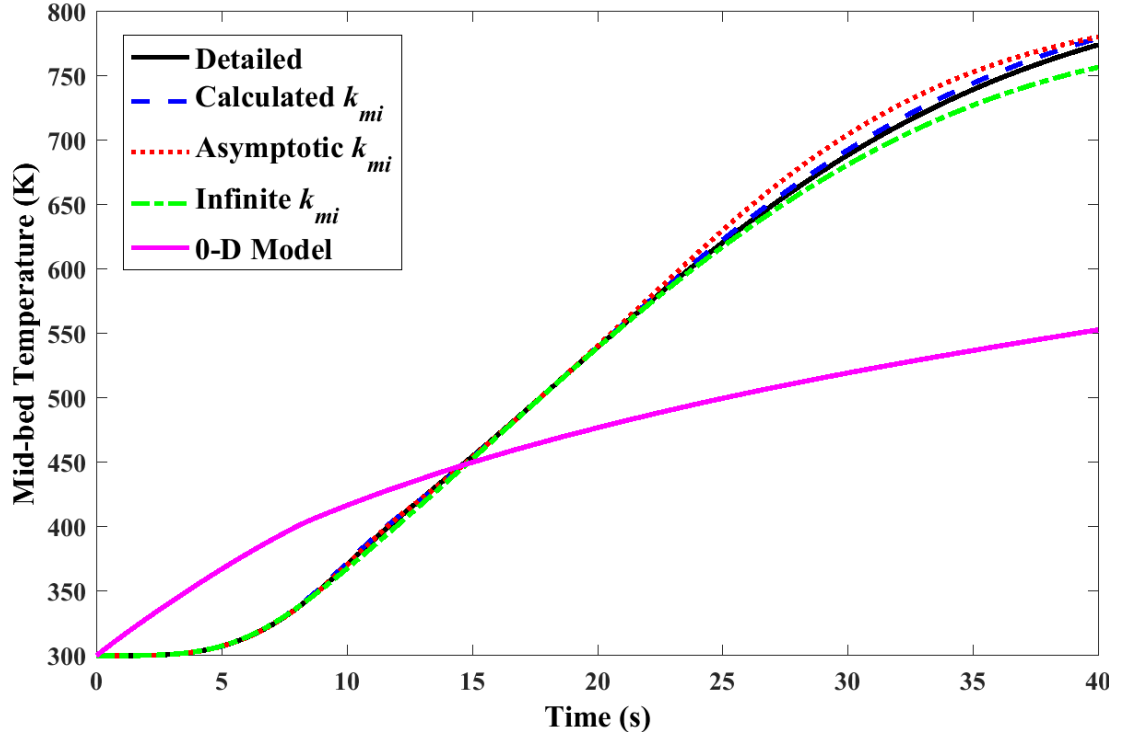


Figure 2.10: Model comparison of mid-bed temperatures.

In Fig. 2.9, we can see that all models predict a peak oxidant conversion in the first several seconds, while Fig. 2.8 shows practically zero reductant conversion during the same period of time. This indicates the ignition of oxygen storage reaction. The kinetic model used here (Table 2.2) predicts a lower ignition temperature for oxygen storage reaction than for the direct catalytic reaction.

Shown in Fig. 2.10 is the transient mid-bed temperature where the detailed model and 1-D models give almost the same temperature profile. The mid-bed temperature stays low till the temperature wave front reaches mid-bed. The brick is gradually heated by the fluid, then the reactions are ignited and the temperature increases much faster till it reaches steady-state. On the other hand, the 0-D model predicts qualitatively different behavior. Because of axial averaging, local reaction heat is distributed over the brick causing slow temperature rise and the reactions ignite only after the whole brick reaches ignition temperature resulting in a late ignition prediction.

## 2.6 Oxygen Storage Dynamics

The true fractional oxidation state (FOS) of the catalyst can't be directly measured, but it can be estimated using fundamental-based TWC models. Different model structures using separately identified kinetic parameters could have similar good agreements in emission predictions, but produce different FOS estimations. The 0-D model proposed in Kumar et al. (2012) is capable of predicting emissions and FOS trends for various driving cycles, but as a result of axially averaging, it cannot capture all the dynamic features of the TWC oxygen storage especially when temperature or concentration gradient is significant. One example of such case is cold start, another example is fast lean-rich cycling resulting from current engine and TWC control strategy. Taking the spatial variations into account, the 1-D model can retain all these dynamic features not only qualitatively, but also with good quantitative accuracy.

Shown in Fig. 2.11 are averaged FOS results given by different models under cold start conditions listed in Table 2.5. The 1-D model correctly predicts the trend of FOS dynamics, while the 0-D model predicts late ignition and high steady-state FOS. Fig. 2.12 further illustrates that the 1-D model can retain the spatial effect during cold start very well.

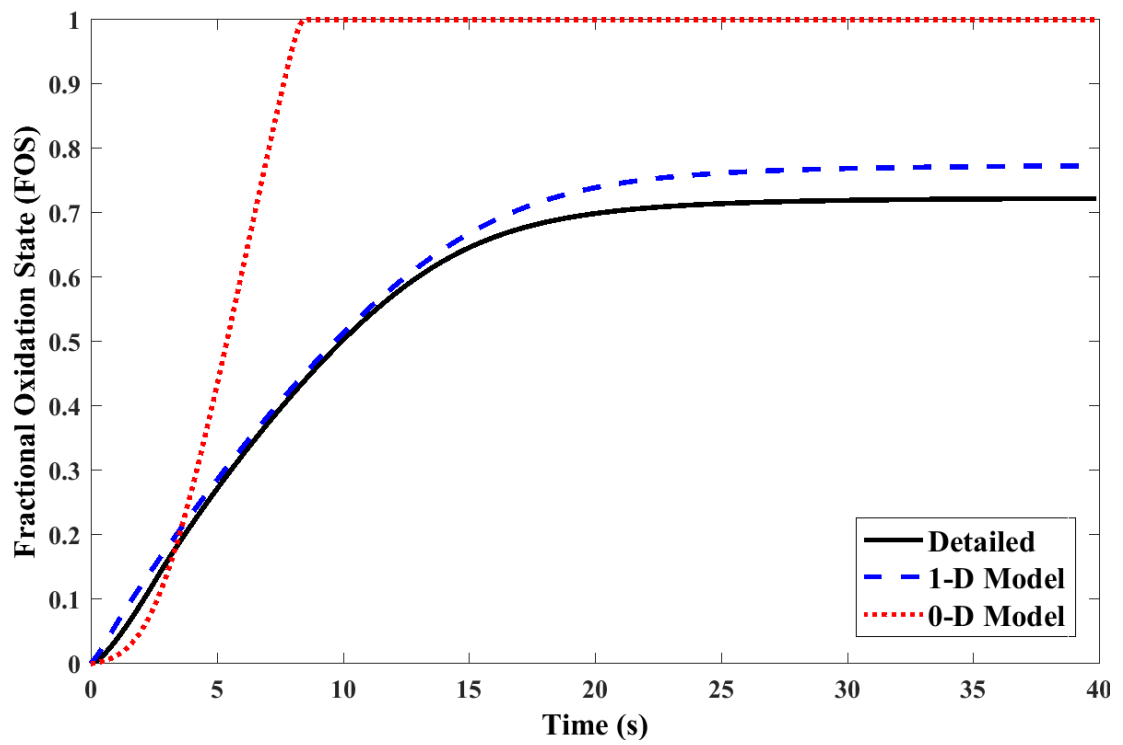


Figure 2.11: Model comparison of FOS dynamics under cold start condition.

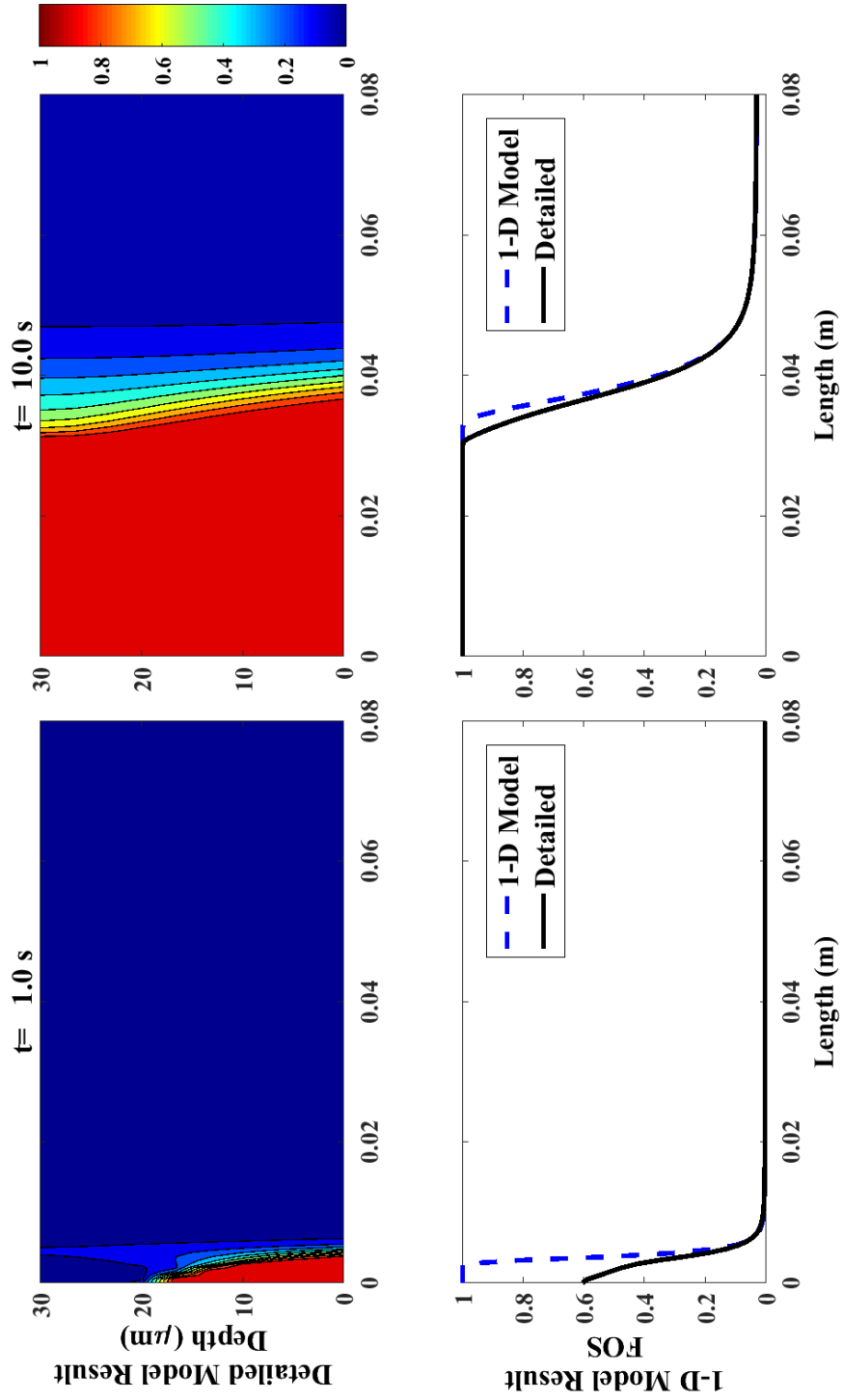


Figure 2.12: Spatial FOS profile under cold start condition.

Table 2.6: Fast cycling conditions

Variable	Value
$u$	$2 \text{ m} \cdot \text{s}^{-1}$
$T_f^0$	650 K
$T_s^0$	650 K
$\theta^0$	0
$X_{f,A}^{in}$	1% / 3%
$X_{f,O_2}^{in}$	1.5% / 0.5%
$T_f^{in}$	650 K

Fast lean-rich cycling is commonly seen in engine operations. Control systems are designed to control gasoline engine to operate around stoichiometry, while slight excursions are often observed, which results in a constant lean-rich cycling. When the cycling is fast and the gas flow rate is relatively small, we can anticipate that only the front part of the TWC will be responsive to the cycling. Thus, the 0-D model will fail to capture the partial response effect. Fast cycling simulation conditions are shown in Table 2.6. The brick is initially hot with no oxygen stored. Feed cycles between lean ( $\lambda = 1.05$ ) and rich ( $\lambda = 0.95$ ) every 2 seconds.

In Fig. 2.13, we can see that the 1-D model FOS prediction agrees well with detailed model result. After about 25 seconds the system reaches periodic steady state where only the front part of the TWC is storing and releasing oxygen while the FOS after the front part stays the same as shown in Fig. 2.14. Because of axially lumping, the whole brick will response to the cycling in the 0-D model, thus the periodic steady FOS will be either near 1 or 0, which is different from the detailed model.

The initial FOS ( $\theta^0$ ) in both cold start and fast cycling simulations are set to be zero in order to study the TWC behavior when stored oxygen is depleted and reductant emissions are most likely to break through. However, in actual driving conditions, the fuel is shut off while the air flows during a cold start, resulting in a lean feed gas which can potentially oxidize the ceria in the catalyst. To study

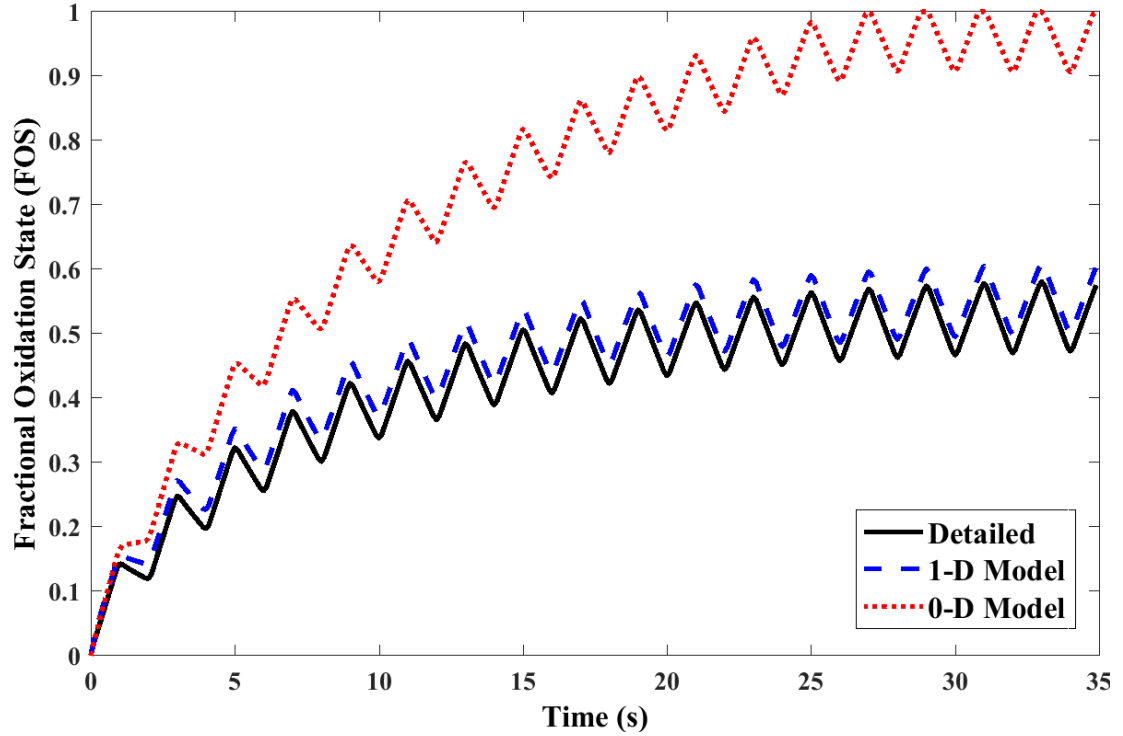


Figure 2.13: Model comparison of FOS dynamics during fast lean-rich cycling.

such case, cold start and fast cycling simulations with full initial oxygen storage ( $\theta^0 = 1$ ) are also conducted. The model results show similar behavior in emission and temperature predictions as the zero initial FOS case, but the 0-D model can provide accurate estimation of FOS in this case since the amplitude of the cycling is small and FOS is varying close to one.

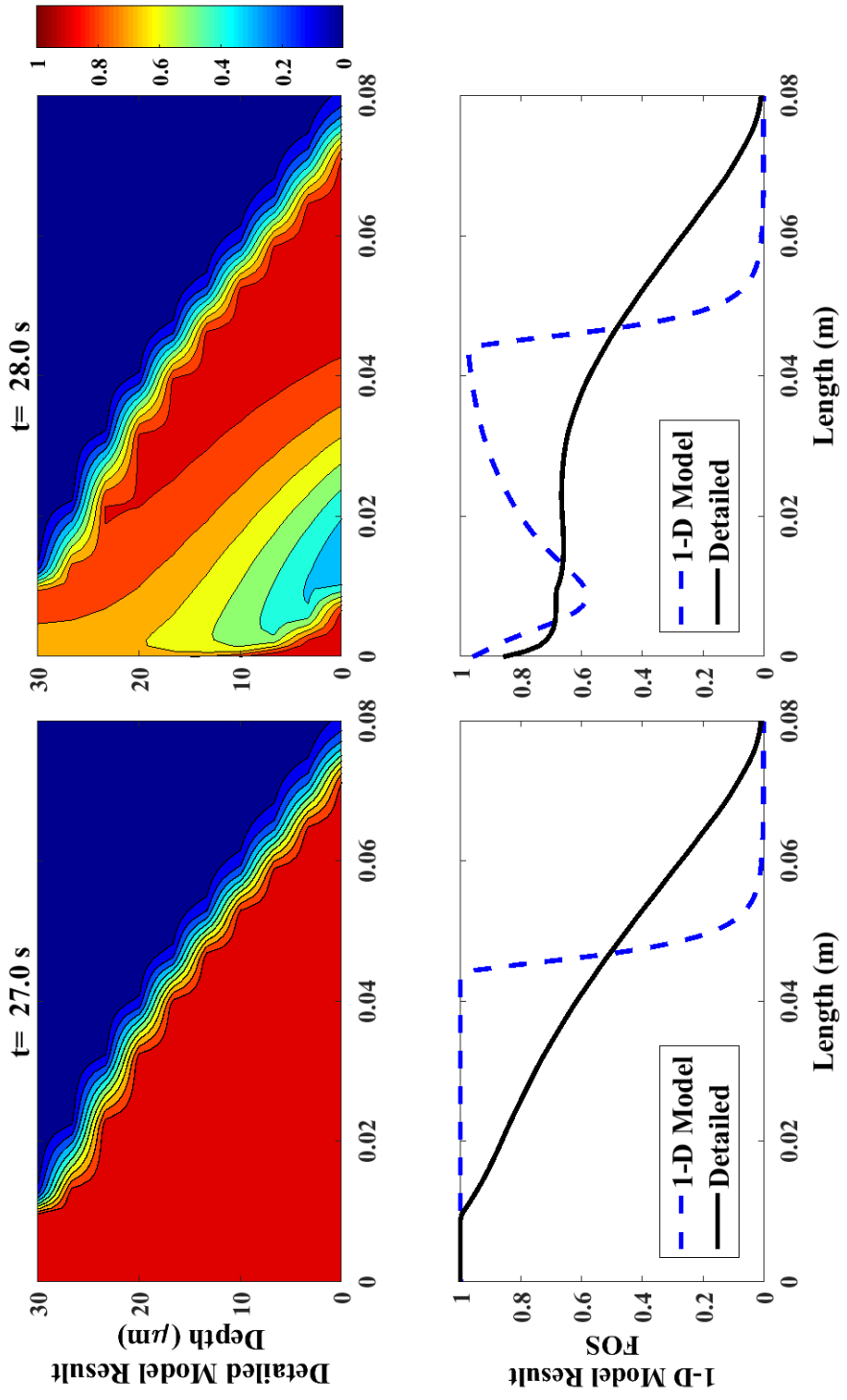


Figure 2.14: Spatial FOS profile during fast lean-rich cycling.

## 2.7 Summary

In this part, we developed and validated a physics-based reduced order seven partial differential equation model for describing the spatio-temporal dynamics of oxygen storage and release as well as the cold-start behavior of a TWC. The proposed model retains the simplified chemistry and washcoat diffusion approximations used in the earlier lumped model of Kumar et al. (2012) but relaxes the axial lumping approximation. The proposed TWC model is validated using emissions data collected in a vehicle over multiple drive cycles including FTP cycles. The internal mass transfer approximation is confirmed by comparing with a detailed washcoat diffusion–reaction model and is observed to be consistent for all practical purposes. As shown in this work, axial gradients in the temperature and stored oxygen profile cannot be neglected during cold start, fast lean to rich cycling or sudden and significant changes in the inlet conditions to the TWC.

## **Part II**

# **Scale-up Analysis of Monolith Reactors**

# Chapter 3

## Introduction and Literature Review

The monolith reactor is the most widely used man-made reactor in the world. While the exact number of units is unknown, it is estimated that there are about one billion monolith reactors used in the treatment of emissions from automobiles alone (e.g. three-way converters, TWCs; diesel oxidation converters, DOCs; lean-NOx traps, LNTs; selective catalytic reduction units, SCRs; ammonia slip converters, ASCs and so forth.) It consists of a honeycomb structure with a large number of straight parallel channels of small hydraulic diameter (0.5-6 mm) through which the fluid flows. The substrate of the monoliths used in automobile exhaust after-treatment is made up of either ceramic, which has lower thermal conductivity ( $0.8\text{-}2 \text{ W} \cdot \text{m}^{-1} \cdot \text{K}^{-1}$ ), or metallic, which is made up of ferritic steels with higher thermal conductivity ( $10\text{-}30 \text{ W} \cdot \text{m}^{-1} \cdot \text{K}^{-1}$ .) The catalytic materials (alumina washcoat containing precious metals such as Pt/Pd/Rh and storage materials such as Ce/Ba or zeolite particles mixed with binders) are deposited on the substrate in the form of one or more layers with thickness in the range of  $10\text{-}50 \text{ }\mu\text{m}$  for each layer. In addition to their use in pollution abatement, monolith reactors are also finding applications in the chemical industry as a replacement for the traditional packed-bed reactor.

The performance of various catalyst formulations in treating the emissions from automobiles is often tested in laboratory experiments using monolith samples of the same cell density, washcoat layer thickness, and catalyst composition and loading but with a smaller length scale (typically 1-2 cm in length) compared to full-scale systems (10-30 cm). The flow rate in the laboratory-scale operation is selected such that the space velocity is the same as that in the full-scale system [In addition to various measurement conveniences, the smaller length and flow rate used in laboratory-scale

operation is to minimize the amount of synthetic exhaust gases used and hence the cost of experiments.] It is hoped that matching the catalyst geometrical properties and space velocity ensures similarity between the laboratory-scale and full-scale systems. However, the conditions for similarity between these two systems have not been validated with any analysis or computation or direct experimental comparison. This lack of validation is the motivation for this study.

While the general principles of scale-up in engineering are well known (Zlokarnik, 2002) (e.g. matching of various dimensionless groups impacting the process), application requires the identification of all the relevant independent variables, which are case dependent. In the context of catalytic reactors in which the same catalyst and fluid is used, it is known that the performance of reactors with different physical scales could be different for the following reasons: (i) fluid flow patterns are not similar (ii) heat and mass dispersion effects are different (iii) the concentrations and temperature ranges used are different, and (iv) the external conditions such as heat exchange with surroundings are different at the two scales.

The impact of fluid flow pattern on reactor performance is well documented in the chemical engineering literature (Froment et al, 2010) and is not reviewed here as it is not the focus of the present work. Fig. 3.1 shows schematic diagrams of a typical laboratory-scale and a full-scale monolith reactor. We note that similarity may not exist between the two systems if the flow conditions before entrance to the monolith channels are not the same, even if the flow becomes laminar after entering the channels and the channels in the two systems are identical (e.g. turbulent flow in the duct of the large scale unit but laminar in the smaller scale). In the present work, we assume uniform flow conditions before entrance to the channels (and hence hydrodynamic similarity exists between the two scales) and focus only on the remaining causes of scale-up failure.

The main goal of this part is to analyze in some detail the impact of heat and

mass dispersion, thermal effects (adiabatic temperature rise or use of different inlet concentrations) and heat losses from the reactor on the scale-up of monolith reactors used in the exhaust after-treatment as well as other applications.

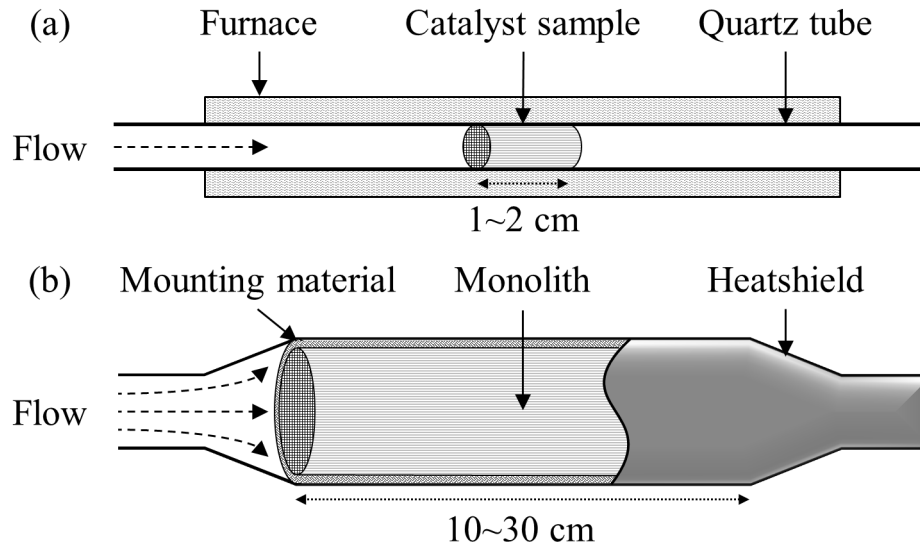


Figure 3.1: Schematic diagrams of (a) a lab-scale reactor and (b) a full-scale reactor.

# Chapter 4

## Model Development

As hydrodynamic similarity between the two scales is assumed, we need to consider only species and energy balance equations in order to examine the impact of heat and mass dispersion and thermal effects on scale-up. For the adiabatic case, this can be done by considering the model of a single channel provided the flow distribution to the various channels is identical. Fig. 4.1a shows a schematic diagram of the cross-section of a monolith channel with a single washcoat layer. Other than square-shaped channels, which are most commonly found, ceramic monolith reactors are also made with triangular and hexagonal channels for either higher mechanical strength or lower back pressure (Heck et al., 2009). Bhattacharya et al. (2004) showed that channels of various shapes can be treated by a single model through proper shape normalization. Using effective washcoat thickness and assuming azimuthal symmetry, monolith channel of arbitrary shape may be treated as a circular channel, and a two-dimensional model is obtained. In this work, we assume that geometric similarity exists and consider an equivalent axisymmetric system with a circular flow channel and uniformly thick washcoat and wall layers (as shown in Fig. 4.1b). This approximation is justified since we have already assumed that geometric similarity exists between the channels of the two scales and the differences are mainly due to axial length scales. Thus, we start from a detailed two-dimensional (axisymmetric) model to determine and compare the relevant dimensionless groups in both lab-scale and full-scale systems. Based on this comparison, the model is further simplified by lumping the various dimensionless groups that are matched in lab- and full-scale systems. In this way, we can examine all the quantitative and qualitative differences between two scales without introducing unnecessary complexity in the model.

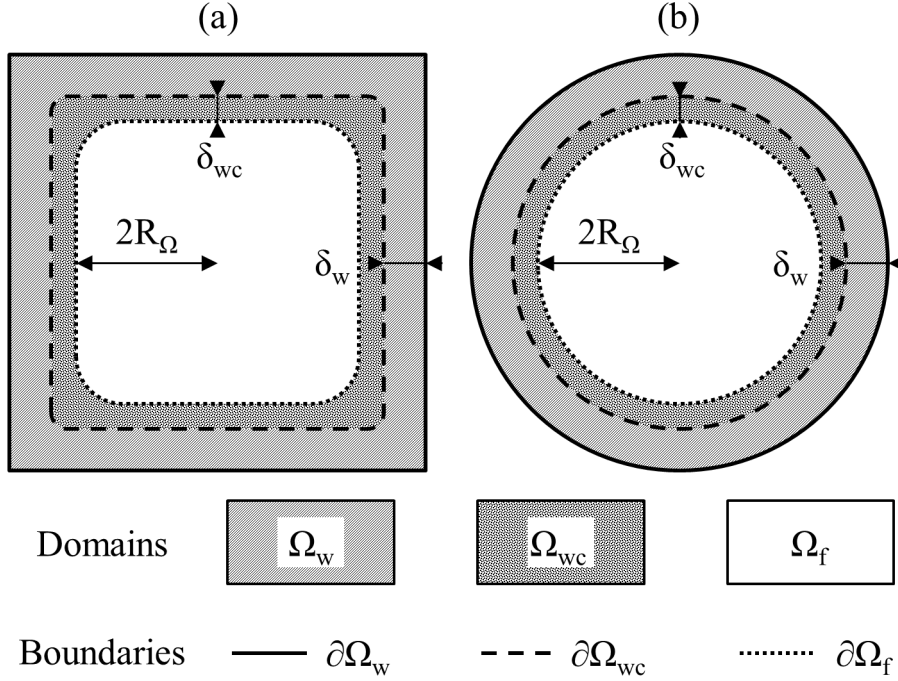


Figure 4.1: Schematic diagram of the cross-section of (a) a single monolith channel and (b) axisymmetric approximation for modeling.

## 4.1 Two-dimensional Monolith Model

As shown in Fig. 4.1, the monolith channel is divided into three domains – flow channel ( $\Omega_f$ ), catalytic washcoat ( $\Omega_{wc}$ ) and substrate wall ( $\Omega_w$ ). The feed gas flows axially through the monolith channel while mass and heat are transported in both axial and radial directions by convection and diffusion. We distinguish between the washcoat and the substrate wall because heat is only generated in the washcoat where reactions take place. The model can be applied to the case of multiple species and reactions, but here we consider only one limiting reactant with one reaction because the focus is to compare reactor performances instead of kinetic models.

The model equations are derived from species and energy balances in each domain.

The species balance in the flow channel is given by

$$\frac{\partial C_f}{\partial t} + u(r) \frac{\partial C_f}{\partial x} = D_f \nabla_{\perp}^2 C_f + D_f \frac{\partial^2 C_f}{\partial x^2} \text{ in } \Omega_f, 0 < x < L, t > 0. \quad (4.1)$$

The species balance in the washcoat is

$$\epsilon_{wc} \frac{\partial C_{wc}}{\partial t} = D_{wc} \nabla_{\perp}^2 C_{wc} + D_{wc} \frac{\partial^2 C_{wc}}{\partial x^2} - R(C_{wc}, T_{wc}) \text{ in } \Omega_{wc}. \quad (4.2)$$

Here,  $C_f$  and  $C_{wc}$ , represent reactant concentrations in the fluid phase and the washcoat, respectively. The species balance in the substrate wall is not considered since there is no reaction in that domain and the molecular diffusivity in the substrate is much smaller than other domains. Here,  $R(C_{wc}, T_{wc})$  is the reaction rate per unit volume of the washcoat;  $D_f$ ,  $D_{wc}$  are molecular diffusivities of the reactant in the fluid phase and the washcoat, respectively;  $L$  is the length of the reactor and  $\epsilon_{wc}$  is the porosity of the washcoat. Assuming the flow is laminar and fully developed, the fluid velocity profile  $u$  is only a function of the radial position  $r$ ,

$$u(r) = 2\bar{u} \left( 1 - \frac{r^2}{4R_{\Omega}^2} \right), 0 < r < 2R_{\Omega},$$

in which  $\bar{u}$  is the average fluid velocity and  $R_{\Omega}$  is the hydraulic radius of the flow channel  $\Omega_f$  (half of the geometric radius for a circular channel). The initial and boundary conditions for the species balances are given by

$$C_f = C_f^0(x, r), C_{wc} = C_{wc}^0(x, r) \text{ at } t = 0, \quad (4.3a)$$

$$D_f \mathbf{n}_{\Omega_f} \cdot \nabla_{\perp} C_f = D_{wc} \mathbf{n}_{\Omega_f} \cdot \nabla_{\perp} C_{wc}, C_f = C_{wc} \text{ on } \partial\Omega_f, \quad (4.3b)$$

$$\mathbf{n}_{\Omega_{wc}} \cdot \nabla_{\perp} C_{wc} = 0 \text{ on } \partial\Omega_{wc}; \quad (4.3c)$$

$$D_f \frac{\partial C_f}{\partial x} = u (C_f - C_f^{in}(t)), \quad \frac{\partial C_{wc}}{\partial x} = 0 \text{ at } x = 0, \text{ and} \quad (4.3d)$$

$$\frac{\partial C_f}{\partial x} = \frac{\partial C_{wc}}{\partial x} = 0 \text{ at } x = L. \quad (4.3e)$$

Here,  $\nabla_{\perp}$  and  $\nabla_{\perp}^2$  are transverse gradient and Laplacian operators;  $\mathbf{n}_{\Omega_f}$  and  $\mathbf{n}_{\Omega_{wc}}$  are unit normal vectors radially outward to the fluid-washcoat interface  $\partial\Omega_f$  ( $r = 2R_{\Omega}$ ) and the washcoat-substrate interface  $\partial\Omega_{wc}$  ( $r = 2R_{\Omega} + \delta_{wc}$ ), respectively. Bold symbols are used to represent vectors.

The energy balance in the fluid phase is given by

$$\rho_f C_p \left( \frac{\partial T_f}{\partial t} + u(r) \frac{\partial T_f}{\partial x} \right) = k_f \nabla_{\perp}^2 T_f + k_f \frac{\partial^2 T_f}{\partial x^2} \text{ in } \Omega_f. \quad (4.4)$$

The energy balance in the washcoat is

$$\rho_{wc} C_p \frac{\partial T_{wc}}{\partial t} = k_{wc} \nabla_{\perp}^2 T_{wc} + k_{wc} \frac{\partial^2 T_{wc}}{\partial x^2} + (-\Delta H) R(C_{wc}, T_{wc}) \text{ in } \Omega_{wc}, \quad (4.5)$$

and the energy balance in the substrate can be expressed as

$$\rho_w C_p \frac{\partial T_w}{\partial t} = k_w \nabla_{\perp}^2 T_w + k_w \frac{\partial^2 T_w}{\partial x^2} \text{ in } \Omega_w. \quad (4.6)$$

Here,  $T$  represents temperature,  $\rho$  and  $C_p$  are density and specific heat capacity, and  $k$  is thermal conductivity. The subscript  $f$  stands for the fluid phase,  $wc$  and  $w$  represent the washcoat and the substrate wall, respectively.  $\Delta H$  is the heat of reaction. The initial and boundary conditions for the energy balances are given by

$$T_f = T_f^0(x, r), \quad T_{wc} = T_{wc}^0(x, r), \quad T_w = T_w^0(x, r) \text{ at } t = 0, \quad (4.7a)$$

$$k_f \mathbf{n}_{\Omega_f} \cdot \nabla_{\perp} T_f = k_{wc} \mathbf{n}_{\Omega_f} \cdot \nabla_{\perp} T_{wc}, \quad T_f = T_{wc} \text{ on } \partial\Omega_f, \quad (4.7b)$$

$$k_{wc} \mathbf{n}_{\Omega_{wc}} \cdot \nabla_{\perp} T_{wc} = k_w \mathbf{n}_{\Omega_{wc}} \cdot \nabla_{\perp} T_w, \quad T_{wc} = T_w \text{ on } \partial\Omega_{wc}, \quad (4.7c)$$

$$\mathbf{n}_{\Omega_w} \cdot \nabla_{\perp} T_w = 0 \text{ on } \partial\Omega_w, \quad (4.7d)$$

$$\frac{k_f}{\rho_f C_{p_f}} \frac{\partial T_f}{\partial x} = u (T_f - T_f^{in}(t)), \quad \frac{\partial T_{wc}}{\partial x} = \frac{\partial T_w}{\partial x} = 0 \text{ at } x = 0, \text{ and} \quad (4.7e)$$

$$\frac{\partial T_f}{\partial x} = \frac{\partial T_{wc}}{\partial x} = \frac{\partial T_w}{\partial x} = 0 \text{ at } x = L. \quad (4.7f)$$

Here,  $\mathbf{n}_{\Omega_w}$  is the unit normal vector radially outward to the substrate boundary  $\partial\Omega_w$  ( $r = 2R_{\Omega} + \delta_{wc} + \delta_w$ );  $\delta_{wc}$  is the thickness of the washcoat and  $\delta_w$  is half-thickness of the substrate wall. [Remark: The boundary conditions for the fluid phase in Eqs. 4.3d,4.3e,4.7e and 4.7f represent the so called "Danckwerts boundary conditions". (Froment et al., 2010)]

Cycling experiments are commonly conducted to evaluate after-treatment catalyst performance, where inlet concentrations and/or fluid temperature are varied periodically. In such cases, the inlet conditions ( $C_f^{in}$  and  $T_f^{in}$ ) are periodic functions of time. Here, we take sinusoidal functions as an example,

$$C_f^{in}(t) = \bar{C}_f^{in} (1 + \varepsilon_C \sin(2\pi\omega t)),$$

$$T_f^{in}(t) = \bar{T}_f^{in} (1 + \varepsilon_T \sin(2\pi\omega t)),$$

where  $\bar{C}_f^{in}$  and  $\bar{T}_f^{in}$  are cycle averaged values of inlet concentration and fluid temperature;  $\varepsilon_C$  and  $\varepsilon_T$  are relative cycling amplitude of inlet concentration and fluid temperature, respectively;  $\omega$  is the cycling frequency which is usually the same for both inlet concentration and fluid temperature. For steady-state experiments,  $\varepsilon_C = \varepsilon_T = 0$ ,  $C_f^{in} = \bar{C}_f^{in}$ ,  $T_f^{in} = \bar{T}_f^{in}$ .

## 4.2 Dimensionless Groups

As stated in the introduction, scale-up problems are usually studied by comparing various dimensionless groups. If two reactors have all dimensionless groups matched,

Table 4.1: Characteristic scales

<i>Scale</i>	<i>Definition</i>	<i>Description</i>
Time	$\tau = L/\bar{u}$	Space time (s)
Axial length	$L$	Reactor length (m)
Transverse length	$R_\Omega$	Hydraulic radius (m)
Concentration	$\bar{C}_f^{in}$	Inlet concentration (mol · m <sup>-3</sup> )
Temperature	$\Delta T_{ad} = \frac{(-\Delta H)\bar{C}_f^{in}}{\rho_f C_{p_f}}$	Adiabatic temperature rise (K)

the mathematical models will become identical indicating that the performances of these two reactors will also be identical. We define characteristic scales as shown in Table 4.1, then non-dimensionalized the variables, operators and inlet conditions accordingly,

$$\hat{t} = \frac{t}{\tau}, z = \frac{x}{L}, \xi = \frac{r}{R_\Omega}, y = \frac{C}{\bar{C}_f^{in}}, \hat{T} = \frac{T - \bar{T}_f^{in}}{\Delta T_{ad}}, \theta^{in} = \frac{\bar{T}_f^{in}}{\Delta T_{ad}}, \widehat{\nabla}_\perp = R_\Omega \nabla_\perp, \widehat{\nabla}_\perp^2 = R_\Omega^2 \nabla_\perp^2,$$

Notice that instead of introducing a predefined reference temperature, we use the adiabatic temperature rise as the temperature scale. In this way, the dimensionless temperature rise  $\hat{T}$  has the same order of magnitude as the conversion  $\chi = 1 - y$ . The adiabatic temperature rise can also be rewritten as

$$\Delta T_{ad} = \frac{(-\Delta H)\bar{C}_f^{in}}{\rho_f C_{p_f}} = \frac{(-\Delta H)\bar{X}_f^{in}}{\widehat{C}_{p_f}},$$

where  $\widehat{C}_{p_f}$  is the molar heat capacity of the fluid which can be assumed constant for dilute reactant,  $\bar{X}_f^{in}$  is the average inlet mole fraction of the limiting reactant. For a given reaction, the adiabatic temperature rise is proportional to  $\bar{X}_f^{in}$ , so all results involving  $\Delta T_{ad}$  can also be interpreted in terms of  $\bar{X}_f^{in}$  in the following sections. Substituting the dimensionless variables in the equations, some important dimensionless groups appear in the governing equations and inlet/boundary conditions. The model

equations may be expressed as

$$\frac{\partial y_f}{\partial \hat{t}} + 2 \left(1 - \frac{1}{4} \xi^2\right) \frac{\partial y_f}{\partial z} = \frac{1}{P_{m,f}} \widehat{\nabla}_{\perp}^2 y_f + \frac{1}{Pe_{m,f}} \frac{\partial^2 y_f}{\partial z^2}, \quad (4.8)$$

$$\epsilon' \frac{\partial y_{wc}}{\partial \hat{t}} = \frac{1}{P_{m,wc}} \widehat{\nabla}_{\perp}^2 y_{wc} + \frac{1}{Pe'_{m,wc}} \frac{\partial^2 y_{wc}}{\partial z^2} - Da'_0 y_{wc} \exp\left(\frac{-1/\beta}{\widehat{T}_{wc} + \theta^{in}}\right), \quad (4.9)$$

$$\frac{\partial \widehat{T}_f}{\partial \hat{t}} + 2 \left(1 - \frac{1}{4} \xi^2\right) \frac{\partial \widehat{T}_f}{\partial z} = \frac{1}{P_{h,f}} \widehat{\nabla}_{\perp}^2 \widehat{T}_f + \frac{1}{Pe_{h,f}} \frac{\partial^2 \widehat{T}_f}{\partial z^2}, \quad (4.10)$$

$$\sigma_{wc} \frac{\partial \widehat{T}_{wc}}{\partial \hat{t}} = \frac{1}{P_{h,wc}} \widehat{\nabla}_{\perp}^2 \widehat{T}_{wc} + \frac{1}{Pe'_{h,wc}} \frac{\partial^2 \widehat{T}_{wc}}{\partial z^2} + Da'_0 y_{wc} \exp\left(\frac{-1/\beta}{\widehat{T}_{wc} + \theta^{in}}\right), \text{ and} \quad (4.11)$$

$$\sigma_w \frac{\partial \widehat{T}_w}{\partial \hat{t}} = \frac{1}{P_{h,w}} \widehat{\nabla}_{\perp}^2 \widehat{T}_w + \frac{1}{Pe'_{h,w}} \frac{\partial^2 \widehat{T}_w}{\partial z^2}, \quad (4.12)$$

with initial and boundary conditions,

$$y_f = y_f^0(z, \xi), \quad y_{wc} = y_{wc}^0(z, \xi) \quad \text{at } \hat{t} = 0, \quad (4.13a)$$

$$\widehat{T}_f = \widehat{T}_f^0(z, \xi), \quad \widehat{T}_{wc} = \widehat{T}_{wc}^0(z, \xi), \quad \widehat{T}_w = \widehat{T}_w^0(z, \xi) \quad \text{at } \hat{t} = 0, \quad (4.13b)$$

$$\frac{1}{P_{m,f}} \mathbf{n}_{\Omega_f} \cdot \widehat{\nabla}_{\perp} y_f = \frac{1}{P_{m,wc}} \mathbf{n}_{\Omega_f} \cdot \widehat{\nabla}_{\perp} y_{wc}, \quad y_f = y_{wc} \quad \text{at } \xi = 2, \quad (4.13c)$$

$$\mathbf{n}_{\Omega_{wc}} \cdot \widehat{\nabla}_{\perp} y_{wc} = 0 \quad \text{at } \xi = 2 + \frac{\delta_{wc}}{R_{\Omega}}, \quad (4.13d)$$

$$\frac{1}{Pe_{m,f}} \frac{\partial y_f}{\partial z} = y_f - y_f^{in}(\hat{t}), \quad \frac{\partial y_{wc}}{\partial z} = 0 \quad \text{at } z = 0, \quad (4.13e)$$

$$\frac{\partial y_f}{\partial z} = \frac{\partial y_{wc}}{\partial z} = 0 \quad \text{at } z = 1, \quad (4.13f)$$

$$\frac{1}{P_{h,f}} \mathbf{n}_{\Omega_f} \cdot \widehat{\nabla}_{\perp} \widehat{T}_f = \frac{1}{P_{h,wc}} \mathbf{n}_{\Omega_f} \cdot \widehat{\nabla}_{\perp} \widehat{T}_{wc}, \quad \widehat{T}_f = \widehat{T}_{wc} \quad \text{at } \xi = 2, \quad (4.13g)$$

$$\frac{1}{P_{h,wc}} \mathbf{n}_{\Omega_{wc}} \cdot \widehat{\nabla}_{\perp} \widehat{T}_{wc} = \frac{1}{P_{h,w}} \mathbf{n}_{\Omega_{wc}} \cdot \widehat{\nabla}_{\perp} \widehat{T}_w, \quad \widehat{T}_{wc} = \widehat{T}_w \quad \text{at } \xi = 2 + \frac{\delta_{wc}}{R_{\Omega}}, \quad (4.13h)$$

$$\mathbf{n}_{\Omega_w} \cdot \widehat{\nabla}_{\perp} \widehat{T}_w = 0 \quad \text{at } \xi = 2 + \frac{\delta_{wc} + \delta_w}{R_{\Omega}}, \quad (4.13i)$$

$$\frac{1}{Pe_{h,f}} \frac{\partial \widehat{T}_f}{\partial z} = \widehat{T}_f - \widehat{T}_f^{in}(\widehat{t}), \quad \frac{\partial \widehat{T}_{wc}}{\partial z} = \frac{\partial \widehat{T}_w}{\partial z} = 0 \text{ at } z = 0, \text{ and} \quad (4.13j)$$

$$\frac{\partial \widehat{T}_f}{\partial z} = \frac{\partial \widehat{T}_{wc}}{\partial z} = \frac{\partial \widehat{T}_w}{\partial z} = 0 \text{ at } z = 1. \quad (4.13k)$$

For periodic inlet forcing, the dimensionless inlet concentration and fluid temperature are

$$y_f^{in}(\widehat{t}) = 1 + \varepsilon_C \sin(2\pi\widehat{\omega}\widehat{t}), \quad \widehat{T}_f^{in}(\widehat{t}) = \theta^{in} \varepsilon_T \sin(2\pi\widehat{\omega}\widehat{t}),$$

where the dimensionless cycling frequency  $\widehat{\omega} = \omega\tau$ . The capacitance parameters are defined by

$$\epsilon' = \epsilon_{wc}, \quad \sigma_{wc} = \frac{\rho_{wc} C p_{wc}}{\rho_f C p_f}, \quad \sigma_w = \frac{\rho_w C p_w}{\rho_f C p_f}.$$

The various transverse Péclet numbers (related to species and heat diffusion in the transverse direction) are defined by

$$P_{m,f} = \frac{\bar{u} R_\Omega^2}{D_f L}, \quad P_{m,wc} = \frac{\bar{u} R_\Omega^2}{D_{wc} L},$$

$$P_{h,f} = \frac{\bar{u} R_\Omega^2}{\alpha_f L}, \quad P_{h,wc} = \frac{\bar{u} R_\Omega^2}{\alpha_f L} \frac{k_f}{k_{wc}}, \quad P_{h,w} = \frac{\bar{u} R_\Omega^2}{\alpha_f L} \frac{k_f}{k_w},$$

where,  $\alpha_f$  is the thermal diffusivity of the fluid defined by

$$\alpha_f = \frac{k_f}{\rho_f C p_f}.$$

The various axial Péclet numbers (related to heat and mass diffusion in the flow direction, washcoat and wall) are defined by

$$Pe_{m,f} = \frac{\bar{u} L}{D_f}, \quad Pe'_{m,wc} = \frac{\bar{u} L}{D_{wc}},$$

$$Pe_{h,f} = \frac{\bar{u} L}{\alpha_f}, \quad Pe'_{h,wc} = \frac{\bar{u} L}{\alpha_f} \frac{k_f}{k_{wc}}, \quad Pe'_{h,w} = \frac{\bar{u} L}{\alpha_f} \frac{k_f}{k_w}.$$

The subscripts  $m$  and  $h$  represent mass and heat transfer,  $f$ ,  $wc$  and  $w$  represent the flow channel, the washcoat and the substrate wall, respectively. For a first-order reaction with rate expression of the form  $R = A \exp\left(-\frac{E_a}{R_g T}\right) C$ , the Damköhler number is defined as  $Da'_0 = A\tau$ , where  $A$  is the pre-exponential factor in the Arrhenius equation. The dimensionless adiabatic temperature rise  $\beta$  is defined as

$$\beta = \frac{\Delta T_{ad} R_g}{E_a},$$

where  $E_a$  is the activation energy of the reaction,  $R_g$  is the gas constant. In the following sections, due to radial averaging, the definitions of some dimensionless groups will be different. The groups appearing in this detailed model are denoted by a prime symbol to distinguish them from those used in the simplified models.

In this work, because the dependence of transport coefficients on temperature does not qualitatively affect the comparison of reactors, we assume that they are constants for simplicity. To apply the criteria discussed in this work, one should evaluate the transport coefficients at the temperature of interest (e.g. ignition temperature) or use average values over the temperature range of interest.

We note that the model has 21 dimensionless groups consisting of cycling amplitudes and frequency, various capacitance ratios, geometric ratios, reaction parameters and Péclet numbers. Among all the dimensionless groups, the ones without reactor length  $L$ , or with only the ratio of  $L/\bar{u}$  (space time  $\tau$ ), including  $\varepsilon_C$ ,  $\varepsilon_T$ ,  $\hat{\omega}$ ,  $\epsilon'$ ,  $\sigma_{wc}$ ,  $\sigma_w$ ,  $\frac{\delta_w}{R_\Omega}$ ,  $\frac{\delta_{wc}}{R_\Omega}$ ,  $Da'_0$ ,  $\theta^{in}$ ,  $\beta$ , and the five transverse Péclet numbers remain exactly the same in both lab-scale and full-scale reactors [Remark: The parameter  $\beta$  remains the same in both scales only if the same limiting reactant concentrations are used]. However, in the five axial Péclet numbers, the reactor length  $L$  and gas velocity  $\bar{u}$  appear as a product. Thus, although the same space time is maintained in different scales, the axial Péclet numbers vary quadratically with reactor length (or scale factor). The

discrepancy of the axial Péclet numbers is one main reason for most of the scale-up issues discussed in this work. Although it is not possible to match the axial Péclet numbers in different scales, the impact of them (axial dispersion/conduction) can be neglected when they are very large and the adiabatic temperature rise is small. In that case, all the  $\frac{1}{Pe} \frac{\partial^2}{\partial z^2}$  terms will be negligible, resulting in a two-dimensional (parabolic) model (with plug flow in the axial direction but with radial heat and mass diffusion included). In this case, similarity can be found in reactors of different scales. However, this is rarely satisfied since the axial Péclet numbers in the lab-scale reactors are usually small (typically by a factor 10 to 100 compared to the full-scale systems).

### 4.3 Simplified Models

In catalytic after-treatment reactors, the transverse Péclet numbers are usually very small, indicating that the concentration and temperature variations across the channel are small. Thus, it is reasonable to use radially lumped models to analyze scale-up issues. Although this assumption of small radial gradients and radial averaging may introduce small error, it may be justified for two reasons: (i) as noted above, it is the *axial* Péclet numbers that do not match at different scales (ii) models of different scales will be influenced in the same way since all the transverse Péclet numbers are exactly matched.

#### 4.3.1 One-dimensional Two-phase Monolith Model

When radial gradients are small, a one-dimensional two-phase model is commonly used. Radially averaging the two-dimensional model and using mass and heat transfer coefficients (Balakotaiah, 2008), the model becomes one-dimensional. Thus, the

species balance in the fluid phase is simplified to

$$\frac{\partial y_f}{\partial \widehat{t}} + \frac{\partial y_f}{\partial z} = \frac{1}{Pe_{m,f}} \frac{\partial^2 y_f}{\partial z^2} - \frac{1}{P_m} (y_f - y_{wc}), \quad (4.14)$$

while the species balance in the washcoat is given by

$$\epsilon \frac{\partial y_{wc}}{\partial \widehat{t}} = \frac{1}{Pe_{m,wc}} \frac{\partial^2 y_{wc}}{\partial z^2} + \frac{1}{P_m} (y_f - y_{wc}) - Da_0 y_{wc} \exp\left(\frac{-1/\beta}{\widehat{T}_s + \theta^{in}}\right). \quad (4.15)$$

For simplicity, we keep the same notation for the state variables. However, unlike in the two-dimensional case where they are functions of the radial position, in the one-dimensional two-phase model they are considered radially averaged values. For example,  $y_f$  and  $y_{wc}$ , represent the cup-mixing (dimensionless) concentration in the fluid phase and the volume averaged (dimensionless) concentration in the washcoat, respectively. Because of the radial averaging, some geometric factors appear in the lumped parameters:

$$\epsilon = \epsilon' \frac{\delta_{wc}}{R_\Omega}, \quad Da_0 = Da'_0 \frac{\delta_{wc}}{R_\Omega}, \quad Pe_{m,wc} = Pe'_{m,wc} \frac{R_\Omega}{\delta_{wc}}.$$

Further,  $P_{m,f}$  and  $P_{m,wc}$  are lumped into an overall transverse mass Péclet number  $P_m$  defined by

$$P_m = P_{m,f} \frac{4}{Sh_e} + P_{m,wc} \frac{\delta_{wc}}{R_\Omega} \frac{1}{Sh_i},$$

where  $Sh_e$  and  $Sh_i$  are external and internal Sherwood numbers, respectively. The Sherwood numbers are defined as (Joshi et al., 2010)

$$Sh_e = \frac{4k_{m,e}R_\Omega}{D_f}, \quad Sh_i = \frac{k_{m,i}R_\Omega}{D_{wc}},$$

where  $k_{m,e}$  and  $k_{m,i}$  are external and internal mass transfer coefficients.

The energy balance in the fluid phase is

$$\frac{\partial \widehat{T}_f}{\partial t} + \frac{\partial \widehat{T}_f}{\partial z} = \frac{1}{Pe_{h,f}} \frac{\partial^2 \widehat{T}_f}{\partial z^2} - \frac{1}{P_h} \left( \widehat{T}_f - \widehat{T}_s \right). \quad (4.16)$$

Since the thermal conductivities of the washcoat and the substrate wall are both large and the thicknesses are small, in the energy balance we assume the temperature is radially uniform in the whole solid phase including both the washcoat and the substrate wall. The parameters used for the solid phase can be defined as an effective or averaged value for the two layers,

$$\begin{aligned} \delta_s &= \delta_w + \delta_{wc}, \quad \delta_s k_s = \delta_w k_w + \delta_{wc} k_{wc}, \\ \rho_s C p_s \delta_s &= \rho_{wc} C p_{wc} \delta_{wc} + \rho_w C p_w \delta_w, \\ P_{h,s} &= \frac{\bar{u} R_\Omega^2 k_f}{\alpha_f L k_s} = \frac{\delta_{wc} + \delta_w}{\frac{\delta_{wc}}{P_{h,wc}} + \frac{\delta_w}{P_{h,w}}}, \\ Pe_{h,s} &= \frac{\bar{u} L k_f R_\Omega}{\alpha_f k_s \delta_s} = \frac{1}{\frac{1}{Pe'_{h,wc}} \frac{\delta_{wc}}{R_\Omega} + \frac{1}{Pe'_{h,w}} \frac{\delta_w}{R_\Omega}}, \end{aligned}$$

where the subscript  $s$  stands for the solid phase including both the washcoat and the substrate. The energy balance in the solid phase can be expressed as

$$\sigma_s \frac{\partial \widehat{T}_s}{\partial t} = \frac{1}{P_h} \left( \widehat{T}_f - \widehat{T}_s \right) + \frac{1}{Pe_{h,s}} \frac{\partial^2 \widehat{T}_s}{\partial z^2} + Da_0 y_{wc} \exp \left( \frac{-1/\beta}{\widehat{T}_s + \theta^{in}} \right). \quad (4.17)$$

The heat capacity ratio  $\sigma_s$  is defined as

$$\sigma_s = \frac{\rho_s C p_s \delta_s}{\rho_f C p_f R_\Omega}.$$

$P_{h,f}$  and  $P_{h,s}$  are lumped into an overall transverse heat Péclet number  $P_h$  as

$$P_h = P_{h,f} \frac{4}{Nu_e} + P_{h,s} \frac{\delta_s}{R_\Omega} \frac{1}{Nu_i},$$

where  $Nu_e$  and  $Nu_i$  are external and internal Nusselt numbers, respectively. The Nusselt numbers are defined as

$$Nu_e = \frac{4h_e R_\Omega}{k_f}, Nu_i = \frac{h_i R_\Omega}{k_s},$$

where  $h_e$  and  $h_i$  are external and internal heat transfer coefficients.

The initial and boundary conditions for this one-dimensional two-phase model are given by

$$y_f = y_f^0(z), y_{wc} = y_{wc}^0(z) \text{ at } \hat{t} = 0, \quad (4.18a)$$

$$\hat{T}_f = \hat{T}_f^0(z), \hat{T}_s = \hat{T}_s^0(z) \text{ at } \hat{t} = 0, \quad (4.18b)$$

$$\frac{1}{Pe_{m,f}} \frac{\partial y_f}{\partial z} = y_f - y_f^{in}(\hat{t}), \frac{\partial y_{wc}}{\partial z} = 0 \text{ at } z = 0, \quad (4.18c)$$

$$\frac{\partial y_f}{\partial z} = \frac{\partial y_{wc}}{\partial z} = 0 \text{ at } z = 1, \quad (4.18d)$$

$$\frac{1}{Pe_{h,f}} \frac{\partial \hat{T}_f}{\partial z} = \hat{T}_f - \hat{T}_f^{in}(\hat{t}), \frac{\partial \hat{T}_s}{\partial z} = 0 \text{ at } z = 0, \text{ and} \quad (4.18e)$$

$$\frac{\partial \hat{T}_f}{\partial z} = \frac{\partial \hat{T}_s}{\partial z} = 0 \text{ at } z = 1. \quad (4.18f)$$

Since the thermal conductivity in the solid phase is much larger than that in the fluid phase,  $P_{h,s} \ll P_{h,f}$ , thus

$$P_h \approx P_{h,f} \frac{4}{Nu_e} = \frac{\bar{u} R_\Omega^2}{\alpha_f L} \frac{4}{Nu_e},$$

and the term containing the internal Nusselt number ( $Nu_i$ ) can usually be neglected. Gundlapally and Balakotaiah (2011) showed that  $Nu_e$  and  $Sh_e$  are functions of space time, radial geometric parameters and diffusivities of the species, which are either independent of  $L$  or dependent on the ratio  $L/\bar{u}$ . Kumar et al. (2012, 2014) provided a correlation for  $Sh_i$ , which involves only kinetic parameters and local properties.

Thus, the transverse heat and mass Péclet numbers ( $P_h$  and  $P_m$ ) are matched exactly in reactors with different scales provided that the same space time is maintained. This confirms our conclusion in 4.2 that the radial mass and heat transfer is matched in lab-scale and full-scale reactors. Although this one-dimensional two-phase model has fewer dimensionless groups due to radial lumping, all information from 4.2 is retained. The dimensionless groups from the two-dimensional model are either kept the same (e.g.,  $Pe_{m,f}$ ) or lumped with similar group to form a combined group (e.g.,  $P_m$ ). [Remark: Radial lumping has reduced the 21 dimensionless groups (5 axial Péclet numbers) of the two-dimensional model into 14 dimensionless groups (4 axial Péclet numbers) of the one-dimensional two-phase model.]

### 4.3.2 Pseudo-homogeneous Model

If the lumped transverse Péclet numbers  $P_m$  and  $P_h$  are very small, one can combine separate phase balances and form a pseudo-homogeneous model by utilizing effective Péclet number  $Pe_{eff}$  defined as (Gundlapally and Balakotaiah, 2013)

$$\frac{1}{Pe_{eff}} = \frac{1}{Pe} + P, \quad (4.19)$$

which combines the effects of axial dispersion and interphase (radial) gradient. Here, for simplicity, we examine this homogeneous limit, i.e.  $P_m = P_h = 0$ . As mentioned in 4.3, since the transverse Péclet numbers are exactly matched, and they are small, neglecting their effects will not qualitatively effect our analysis. The impact of this simplification is further discussed in 5.3.

When combining separate phase balances, the axial Péclet numbers for the pseudo-homogeneous model,  $Pe_m$  and  $Pe_h$ , are defined as

$$Pe_m = \frac{1}{\frac{1}{Pe_{m,f}} + \frac{1}{Pe_{m,wc}}} = \frac{\bar{u}L}{D_f} \frac{1}{1 + \frac{D_{wc}}{D_f} \frac{\delta_{wc}}{R_\Omega}} \approx Pe_{m,f} \text{ and}$$

$$Pe_h = \frac{1}{\frac{1}{Pe_{h,f}} + \frac{1}{Pe_{h,s}}} = \frac{\bar{u}L k_f R_\Omega}{\alpha_f k_s \delta_s} \frac{1}{\frac{k_f R_\Omega}{k_s \delta_s} + 1} \approx Pe_{h,s}.$$

Thus, when the axial Péclet number in one phase is significantly larger than the one in the other phase, the smaller one will dominate the behavior of the pseudo-homogeneous model. In the case of mass transfer, since the molecular diffusivity in the washcoat ( $D_{wc}$ ) can be two to three orders of magnitude smaller than the molecular diffusivity in the fluid phase,  $Pe_{m,f}$  is usually much smaller than  $Pe_{m,s}$ . Thus, it is reasonable to assume  $Pe_m \approx Pe_{m,f}$ . Similarly in the case of axial heat diffusion,  $Pe_{h,f}$  is usually much larger than  $Pe_{h,s}$  (as the solid thermal conductivity is about two orders of magnitude larger than that of the fluid). Assuming  $Pe_h \approx Pe_{h,s}$  will only lead to small error.

Here, we examine the ratio  $Pe_m/Pe_h$ ,

$$\frac{Pe_m}{Pe_h} \approx \frac{Pe_{m,f}}{Pe_{h,s}} = \frac{k_s}{k_f} \frac{\delta_s}{R_\Omega} Le_f,$$

where

$$Le_f = \frac{\alpha_f}{D_f}$$

is the Lewis number depending only on the physical properties of the gas and diffusivity of the limiting reactant species. Further,  $\delta_s/R_\Omega$  is a constant depending on the monolith channel structure, and  $k_s/k_f$  depends on the material of the monolith and thermal conductivity of the fluid. Thus, under the assumptions of this work, the  $Pe_m/Pe_h$  ratio remains the same regardless of the reactor length. For ceramic monolith, this ratio is about 10 while for metallic monolith the ratio can be 100 or up to several hundreds.

With the dimensional analysis and simplifications, we arrive at a monolith model that is simple yet sufficient to explore the differences in reactors of different scales. For convenience and symmetry of the equations, we use the conversion  $\chi = 1 - y$

instead of the dimensionless concentration  $y$ , in the species balance,

$$(1 + \epsilon) \frac{\partial \chi}{\partial \hat{t}} = \frac{1}{Pe_m} \frac{\partial^2 \chi}{\partial z^2} - \frac{\partial \chi}{\partial z} + Da_0 (1 - \chi) \exp\left(\frac{-1/\beta}{\hat{T} + \theta^{in}}\right). \quad (4.20)$$

The energy balance is

$$(1 + \sigma_s) \frac{\partial \hat{T}}{\partial \hat{t}} = \frac{1}{Pe_h} \frac{\partial^2 \hat{T}}{\partial z^2} - \frac{\partial \hat{T}}{\partial z} + Da_0 (1 - \chi) \exp\left(\frac{-1/\beta}{\hat{T} + \theta^{in}}\right). \quad (4.21)$$

The boundary conditions are

$$\frac{1}{Pe_m} \frac{\partial \chi}{\partial z} - \chi = y_f^{in}(\hat{t}) - 1 = \varepsilon_C \sin(2\pi\hat{\omega}\hat{t}), \text{ at } z = 0, \quad (4.22a)$$

$$\frac{1}{Pe_h} \frac{\partial \hat{T}}{\partial z} - \hat{T} = -\hat{T}_f^{in}(\hat{t}) = -\theta^{in} \varepsilon_T \sin(2\pi\hat{\omega}\hat{t}), \text{ at } z = 0, \text{ and} \quad (4.22b)$$

$$\frac{\partial \chi}{\partial z} = \frac{\partial \hat{T}}{\partial z} = 0 \text{ at } z = 1. \quad (4.22c)$$

[Remark: In simplifying the one-dimensional two-phase model further to this pseudo-homogeneous model, we have reduced the number of dimensionless groups to 10 and the axial Péclet numbers to 2. The steady-state version of this model is characterized by five groups, i.e.  $Da_0$ ,  $\beta$ ,  $\theta^{in}$ ,  $Pe_m$  and  $Pe_h$ .] This model has three limiting cases of significance. When both  $Pe_m \rightarrow 0$  and  $Pe_h \rightarrow 0$ , the model approaches a continuous-flow stirred tank reactor (CSTR) asymptote; when  $Pe_m \rightarrow \infty$  and  $Pe_h \rightarrow \infty$ , the model approaches a plug flow reactor (PFR) asymptote; when  $Pe_m \rightarrow \infty$  and  $Pe_h \rightarrow 0$ , the model becomes a lumped thermal reactor model (LTR). Because  $Pe_m$  is usually larger than  $Pe_h$ , the asymptote where  $Pe_m \rightarrow 0$  and  $Pe_h \rightarrow \infty$  is not important from a practical point of view.

Since the dimensionless time  $\hat{t}$  and frequency  $\hat{\omega}$  contain only the ratio of  $L/\bar{u}$ , which is matched in different scales, the transient performances of lab- and full-scale reactors will be similar provided that their steady-state performances (e.g. light-off

curves, hysteresis behaviors) are similar. Thus, in the following sections, we consider mainly the steady-state versions of the simplified models to study the scale-up issues. In the steady-state models, all  $\hat{t}$  containing terms are neglected and the equations become nonlinear ordinary differential equations (ODEs) in the axial coordinate.

# Chapter 5

## Impact of Heat and Mass Dispersion and Thermal Effects on the Scale-up of Monolith Reactors

### 5.1 Impact of Mass Dispersion

As discussed above, the mass Péclet number  $Pe_m$  is usually much larger than heat Péclet number  $Pe_h$ , the ratio can vary from 10 (for ceramic monolith) to 100 (for metallic monolith). Thus,  $Pe_m$  usually has less impact on the reactor behavior than  $Pe_h$  in most non-isothermal operations and one can often neglect the axial diffusion term in the species balance. However, in isothermal operations, different  $Pe_m$  (different reactor length scales) can also lead to significant quantitative and sometimes qualitative differences.

#### 5.1.1 Linear Kinetics

In case of an isothermal reactor, where  $\Delta T_{ad} = 0$ ,  $T = T^{in}$ , for a first-order reaction the steady-state pseudo-homogeneous model becomes

$$\frac{1}{Pe_m} \frac{d^2\chi}{dz^2} - \frac{d\chi}{dz} + Da_0(1 - \chi) \exp\left(-\frac{E_a}{RT^{in}}\right) = 0 \text{ and} \quad (5.1)$$

$$\frac{1}{Pe_m} \frac{d\chi}{dz} \Big|_{z=0} - \chi(z=0) = 0, \quad \frac{d\chi}{dz} \Big|_{z=1} = 0. \quad (5.2)$$

The solution of the above isothermal axial dispersion model can be found in chemical engineering textbooks (Fogler, 2005; Levenspiel, 1998). The exit conversion is

$$\chi^{exit} = 1 - \frac{4q \exp(Pe_m/2)}{(1+q)^2 \exp(qPe_m/2) - (1-q)^2 \exp(-qPe_m/2)}, \quad (5.3)$$

where

$$q = \sqrt{1 + \frac{4Da_0}{Pe_m} \exp\left(-\frac{E_a}{RT^{in}}\right)}.$$

The two asymptotic cases where  $Pe_m \rightarrow \infty$  (PFR) and  $Pe_m \rightarrow 0$  (CSTR) can also be solved as

$$\chi_{PFR}^{exit} = 1 - \exp\left(-Da_0 \exp\left(-\frac{E_a}{RT^{in}}\right)\right) \quad \text{and} \quad (5.4)$$

$$\chi_{CSTR}^{exit} = 1 - \frac{1}{1 + Da_0 \exp\left(-\frac{E_a}{RT^{in}}\right)}. \quad (5.5)$$

Shown in Fig. 5.1 are steady-state conversions of isothermal reactors with different  $Pe_m$ , where the kinetic parameters are chosen to be typical values of after-treatment catalysts ( $E_a = 100 \text{ kJ/mol}$ ,  $Da_0 = 10^{10}$ ). When  $Pe_m$  is smaller than 10, mass dispersion can introduce significant quantitative errors especially at high conversions ( $\chi^{exit} > 0.8$ ), which is the range of interest. In that case, direct scale-up according to lab-scale performance will result in an overdesign of the catalyst loading for full-scale reactors.

### 5.1.2 Nonlinear Kinetics

When the kinetics are nonlinear, mass dispersion can create multiple solutions in the steady-state conversions. Hence, the difference between reactors with different  $Pe_m$  can be qualitative. Langmuir-Hinshelwood mechanism and Voltz kinetics are widely accepted as global kinetic models for  $CO$  oxidation on Pt and other oxidation reactions in after-treatment catalysts (Voltz et al., 1973; Salomons et al., 2007; Olsson et al., 2005). Here we take Langmuir-Hinshelwood kinetics for  $CO$  oxidation as an

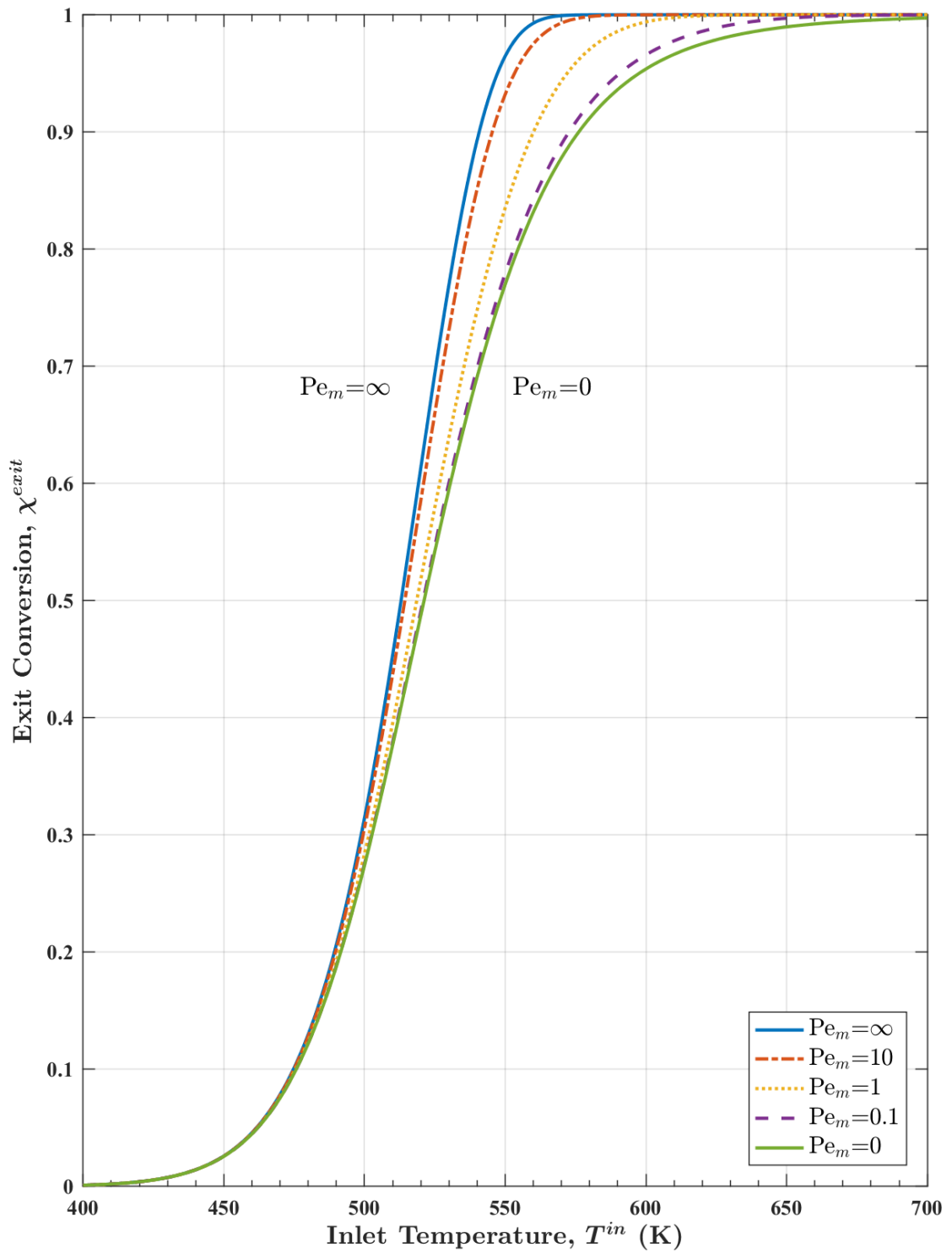


Figure 5.1: Plot of steady-state exit conversion versus inlet temperature in isothermal reactors with first-order kinetics and different axial mass Péclet numbers ( $Pe_m$ ). ( $E_a = 100$  kJ/mol,  $Da_0 = 10^{10}$ )

example, and the rate expression is given by

$$R = \frac{A \exp\left(-\frac{E_a}{RT}\right) C_{O_2} C_{CO}}{(1 + K_{ads} C_{CO})^2},$$

where  $K_{ads}$  is the adsorption equilibrium constant. When the concentration of  $CO$  is high, the reaction is inhibited by  $CO$  and close to negative first-order with respect to  $CO$ .

We assume that  $O_2$  is in large excess so that  $C_{O_2}$  can be treated as a constant and can be lumped into the rate constant. The dimensionless adsorption equilibrium constant  $\kappa$  is defined as

$$\kappa = K_{ads} C_{total},$$

where  $C_{total}$  is total fluid concentration. Then, the Damköhler number can be defined as

$$Da_0^{LH} = \frac{A\tau C_{O_2}}{(1 + \kappa X_{CO}^{in})^2} \frac{\delta_{wc}}{R\Omega}.$$

The model equations in terms of  $CO$  conversion are

$$\frac{1}{Pe_m} \frac{d^2\chi}{dz^2} - \frac{d\chi}{dz} + Da_0^{LH} \exp\left(-\frac{E_a}{RT^{in}}\right) \frac{(1 + \kappa X_{CO}^{in})^2 (1 - \chi)}{[1 + \kappa X_{CO}^{in} (1 - \chi)]^2} = 0 \quad \text{and} \quad (5.6)$$

$$\frac{1}{Pe_m} \frac{d\chi}{dz} \Big|_{z=0} = \chi(z=0), \quad \frac{d\chi}{dz} \Big|_{z=1} = 0. \quad (5.7)$$

For simplicity,  $\kappa$  is assumed constant versus temperature. Using typical kinetic parameters for CO oxidation ( $E_a = 100$  kJ/mol,  $Da_0^{LH} = 10^{10}$ ,  $\kappa = 2000$ ,  $X_{CO}^{in} = 0.02$ ), the bifurcation diagrams are calculated for different  $Pe_m$  as shown in Fig. 5.2. Reactors with small  $Pe_m$  have a lower ignition temperature, multiple steady-states and hence hysteresis behavior, while the full-scale reactor (high  $Pe_m$ , close to PFR) does not exhibit hysteresis.

Hysteresis region caused by nonlinear kinetics is usually narrow since the nonlin-

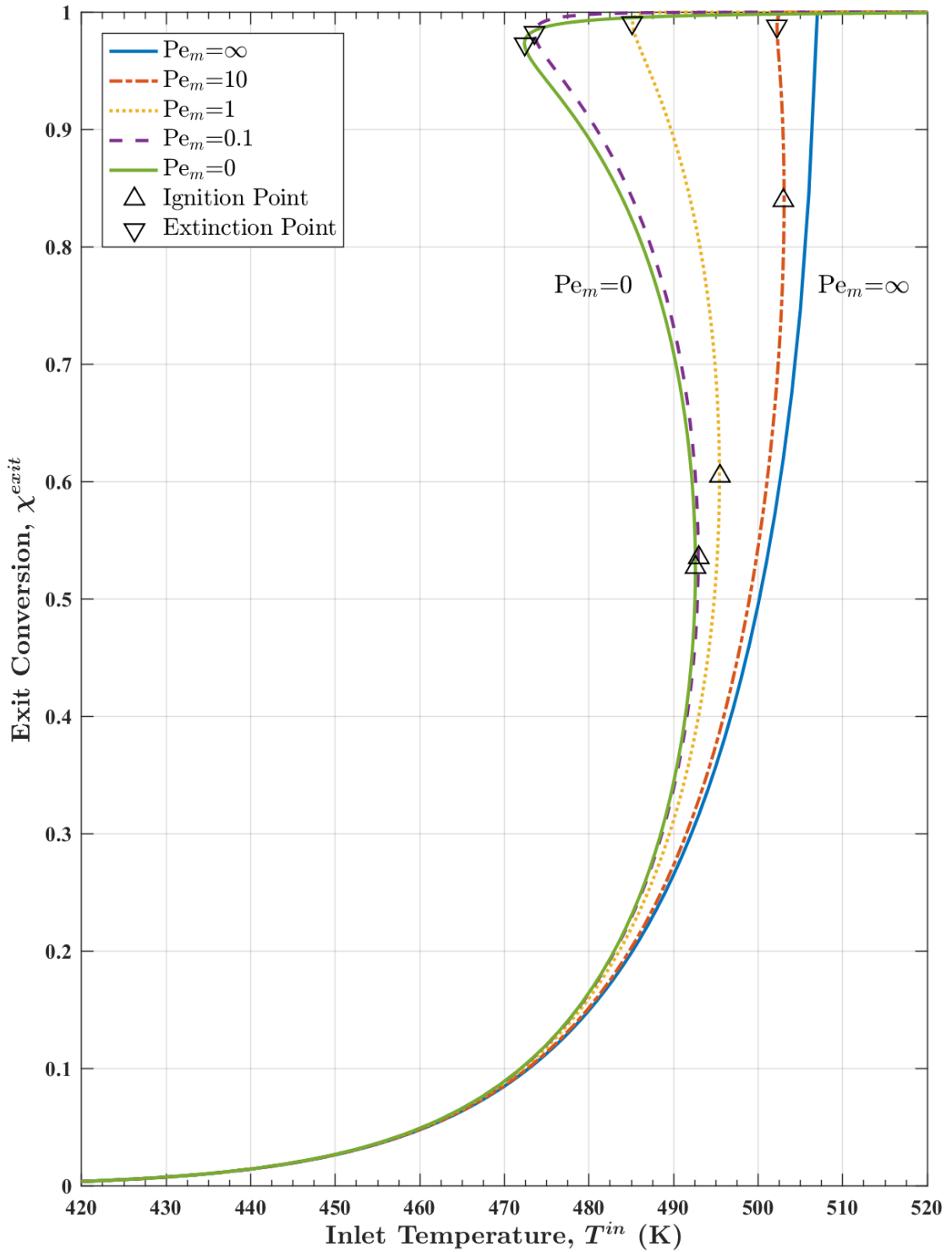


Figure 5.2: Bifurcation diagrams of steady-state exit conversion versus inlet temperature for isothermal reactors with Langmuir-Hinshelwood kinetics and different axial mass Péclet numbers ( $Pe_m$ ). ( $E_a = 100$  kJ/mol,  $Da_0^{LH} = 10^{10}$ ,  $\kappa = 2000$ ,  $X_{CO}^{in} = 0.02$ )

earity is polynomial. It appears when  $Pe_m$  is small and  $\kappa X_{CO}^{in}$  is large. Shown in Fig. 5.3, are hysteresis loci for isothermal reactors with different  $\kappa$  projected on the  $(X^{in}, Pe_m)$  plane. For more "sticky" (or strongly absorbed) molecules (e.g. propylene),  $\kappa$  becomes larger and it is more difficult to eliminate multiplicity. When  $Pe_m$  is large ( $>100$ ), the inlet concentration required for multiplicity exceeds practical range and mass dispersion causes only quantitative errors. [Remark: Hysteresis locus is the set of parameter values at which ignition and extinction points appear or disappear in the bifurcation diagram of a state variable (e.g. exit conversion) versus a bifurcation parameter (e.g. inlet temperature).]

### 5.1.3 Cycling Performance

As stated in 4.3.2, if the steady-state performances are similar in reactors of different scales, the transient performances will also be similar. Here, through simulating the cycling operations of a isothermal reactor, we illustrate that when steady-state performances of lab- and full-scale reactors are different, their transient performances will also differ. For a first-order reaction, the transient model is linear. The cycle averaged conversion will be almost the same as the steady-state conversion (Fig. 5.1) unless the cycling is very fast (cycle time is much smaller than the residence time of the reactor). For nonlinear kinetics shown, the cycling performance is analyzed by solving the transient model, (for the transient model  $Da_0^{LH}$  is defined with respect to the average inlet mole fraction  $\bar{X}_{CO}^{in}$ )

$$(1 + \epsilon) \frac{\partial \chi}{\partial t} = \frac{1}{Pe_m} \frac{\partial^2 \chi}{\partial z^2} - \frac{\partial \chi}{\partial z} + Da_0^{LH} \exp\left(-\frac{E_a}{RT^{in}}\right) \frac{(1 + \kappa \bar{X}_{CO}^{in})^2 (1 - \chi)}{[1 + \kappa \bar{X}_{CO}^{in} (1 - \chi)]^2}, \quad (5.8)$$

$$\frac{1}{Pe_m} \frac{\partial \chi}{\partial z} - \chi = \epsilon_C \sin(2\pi \hat{\omega} \hat{t}) \quad \text{at } z = 0, \quad \text{and} \quad (5.9a)$$

$$\frac{\partial \chi}{\partial z} = 0 \quad \text{at } z = 1. \quad (5.9b)$$

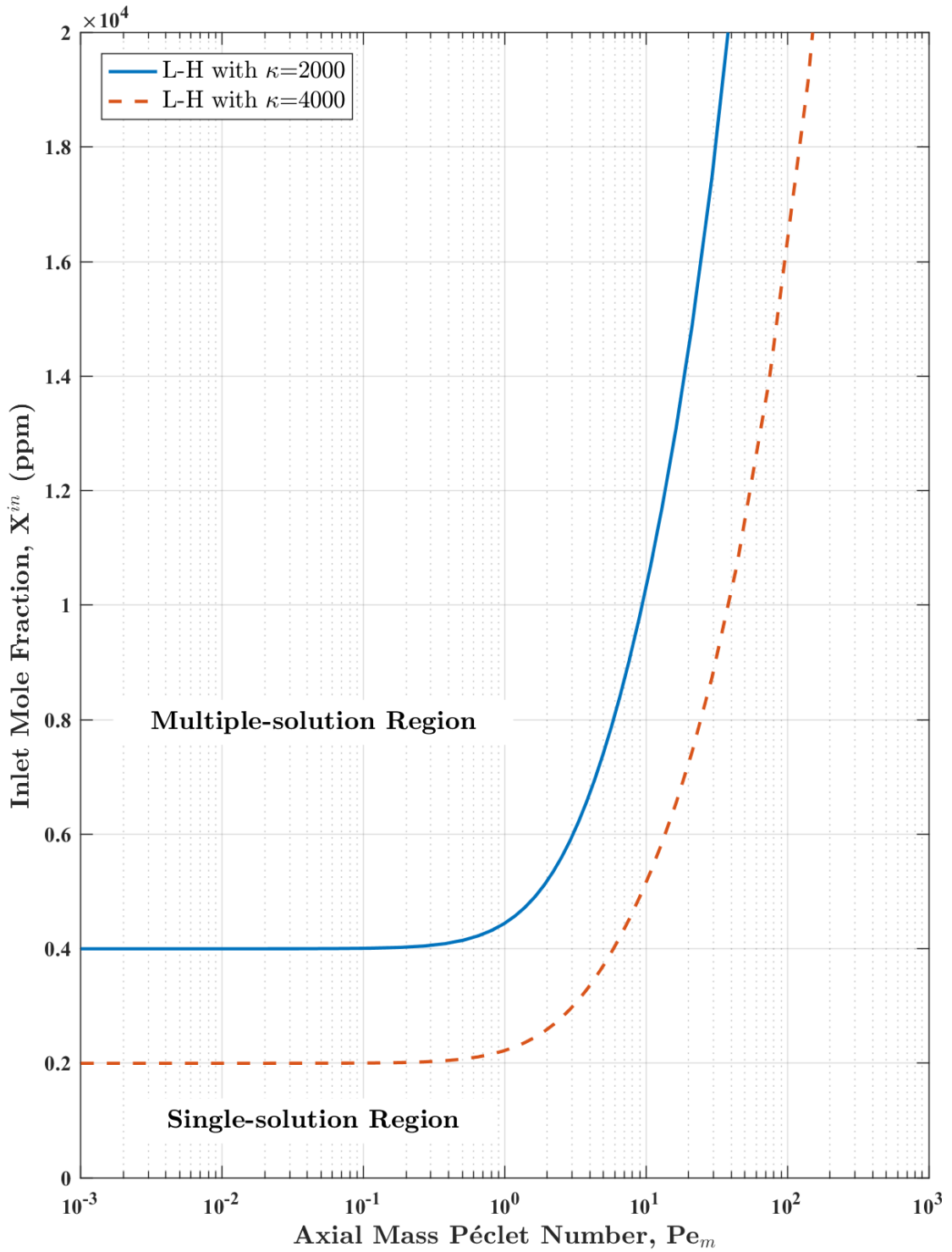


Figure 5.3: Hysteresis loci of isothermal reactors with Langmuir-Hinshelwood kinetics and different adsorption equilibrium constants ( $\kappa$ ) in the  $(X^{in}, Pe_m)$  plane. ( $E_a = 100 \text{ kJ/mol}$ ,  $Da_0^{LH} = 10^{10}$ )

For the simulations, we take  $\epsilon = 0.1$ ,  $E_a = 100$  kJ/mol and  $Da_0 = 10^{10}$ . As shown in 5.1.2, this model can exhibit ignition/extinction behavior with fixed  $X_{CO}^{in}$  and varying  $T^{in}$ . Similarly, the model can also show ignition/extinction when  $T^{in}$  is fixed and  $X_{CO}^{in}$  is varying, which will significantly affect the cycling performances of the reactor. For example, at  $T^{in} = 470$  K, bifurcation diagrams of  $\chi^{exit}$  versus  $X_{CO}^{in}$  are calculated for different  $Pe_m$  as shown in Fig. 5.4. To better illustrate cycling performances, in the transient simulations  $\varepsilon_C$  is chosen to be 100% so that all possible ignition/extinction behaviors are included in the calculation.

The dimensionless frequency  $\hat{\omega}$  can be interpreted as how many times the inlet concentration will cycle during the space time. For a typical after-treatment reactor,  $\hat{\omega}$  is usually smaller than 0.1 (for a 100 ms space time, this results in 1 Hz cycling). We conduct transient simulations for  $\hat{\omega} = 0.01$  and 0.1 till the model reaches periodic steady-state, and plot the cycle averaged exit conversion versus inlet temperature in Fig. 5.5. Comparing to the steady-state light-off curve ( $\hat{\omega} = 0$ ), the impact of mass dispersion (the difference between lab- and full-scale reactor) is more significant in the cycling cases. Different cycling performances between lab- and full-scale reactor is also observed experimentally by Prikhodko et al. (2009), who referred to this as axial length effects when they compared the performances of a 2.54- cm-long (or lab-scale) LNT catalyst and a 7.64- cm-long (or full-scale) one.

#### 5.1.4 Estimation of Kinetic Parameters from Light-off Curves

In after-treatment reactors,  $Pe_m$  is usually of order  $10^3$  in full-scale reactors and is usually larger than 10 in lab-scale reactors (assuming a scaling factor of 10). Thus, in most cases mass dispersion has minor impact and the reactor behaves like a PFR. However, when the lab-scale reactor is too short (leading to small  $Pe_m$ ), axial mass dispersion is noticeably influencing the reactor behaviors. In this case, using a reactor model without axial dispersion (e.g. PFR) to estimate kinetic parameters from lab

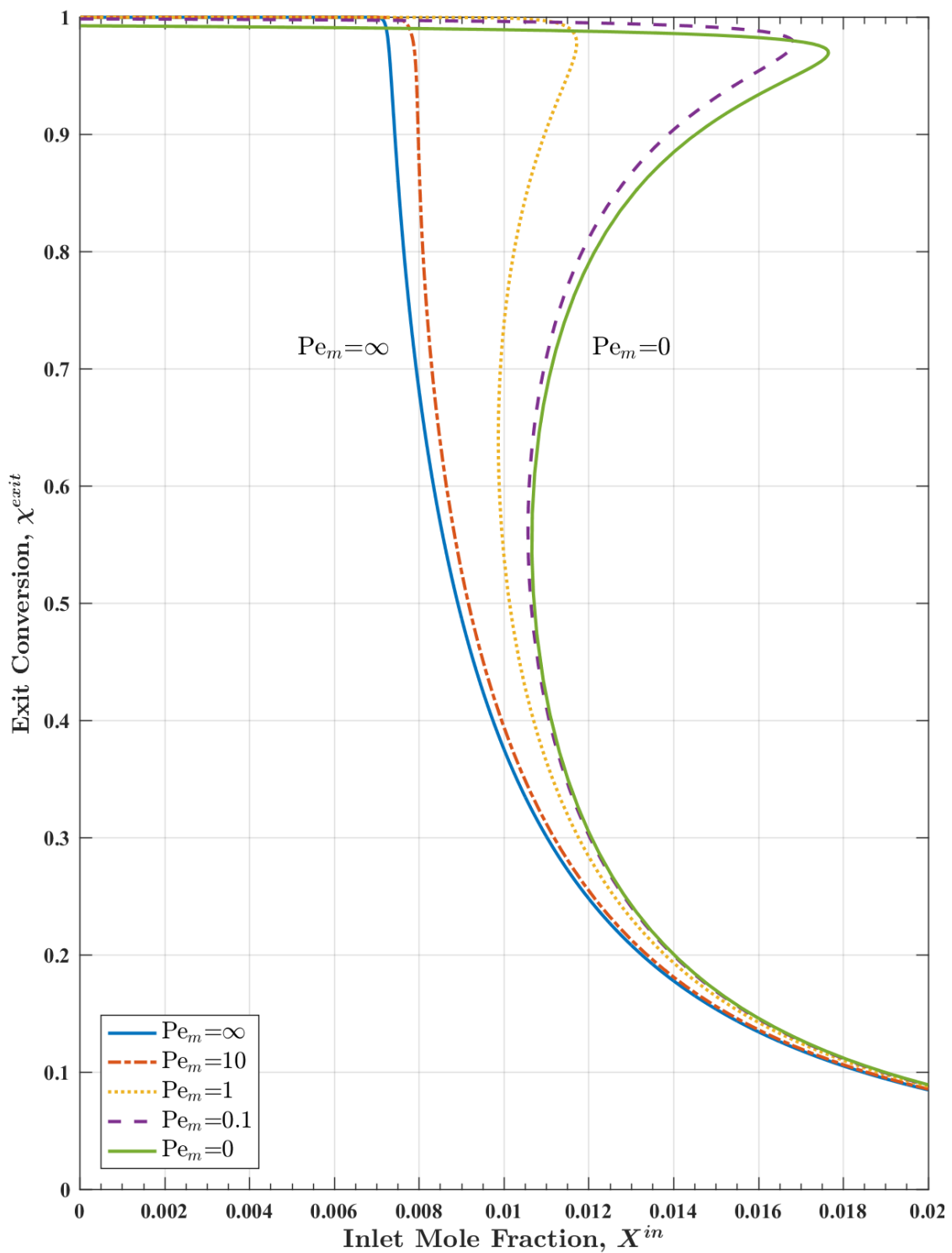


Figure 5.4: Bifurcation diagrams of steady-state exit conversion versus inlet mole fraction for isothermal reactors with Langmuir-Hinshelwood kinetics and different axial mass Péclet numbers ( $Pe_m$ ). ( $E_a = 100$  kJ/mol,  $Da_0^{LH} = 10^{10}$ ,  $\kappa = 2000$ ,  $T^{in} = 470$  K)

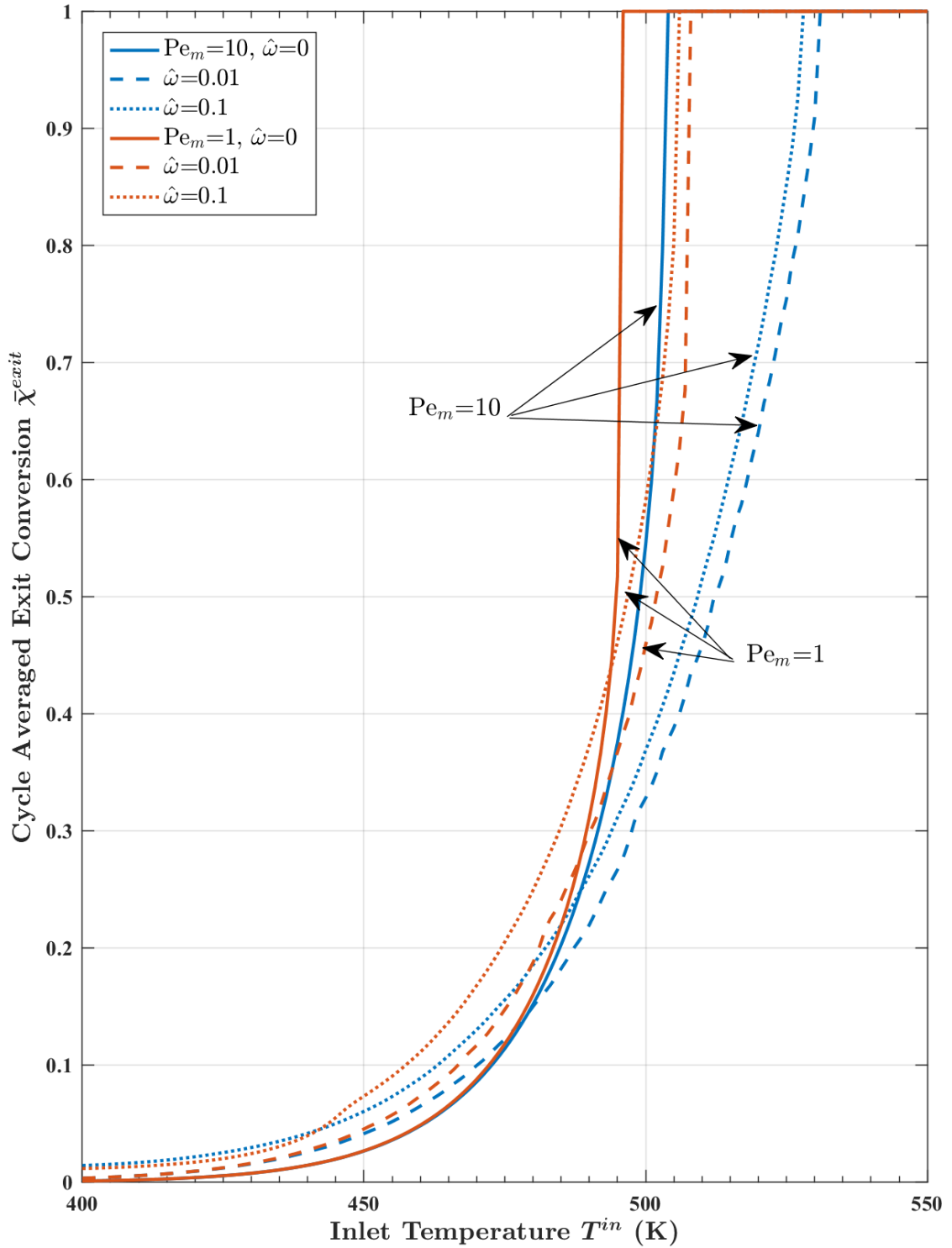


Figure 5.5: Light-off curves of cycle averaged exit conversion versus inlet temperature for isothermal reactors with Langmuir-Hinshelwood kinetics. ( $E_a = 100$  kJ/mol,  $Da_0^{LH} = 10^{10}$ ,  $\kappa = 2000$ ,  $\epsilon = 0.1$ ,  $\bar{X}_{CO}^{in} = 0.02$ ,  $\epsilon_C = 1$ )

data, can result in significant quantitative errors. For linear kinetics, if we use a PFR model to fit data generated from a reactor with  $Pe_m = 10$  by equalizing the values and the slopes of steady-state conversions at the inflection temperature (where the exit conversion is  $1 - 1/e \approx 0.632$ ), the estimated activation energy  $\widetilde{E}_a \approx 0.923E_a$ , resulting in  $\sim 8\%$  error. Shown in Fig. 5.6a is how this estimation error changes with  $Pe_m$  of lab-scale reactors. In Fig. 5.6b, we can see that although the fitting error is small, the estimated activation energy  $\widetilde{E}_a$  can have significant error (for the case in the figure  $\sim 25\%$ ).

When estimating kinetic parameters for nonlinear kinetics, the experiments should be designed such that both the rate constants and the adsorption constants can be estimated. The rate constants (or pre-exponential factor  $A$  and activation energy  $E_a$ ) can be obtained by using low inlet concentrations of the limiting reactant such that  $K_{ads}C^{in} \ll 1$ . In this way, the nonlinear effects are negligible and same method used in linear kinetics can be applied. After estimating  $A$  and  $E_a$ , the adsorption constant  $K_{ads}$  can be estimated by using higher inlet concentration of the limiting reactant. In such cases, the nonlinear effects are more pronounced and the reactor may exhibit hysteresis. Then, both light-off (ignition) and light-out (extinction) curves should be used in the estimation. The necessity of both curves has also been emphasized in the recent work by Etheridge and Watling (2015). This process has two further complications: (i) Without estimating  $K_{ads}$ , one cannot select  $C^{in}$  to guarantee  $K_{ads}C^{in} \ll 1$  and estimate  $A$  and  $E_a$  assuming a first-order reaction. Without good estimations of  $A$  and  $E_a$ , accurate  $K_{ads}$  estimation cannot be obtained. Thus, the estimations of the rate constants and the adsorption constants should be done iteratively. (ii) For the negative-order effects to be significant, high inlet concentrations are used. This leads to higher adiabatic temperature rise and the isothermal assumption may not be valid. In this case, the hysteresis is caused by the combined effect of nonlinear kinetics and non-isothermal effects which is discussed in 5.2.2.

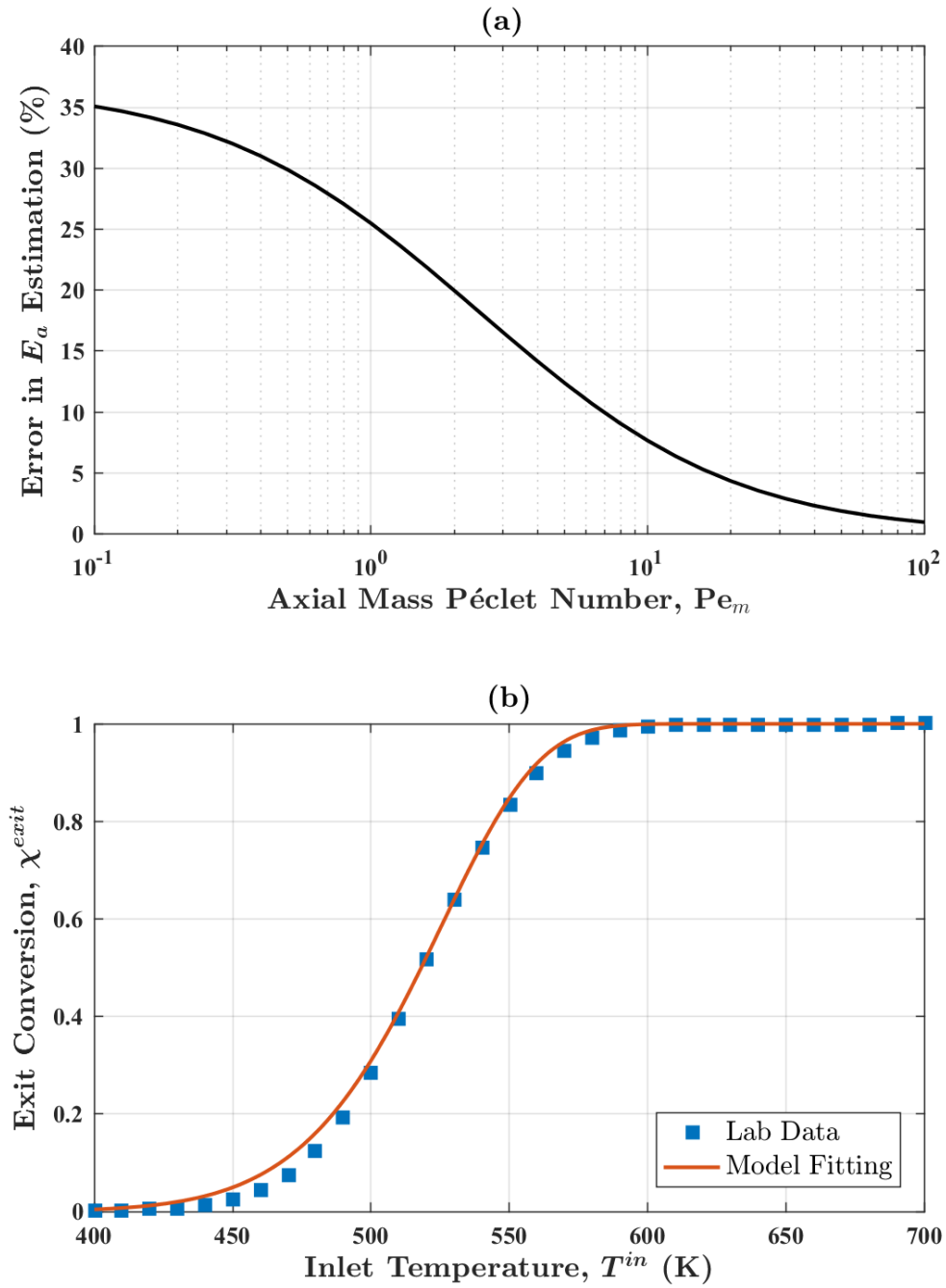


Figure 5.6: (a) Percentage error in the estimated activation energy by assuming a PFR model and fitting data from reactors with first-order kinetics and different  $Pe_m$ . (b) PFR model fitting data generated from a reactor with  $Pe_m = 1$ . ( $E_a = 100$  kJ/mol,  $Da_0 = 10^{10}$ )

## 5.2 Impact of Heat Conduction and Adiabatic Temperature Rise

Unlike lab-scale reactors, which are placed in a furnace whose temperature is controlled, full-scale reactors are usually operated almost adiabatically. When the adiabatic temperature rise  $\Delta T_{ad}$  (or  $\beta$ ) is not negligible, there will be significant thermal gradients and hence an axial temperature profile in the reactor. For small  $\Delta T_{ad}$ , the shape of the steady-state temperature profile is determined by heat conduction. Shown in Fig. 5.7 are steady-state temperature profiles of adiabatic reactors with linear kinetics and different axial heat Péclet numbers ( $Pe_h$ ). Larger  $Pe_h$  leads to sharper axial temperature profile. When  $Pe_h$  is large, the width of the temperature front in the non-reactive zone can be approximated as (Yu et al., 2013)

$$\Delta z = 2\sqrt{\frac{2}{Pe_h}}.$$

When  $\Delta T_{ad}$  (or  $\beta$ ) is large, the temperature profile is affected by both heat conduction ( $Pe_h$ ) and heat generation ( $\beta$ ). Because of the strong nonlinearity, reactors with finite  $Pe_h$  can have multiple steady-states. In order to study bifurcation behaviors, the steady-state forms of the simplified models (boundary value problems) are solved using the shooting method with sensitivity functions (Subramanian and Balakotaiah, 1996).

### 5.2.1 Linear Kinetics

Shown in Fig. 5.8, are bifurcation diagrams of steady-state conversions of adiabatic reactors with different  $Pe_h$ , assuming linear kinetics and  $Pe_m/Pe_h = 10$  (typical for ceramic monoliths). The  $\Delta T_{ad}$  is chosen to be 200 K, which corresponds to the oxidation of  $\sim 2\%$   $CO$  or  $\sim 3,000$  ppm  $C_3H_6$ . Reactors with lower  $Pe_h$  will exhibit hys-

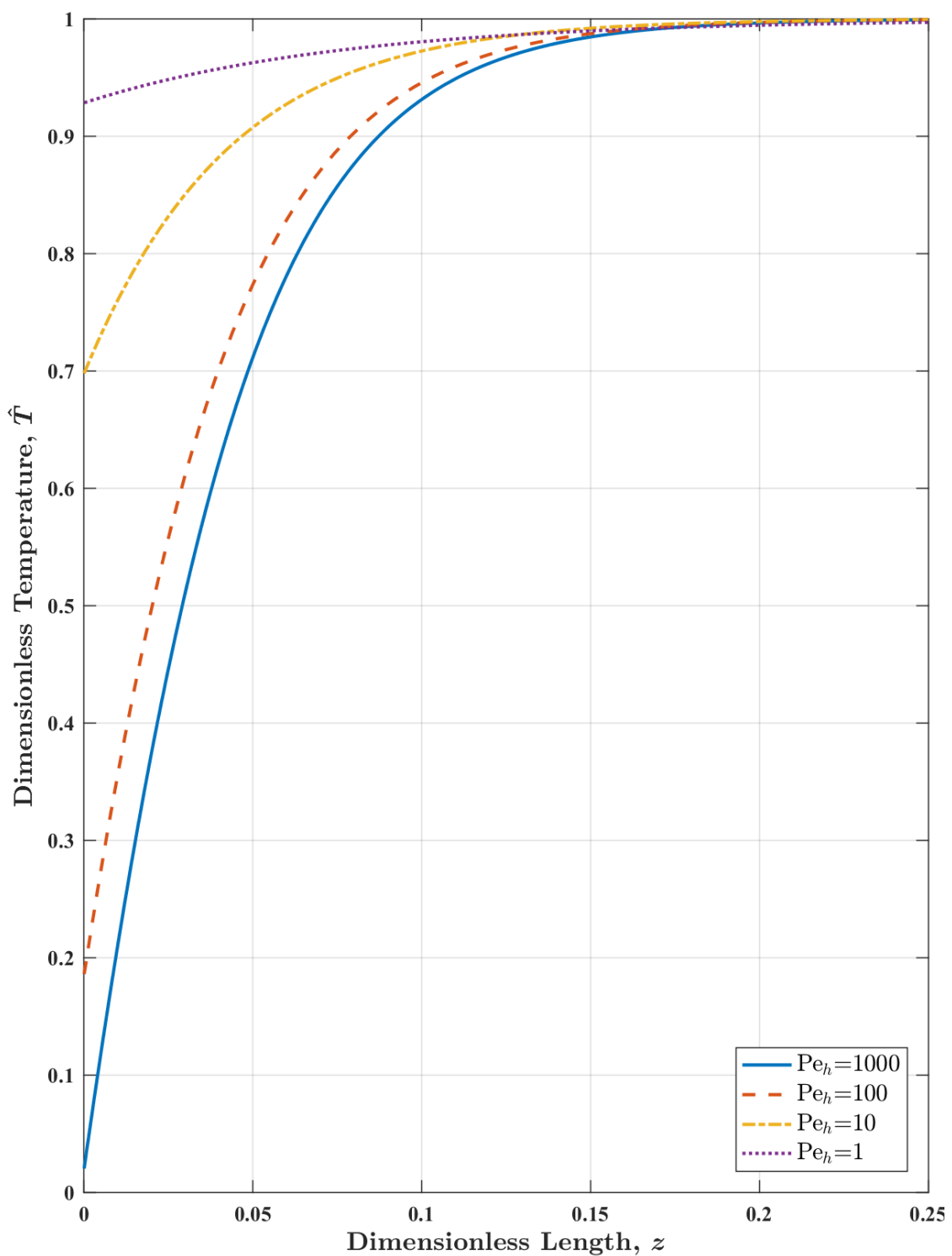


Figure 5.7: Steady-state axial temperature profiles of adiabatic reactors with first-order kinetics and different axial heat Péclet numbers ( $Pe_h$ ). ( $E_a = 100$  kJ/mol,  $Da_0 = 10^{10}$ ,  $\Delta T_{ad} = 12$  K,  $T^{in} = 600$  K,  $Pe_m/Pe_h = 10$ )

teresis and a lower ignition temperature. Thus, unless  $Pe_h$  in both lab- and full-scale reactors are very large, their behaviors will be qualitatively different.

Typically in full-scale ceramic monolith reactors,  $Pe_h \sim 100$  leading to a PFR-like behavior, while  $Pe_h$  in lab-scale reactors are 10 to 100 times smaller leading to hysteresis behaviors. In full-scale metallic monolith reactors where  $Pe_h \sim 10$ , there can be hysteresis in both lab- and full-scale reactors, but the hysteresis in lab-scale will be more pronounced. Thus, a direct scale-up based on lab-scale performance is usually not possible, because the estimated ignition temperature will be lower. Also, the ignited branch, where the steady-state conversion can stay high even when the inlet temperature drops, does not exist or shrinks in the full-scale reactors. It can be noted from Fig. 5.8 that when  $Pe_h$  is very small, the width of the hysteresis region does not decrease monotonically with increase in  $Pe_h$ . The reason for this may be that when  $Pe_h$  is sufficiently small (suggesting that temperature profile is close to uniform),  $Pe_m = 10Pe_h$  is still large enough to create a relatively sharp concentration profile, as illustrated in Fig. 5.9, hence for a certain  $Pe_h$  range the model is approaching the lumped thermal reactor asymptote which has a larger hysteresis region (Luss and Balakotaiah, 1984).

The width of the hysteresis region is also impacted by the thermal effects ( $\Delta T_{ad}$ ), since the more heat is generated, the lower inlet temperature is needed to maintain high steady-state conversion. To illustrate this effect, we calculated the bifurcation sets (ignition/extinction loci) of adiabatic reactors at different  $Pe_h$  as shown in Fig. 5.10. After  $\Delta T_{ad}$  exceeds a certain value (hysteresis point), the width of the hysteresis region increases monotonically with  $\Delta T_{ad}$ . From Fig. 5.10, we can see that the ignition locus is almost vertical suggesting that the ignition temperatures are not sensitive to the thermal effects. Thus, the widening of the hysteresis region is mainly in the form of lower extinction temperatures.

The hysteresis points are of special interests, since they indicate the boundary

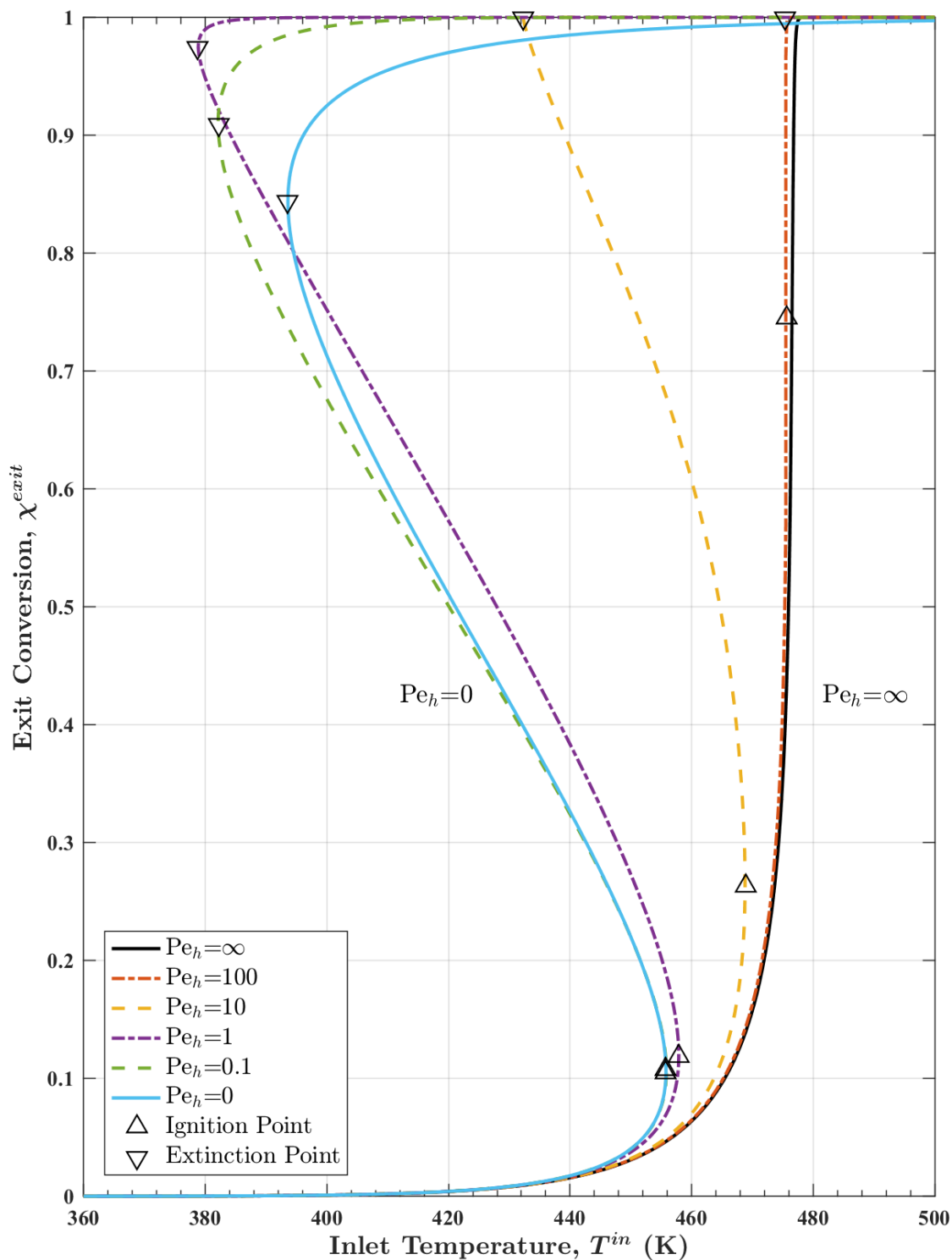


Figure 5.8: Bifurcation diagrams of steady-state exit conversion versus inlet temperature in adiabatic reactors with first-order kinetics and different axial heat Péclet numbers ( $Pe_h$ ). ( $E_a = 100$  kJ/mol,  $Da_0 = 10^{10}$ ,  $\Delta T_{ad} = 200$  K,  $Pe_m/Pe_h = 10$ )

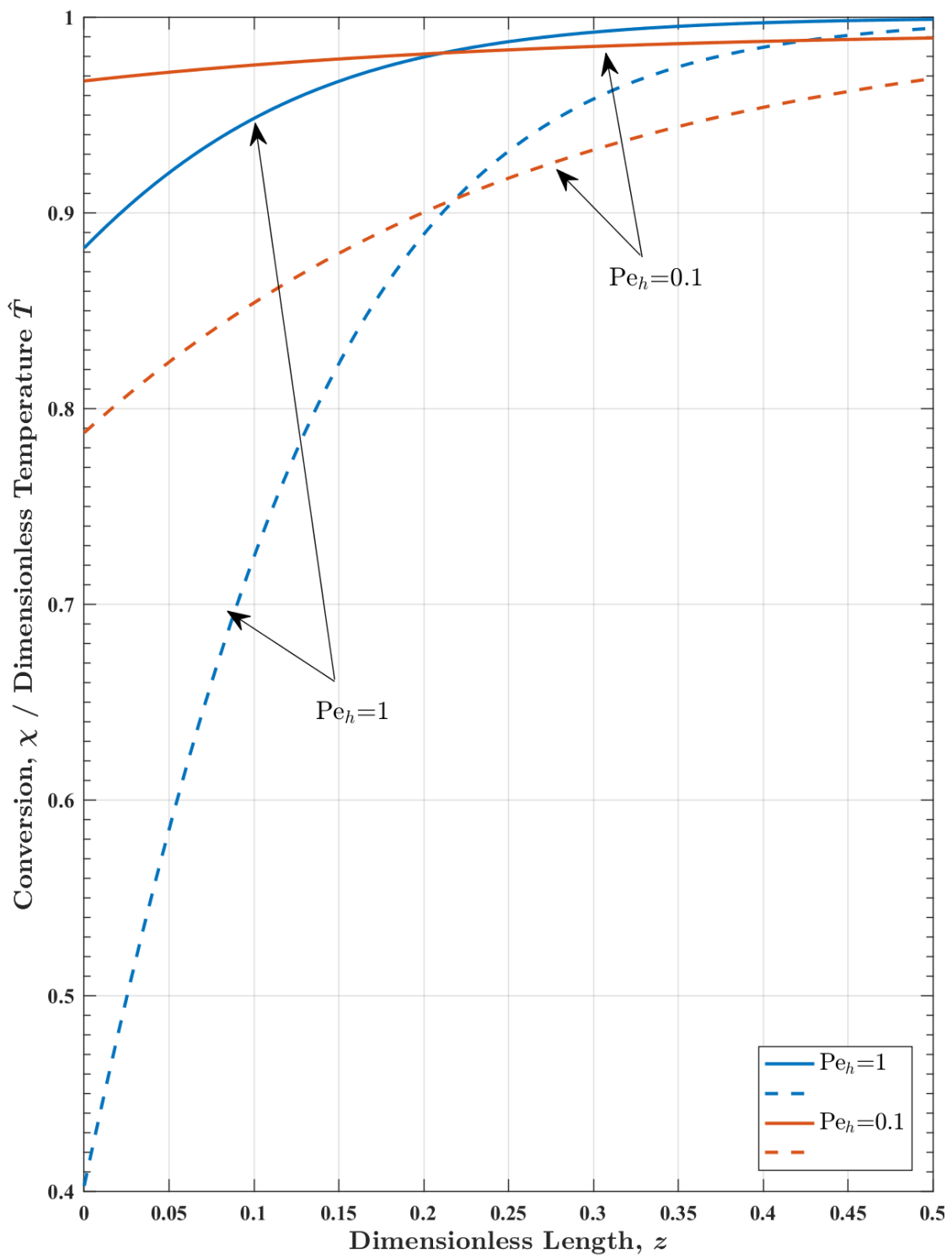


Figure 5.9: Steady-state axial temperature (solid line) and conversion (dashed line) profiles of adiabatic reactors with first-order kinetics and small  $Pe_h$ . ( $E_a = 100$  kJ/mol,  $Da_0 = 10^{10}$ ,  $\Delta T_{ad} = 200$  K,  $T^{in} = 400$  K,  $Pe_m/Pe_h = 10$ )

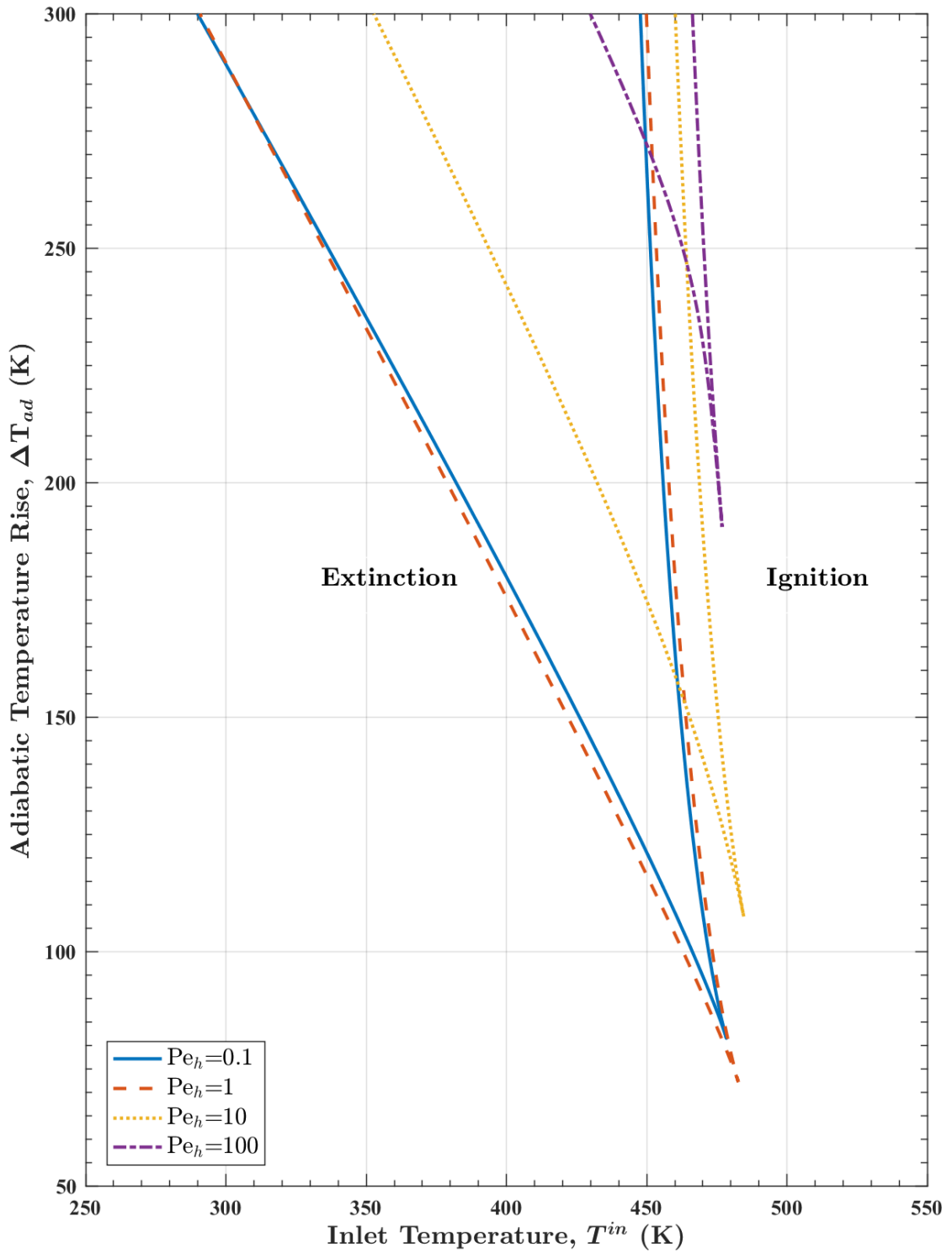


Figure 5.10: Ignition/extinction loci of adiabatic reactors with first-order kinetics and different axial heat Péclet numbers ( $Pe_h$ ). ( $E_a = 100$  kJ/mol,  $Da_0 = 10^{10}$ ,  $Pe_m/Pe_h = 10$ )

of single- and multiple-solution regions and determine whether the differences between lab- and full-scale reactors are qualitative. Shown in Fig. 5.11, are hysteresis loci of adiabatic reactors with different  $Pe_m/Pe_h$  ratios projected on the  $(\Delta T_{ad}, Pe_h)$  plane. For larger  $Pe_h$ , the adiabatic temperature rise required for hysteresis increases exponentially with  $Pe_h$  (Balakotaiah, 1996). The hysteresis loci of reactor with  $Pe_m/Pe_h = 1$  (more realistic for packed bed reactors) and  $Pe_m/Pe_h = \infty$  (mass dispersion is neglected) divide the plane into three regions. The region (painted in blue) above the hysteresis locus with  $Pe_m/Pe_h = 1$  is the multiple-solution region; the region (painted in red) below the hysteresis locus with  $Pe_m/Pe_h = \infty$  is the single-solution region. The region in between these two lines is the transitional region where the material of the monolith ( $Pe_m/Pe_h$  ratio) determines whether the reactor exhibits hysteresis. For larger  $Pe_h$ , the hysteresis locus with  $Pe_m/Pe_h = \infty$  is a good approximation for both ceramic and metallic monolith reactors. In Fig. 5.11, some typical operation points are marked as stars. The blue six-pointed star indicates a full-scale ceramic reactor with  $\Delta T_{ad} = 200$  K. The red five-pointed star indicates a full-scale metallic reactor or a lab-scale ceramic reactor with 1/3 of the full length. The green four-pointed star indicates a lab-scale metallic reactor with 1/3 of the full length or a lab-scale ceramic reactor with 1/10 of the full length. For qualitative similarity, lab- and full-scale reactors should fall in the same region. Lab- and full-scale ceramic reactors often lie in different regions indicating qualitative differences. Although lab- and full-scale metallic reactors may lie in the same region, the qualitative difference is usually significant as shown in Figs. 5.8 and 5.10. The hysteresis loci are also projected on  $(\chi^{exit}, Pe_h)$  and  $(T^{in}, Pe_h)$  planes as shown in Figs. 5.12 and 5.13. These loci show how steady-state exit conversion  $\chi^{exit}$  and inlet temperature  $T^{in}$  at the hysteresis point vary with  $Pe_h$ . As shown in Fig. 5.10,  $T^{in}$  at hysteresis point is a good approximation for the ignition temperature, so Fig. 5.13 can also be interpreted as how ignition temperature varies with  $Pe_h$ .

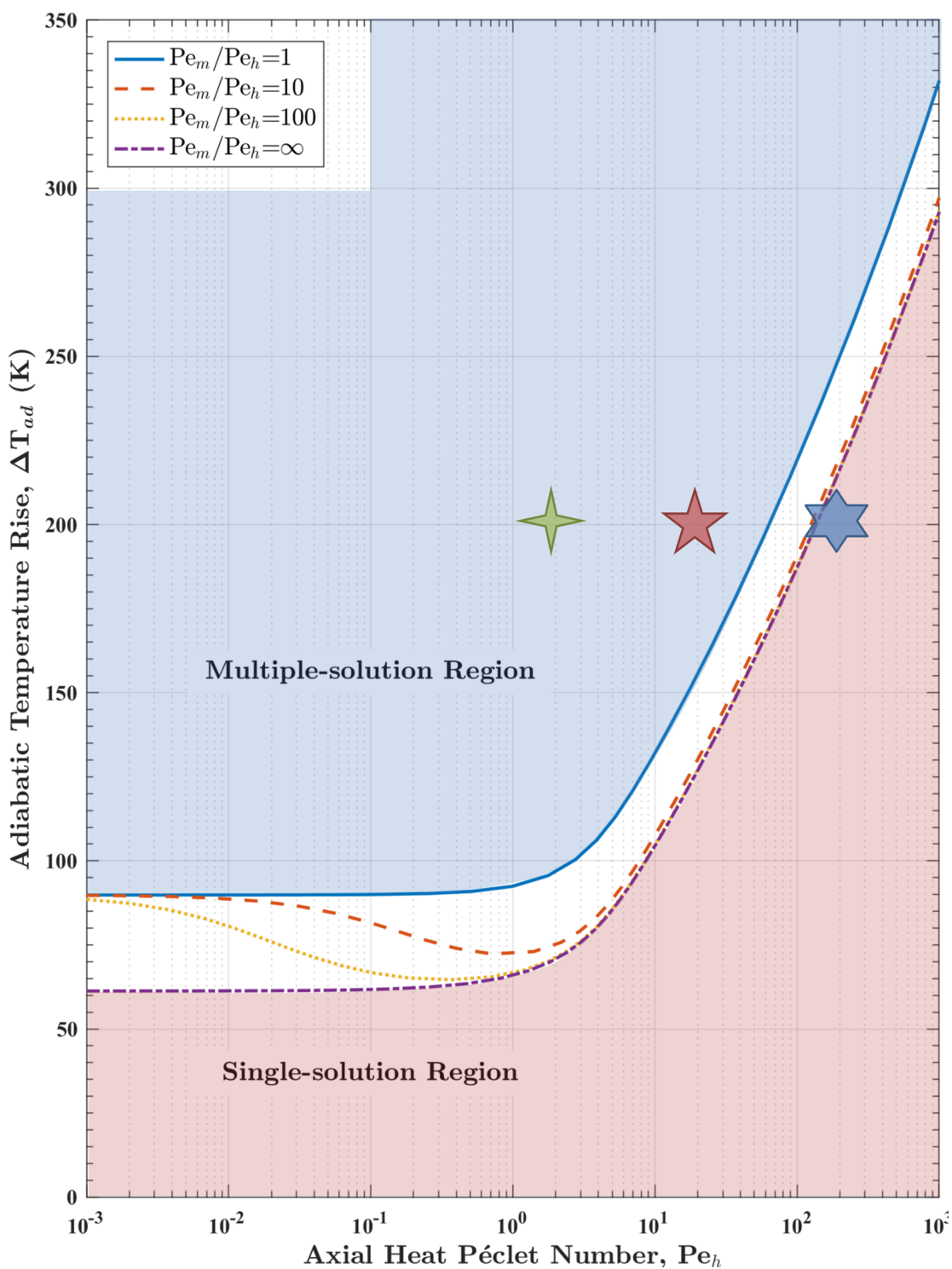


Figure 5.11: Hysteresis loci of adiabatic reactors with first-order kinetics and different  $Pe_m/Pe_h$  ratios in the  $(\Delta T_{ad}, Pe_h)$  plane. ( $E_a = 100$  kJ/mol,  $Da_0 = 10^{10}$ )

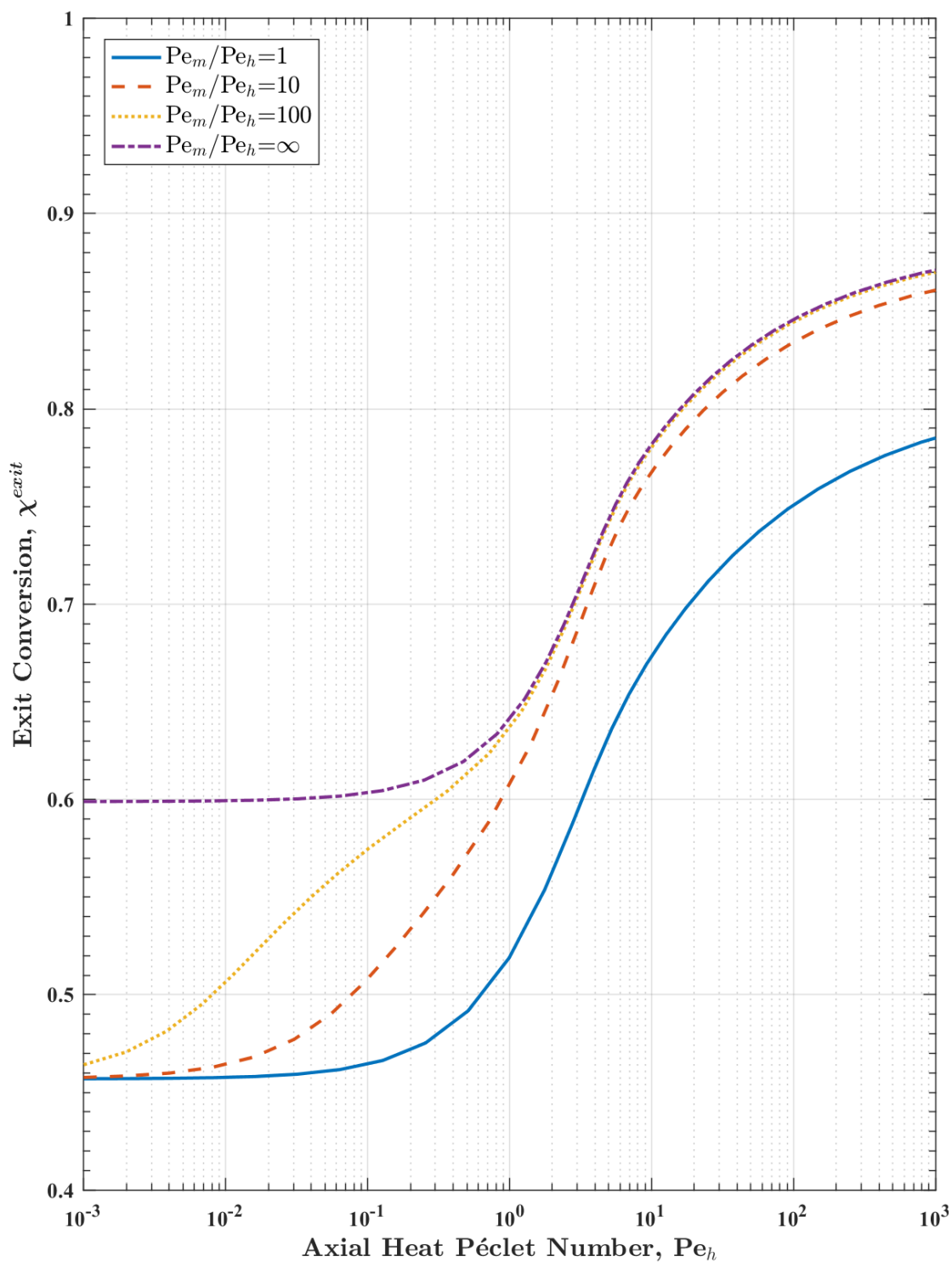


Figure 5.12: Hysteresis loci of adiabatic reactors with first-order kinetics and different  $Pe_m/Pe_h$  ratios in the  $(\chi^{exit}, Pe_h)$  plane . ( $E_a = 100$  kJ/mol,  $Da_0 = 10^{10}$ )

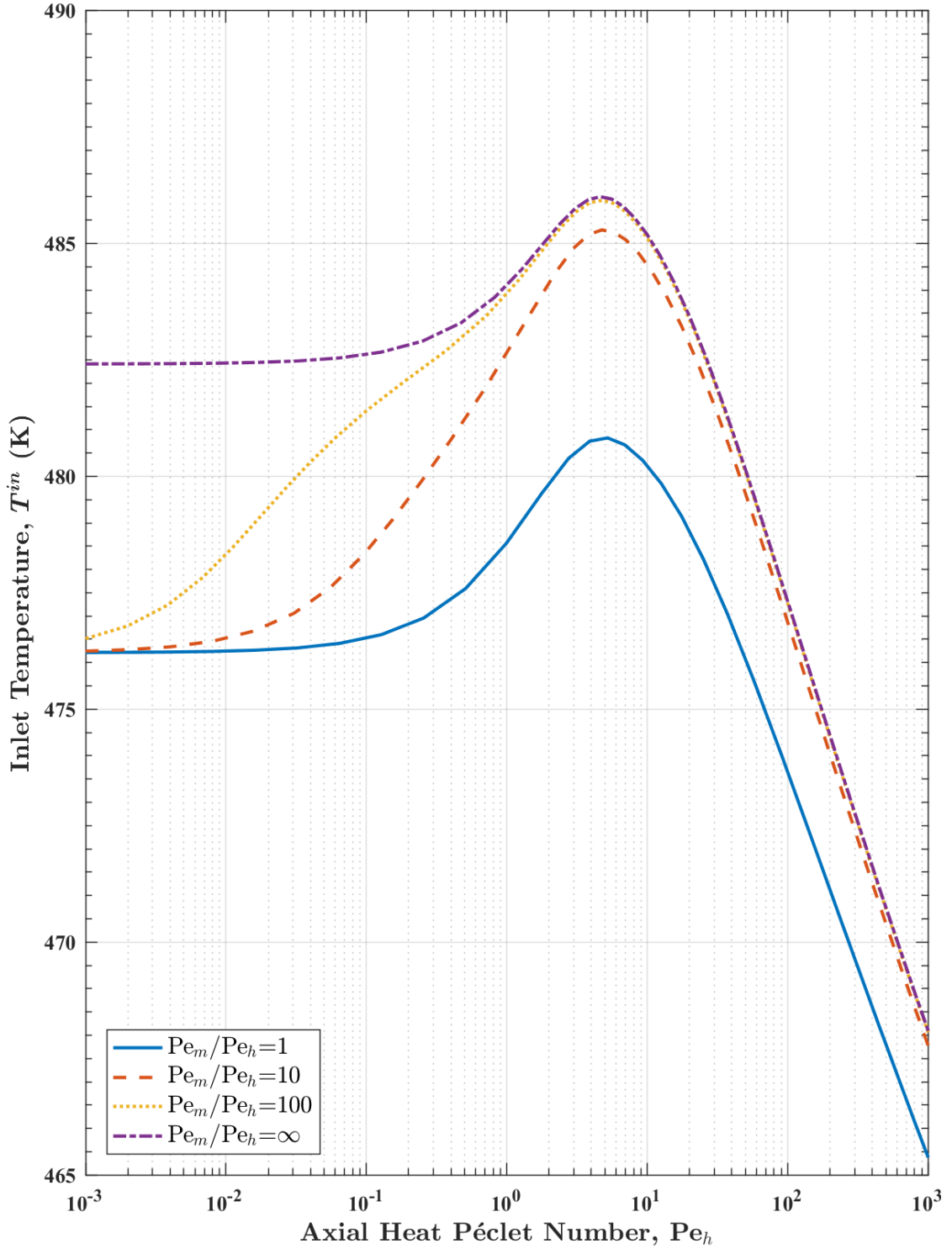


Figure 5.13: Hysteresis loci of adiabatic reactors with first-order kinetics and different  $Pe_m/Pe_h$  ratios in the  $(T^{in}, Pe_h)$  plane. ( $E_a = 100$  kJ/mol,  $Da_0 = 10^{10}$ )

### 5.2.2 Nonlinear Kinetics

In 5.2.1, we assumed the reaction is first-order, thus the nonlinearity is only from the exponential temperature dependence of the reaction rate. However, the nonlinearity can also appear in the rate expressions as we have shown in 5.1.2 for the isothermal case. Here, we show how nonlinear mechanism is coupled with non-isothermal effects. For the Langmuir-Hinshelwood kinetics, we assume the reactant is  $CO$ , the dimensionless adsorption equilibrium constant  $\kappa = 2000$  and  $\Delta T_{ad} \approx 10^{-2} X^{in}$  (in ppm). As shown in Fig. 5.14, the combined effect of Langmuir-Hinshelwood kinetics and non-isothermal effects leads to a hysteresis region that is significantly wider than single effect cases. Taking the limit  $Pe_h \rightarrow 0$  for example, the width of hysteresis region for adiabatic operation with Langmuir-Hinshelwood kinetics is 167 K compared to 62 K for adiabatic operation with first-order reaction (non-isothermal effects alone) and 20 K for isothermal operation with Langmuir-Hinshelwood kinetics (nonlinear kinetics alone).

Nonlinear kinetics also affect the boundary of multiple-solution region. To illustrate this effect, we calculated the hysteresis loci and projected them on the  $(X^{in}, Pe_h)$  plane as shown in Fig. 5.15. The general trends of the loci are the same. However, comparing to first-order reaction case, the nonlinear kinetics significantly enlarged the multiple-solution region. Comparing to the isothermal case, thermal effects enlarged the multiple-solution region, especially for large  $Pe_h$ . A case with  $\kappa = 200$  is also calculated to show the transition from first-order to strong nonlinear kinetics.

### 5.2.3 Plots of Exit Conversion Versus Mid-bed Temperature

Laboratory-scale experimental data are often displayed by plotting the limiting reactant exit conversion as a function of the catalyst temperature at the mid-point of the monolith. The main reason for such plots is the belief that the kinetics can be

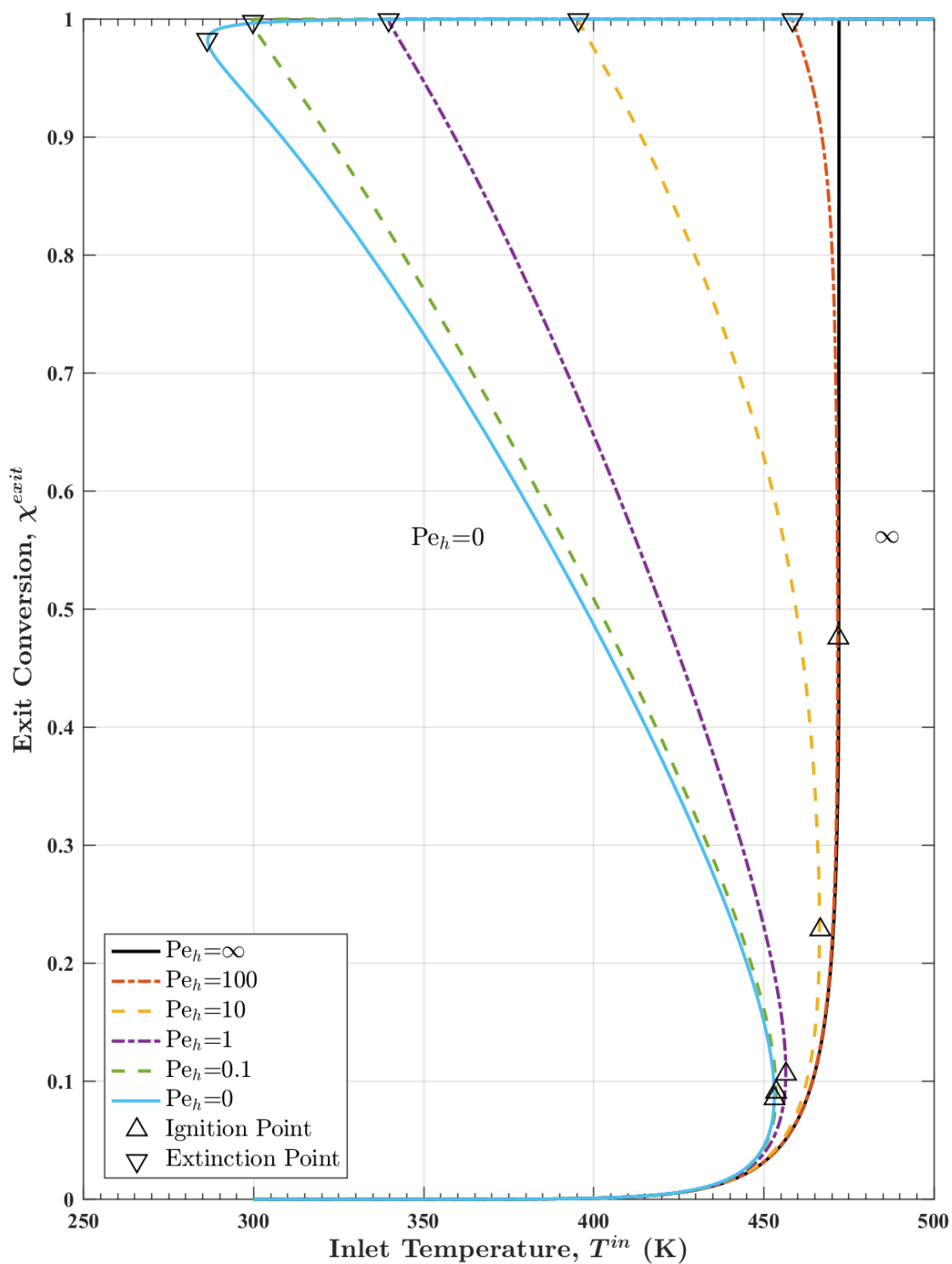


Figure 5.14: Bifurcation diagrams of steady-state exit conversion versus inlet temperature in adiabatic reactors with Langmuir-Hinshelwood kinetics and different axial heat Péclet numbers ( $Pe_h$ ). ( $E_a = 100$  kJ/mol,  $Da_0^{LH} = 10^{10}$ ,  $\kappa = 2000$ ,  $X_{CO}^{in} = 0.02$ ,  $Pe_m/Pe_h = 10$ )

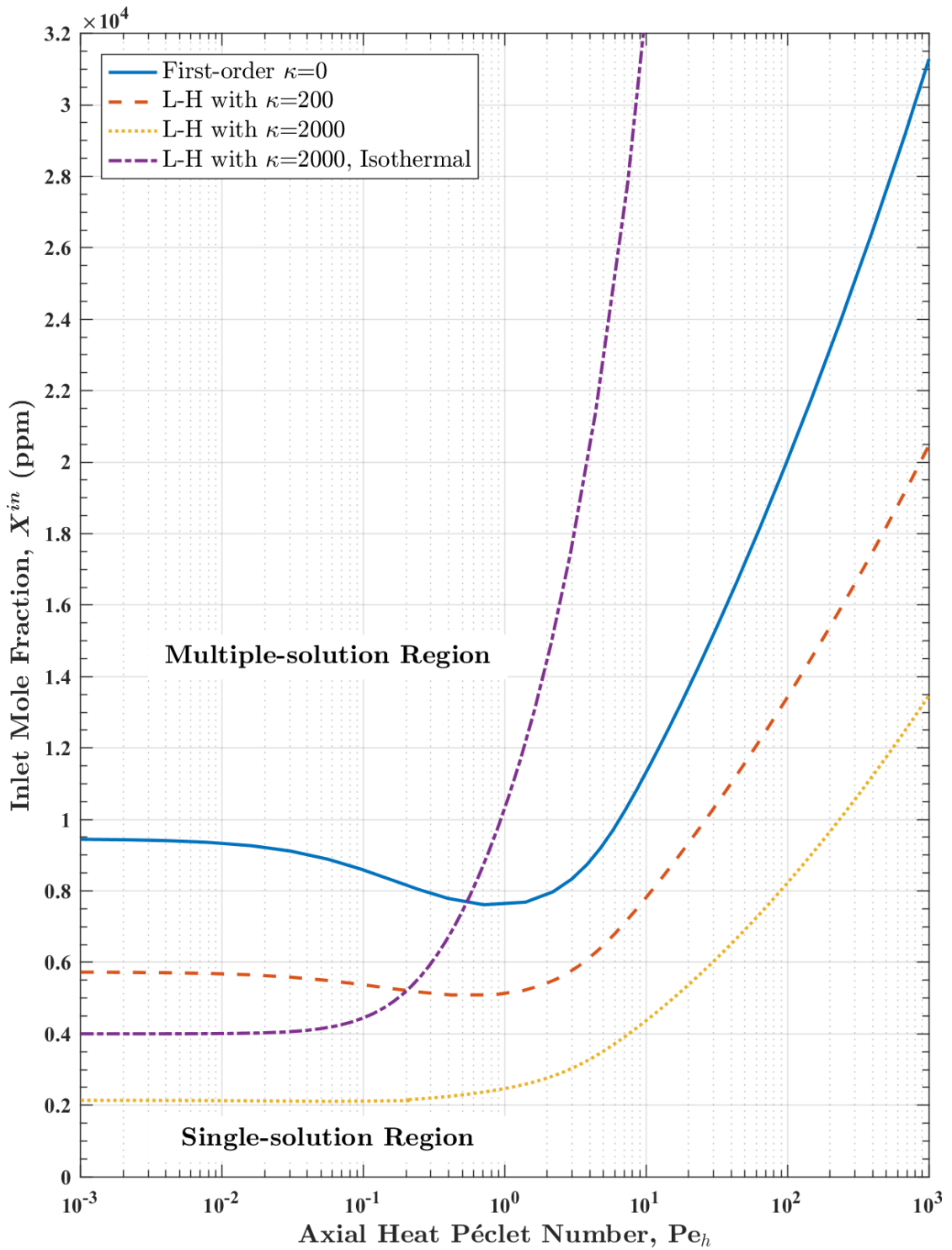


Figure 5.15: Hysteresis loci of adiabatic reactors with Langmuir-Hinshelwood kinetics and different adsorption equilibrium constants ( $\kappa$ ) on the  $(X^{in}, Pe_h)$  plane. ( $E_a = 100$  kJ/mol,  $Da_0^{LH} = 10^{10}$ ,  $Pe_m/Pe_h = 10$ )

determined more accurately if the temperature profile within the monolith is uniform. We examine here the validity of this assumption, especially for cases in which  $\Delta T_{ad}$  is not small.

Shown in Fig. 5.16, are the bifurcation diagrams of steady-state conversion versus inlet temperature (same as Fig. 5.8) and mid-bed temperature ( $T^{mid}$ ). We can see that for small  $Pe_h$  the curve of  $\chi^{exit}$  versus  $T^{mid}$  is single-valued and very similar to the isothermal reactor case (Fig. 5.1). This might lead to the belief that these plots are better for kinetic studies, since they can be treated as isothermal reactors at mid-bed temperatures. However, this type of plot is not a good way to present the results, because  $T^{mid}$  itself is an output of the system (unlike  $T^{in}$  which is an input) which is affected by inlet temperature, kinetics and adiabatic temperature rise ( $T^{mid} = T^{in} + \chi^{mid} \Delta T_{ad}$ ). Plotting two outputs versus each other may conceal the actual system behavior. More importantly, the single-valued plot of  $\chi^{exit}$  versus  $T^{mid}$  can be misleading, since part of the curve is unstable and cannot be observed experimentally. To illustrate this, we take the  $Pe_h = 0.1$  curves in Fig. 5.16 for example and plot them again in Fig. 5.17 with dotted part indicating unstable steady-states. By either slowly increasing or decreasing the inlet temperature, one can find either the light-off curve (upward arrows) or light-out curve (downward arrows). Thus, although the  $\chi^{exit}$  versus  $T^{mid}$  curve is single-valued in the bifurcation diagram, it still has hysteresis (as long as the corresponding  $\chi^{exit}$  versus  $T^{in}$  curve is multi-valued). Thus, we believe that  $\chi^{exit}$  versus  $T^{mid}$  plots provide no significant advantage over  $\chi^{exit}$  versus  $T^{in}$  plots.

In Fig. 5.16, we can also see for the same  $\chi^{exit}$ , the difference between  $T^{in}$  and  $T^{mid}$  decreases as  $Pe_h$  increases. This is due to shifting of the reaction zone. To illustrate this, we plot the axial temperature profiles of reactors with different  $Pe_h$ , at their extinction points (lowest possible temperature to have high conversion) in Fig. 5.18. For smaller  $Pe_h$ , high conversion can be achieved near the inlet of the reactor and the

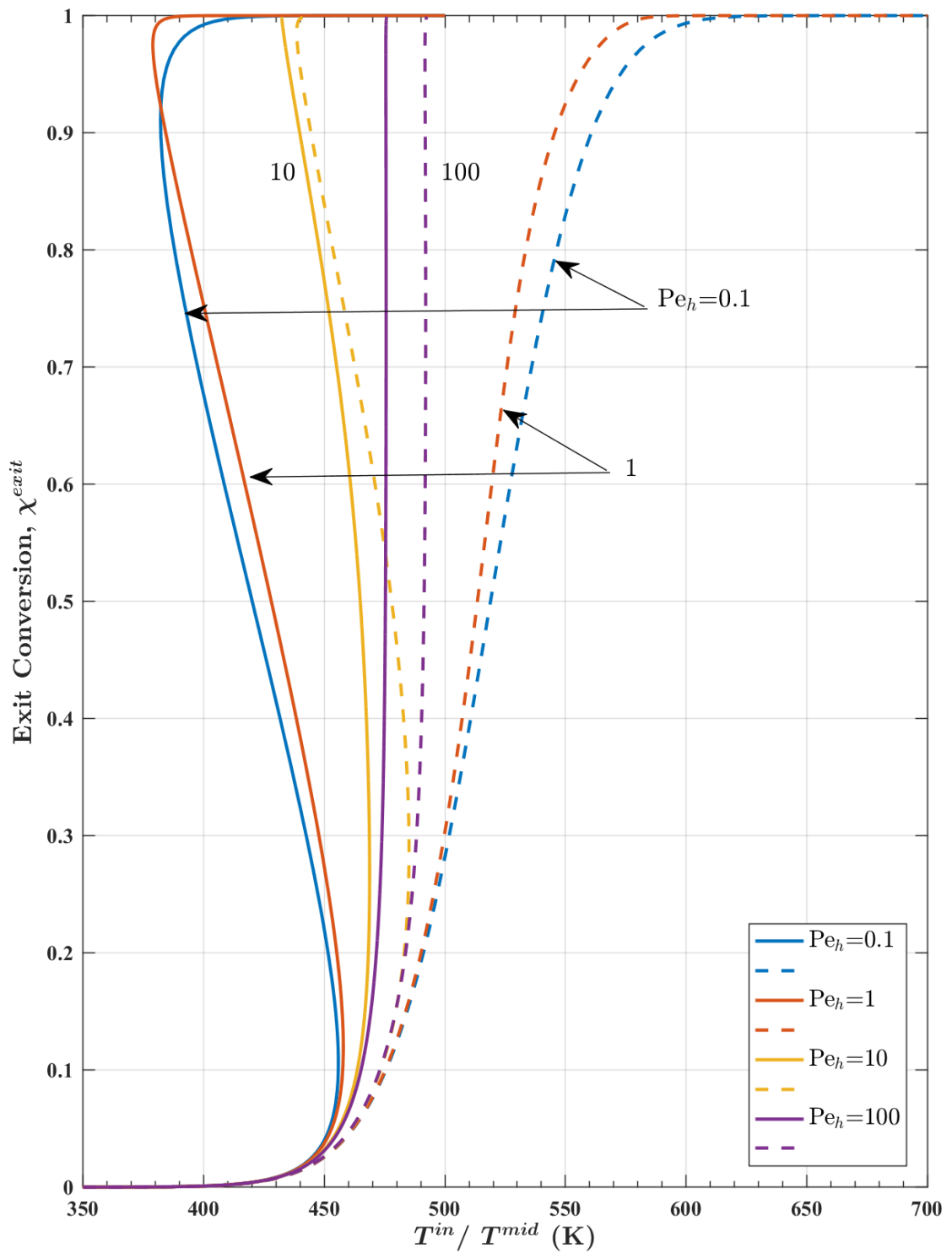


Figure 5.16: Bifurcation diagrams of steady-state exit conversion versus inlet temperature (solid) / mid-bed temperature (dashed) in adiabatic reactors with first-order kinetics and different axial heat Péclet numbers ( $Pe_h$ ). ( $E_a = 100$  kJ/mol,  $Da_0 = 10^{10}$ ,  $\Delta T_{ad} = 200$  K,  $Pe_m/Pe_h = 10$ )

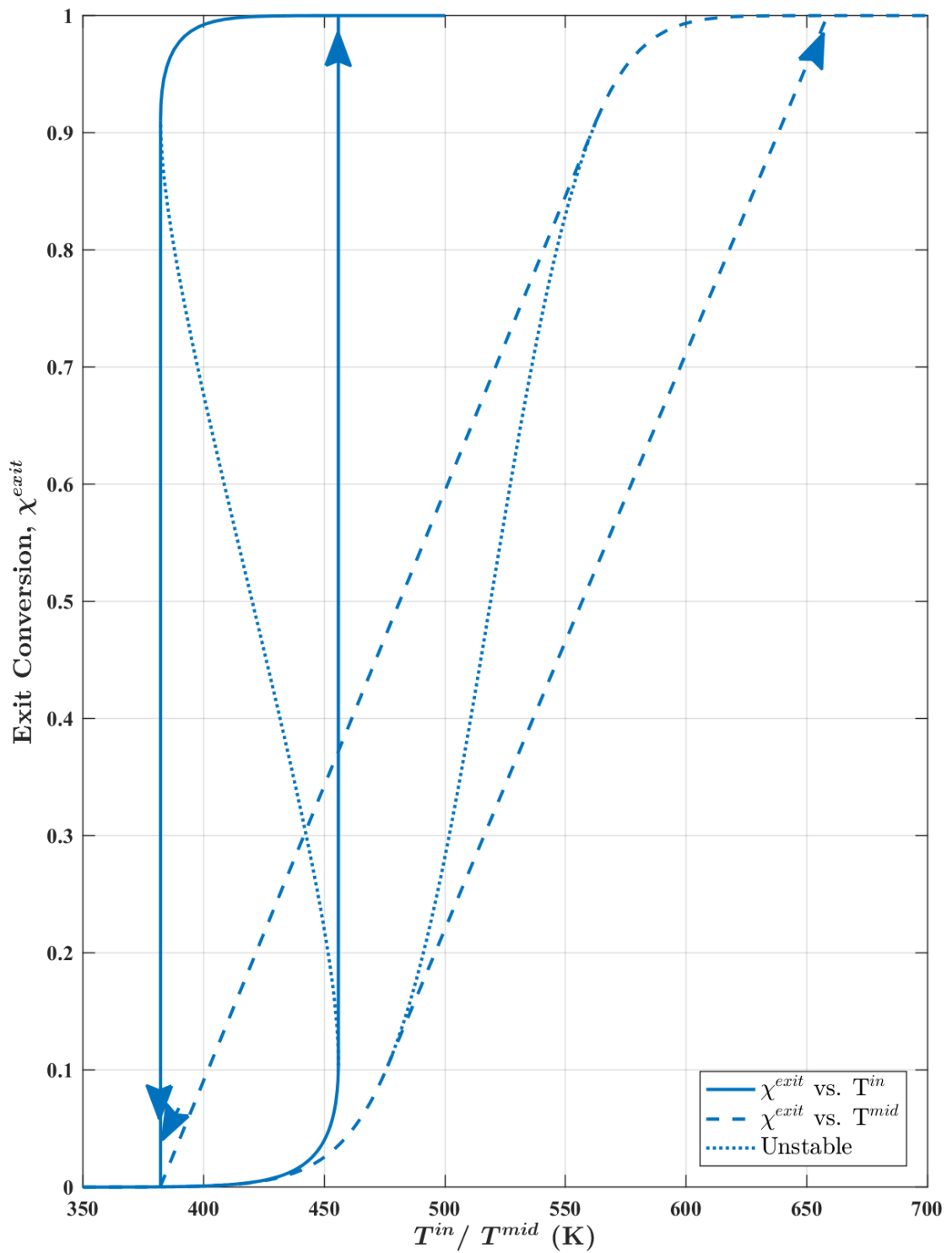


Figure 5.17: Bifurcation diagrams of steady-state exit conversion versus inlet temperature (solid) / mid-bed temperature (dashed) in adiabatic reactors with first-order kinetics. ( $E_a = 100$  kJ/mol,  $Da_0 = 10^{10}$ ,  $\Delta T_{ad} = 200$  K,  $Pe_h = 0.1$ ,  $Pe_m = 1$ )

temperature profile is near flat, thus  $T^{mid} - T^{in} \approx T^{exit} - T^{in} = \chi^{exit} \Delta T_{ad}$ . For larger  $Pe_h$ , high conversion is achieved only near the end of the reactor. Thus, even when exit conversion is high,  $\chi^{mid}$  is still small and the difference between  $T^{in}$  and  $T^{mid}$  will also be small. After the exit conversion reaches unity, if  $T^{in}$  keeps increasing, the reaction zone will shift towards the inlet and ultimately the profile will also become flat.

We note that multiple solutions disappear and the curve of  $\chi^{exit}$  versus  $T^{in}$  or  $\chi^{exit}$  versus  $T^{mid}$  are single-valued if  $\Delta T_{ad}$  is below the hysteresis locus in Fig. 5.11. However, to achieve a small enough  $\Delta T_{ad}$  the inlet reactant concentration may become so low that the measurement accuracy may be impacted. In such cases, the results presented in this work may be used to select the proper catalyst dimensions and reactant concentrations to obtain meaningful laboratory data that can be used for kinetic parameter estimation.

### 5.3 Impact of Interphase Gradients

Although the analysis so far is mainly based on a one-dimensional pseudo-homogeneous reactor model (described in 4.3.2), the conclusions are valid for small excursions from the assumptions. Here, we examine the impact of interphase (or radial) gradients. In the pseudo-homogeneous model, the transverse Péclet numbers are either neglected ( $P_m = P_h = 0$ ) or lumped into effective Péclet numbers. Since the typical  $P_m$  value of an after-treatment reactor is of the order 0.01, the assumption is usually valid. As shown in Fig. 5.19,  $P_m = P_h = 0.01$  leads to negligible deviation from the pseudo-homogeneous model. Even when the interphase gradients are larger ( $P_m = P_h = 0.1$  which is one order of magnitude larger than typical values), the pseudo-homogeneous model can predict the ignition and extinction temperatures with only small errors.

However, since the transverse Péclet numbers are never actually zero, when the

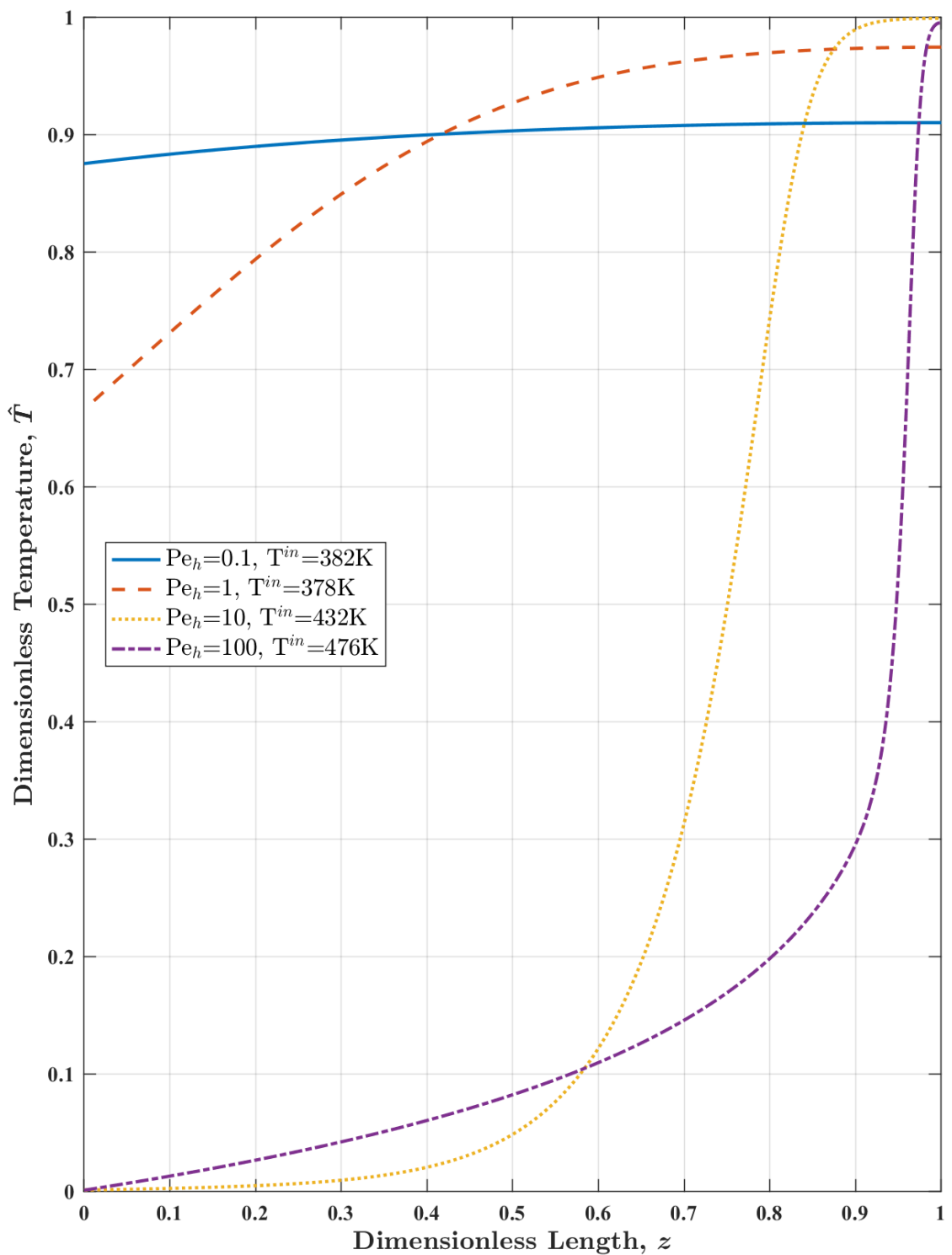


Figure 5.18: Steady-state axial temperature profiles of adiabatic reactors with first-order kinetics and different axial heat Péclet numbers ( $Pe_h$ ) at extinction temperatures. ( $E_a = 100$  kJ/mol,  $Da_0 = 10^{10}$ ,  $\Delta T_{ad} = 200$  K,  $Pe_m/Pe_h = 10$ )

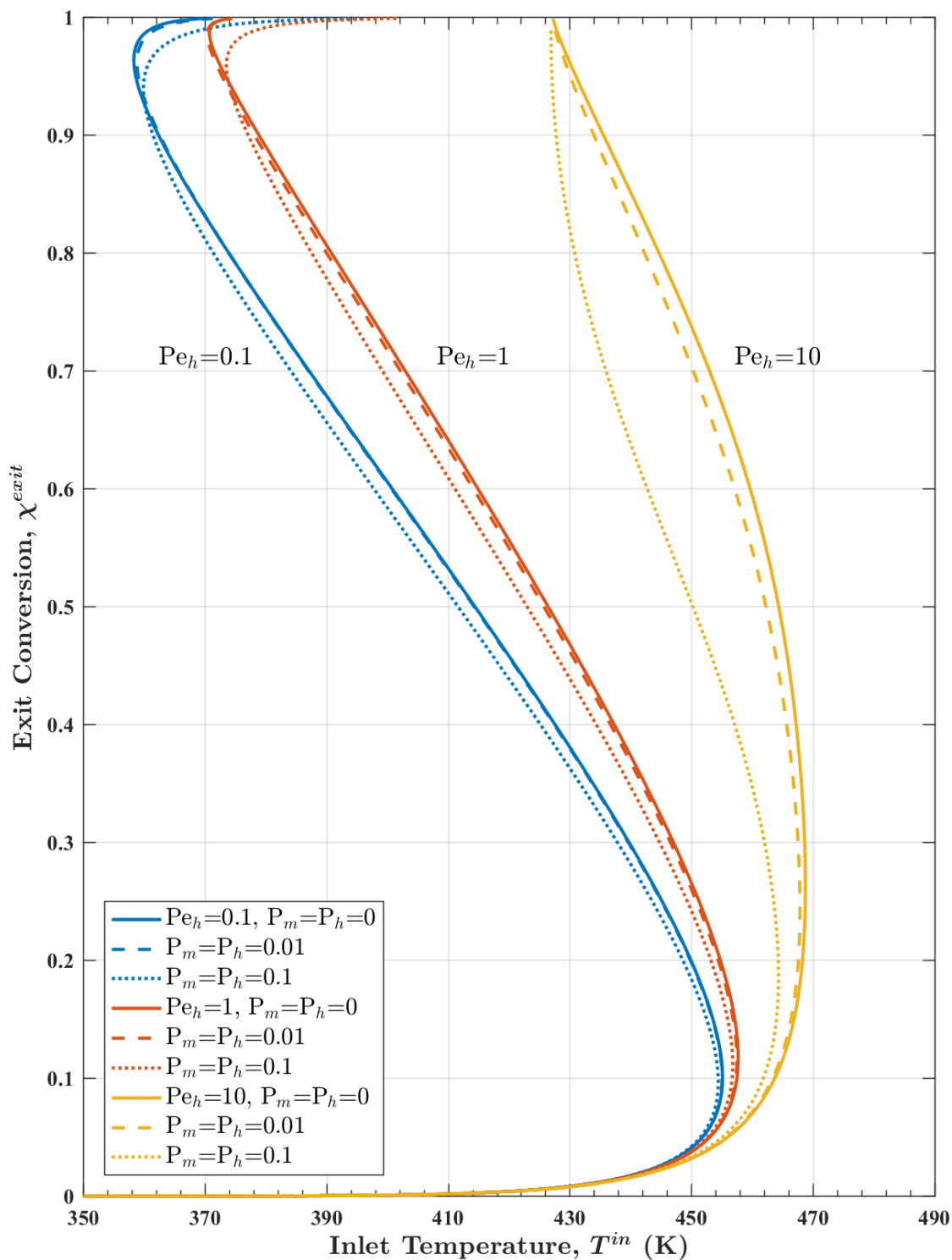


Figure 5.19: Bifurcation diagrams of steady-state exit conversion versus inlet temperature in adiabatic reactors with first-order kinetics, different axial heat Péclet numbers ( $Pe_h$ ) and different transverse Péclet numbers ( $P_m$  and  $P_h$ ). ( $E_a = 100 \text{ kJ/mol}$ ,  $Da_0 = 10^{10}$ ,  $\Delta T_{ad} = 200 \text{ K}$ ,  $Pe_m = \infty$ )

axial Péclet numbers are very large (axial dispersion/conduction effects are negligible) the transverse Péclet numbers (interphase mass and heat transfer) will dominate the reactor behavior. This can be qualitatively understood from the definition of the effective Péclet numbers (Eq. 4.19). When the axial Péclet number ( $Pe$ ) is very large, the effective Péclet number ( $Pe_{eff}$ ) equals to the reciprocal of the transverse Péclet number ( $P$ ). The usage of the effective Péclet number is only quantitatively correct for small  $P$ , large  $Pe$  and small  $\Delta T_{ad}$  (such that the model does not exhibit hysteresis), but it can help to predict qualitatively the behavior of a one-dimensional two-phase model (described in 4.3.1) even outside its applicable region.

To further illustrate the impact of interphase gradients, we calculated the hysteresis locus for the two-phase model with small  $P_m$  and  $P_h$  as shown in Fig. 5.20. Here, we only solve the  $Pe_m = \infty$  case since it captures the lower boundary of the hysteresis loci with different  $Pe_m/Pe_h$  ratios (as illustrated in Fig. 5.11), and thus conservatively defines the boundary of single-solution region. From Fig. 5.20, we can see that for larger  $Pe_h$  the hysteresis locus for the two-phase model does not increase exponentially as in the pseudo-homogeneous model. Instead, the hysteresis locus will reach a plateau where it is not sensitive to  $Pe_h$ , but dominated by  $P_h$ . This trend can also be qualitatively predicted by the effective Péclet number, where the plateau of the hysteresis is determined by the reciprocal of the transverse Péclet number. When  $P_m$  and  $P_h$  are small and  $Pe_h$  is not very large, the pseudo-homogeneous model (with lumped effective parameters) gives a very good approximation of the two-phase model.

## 5.4 Impact of Heat Loss

So far the analysis is based on either adiabatic reactors (no heat exchange with surroundings) or isothermal reactors (infinitely fast heat exchange with furnace/surroundings).

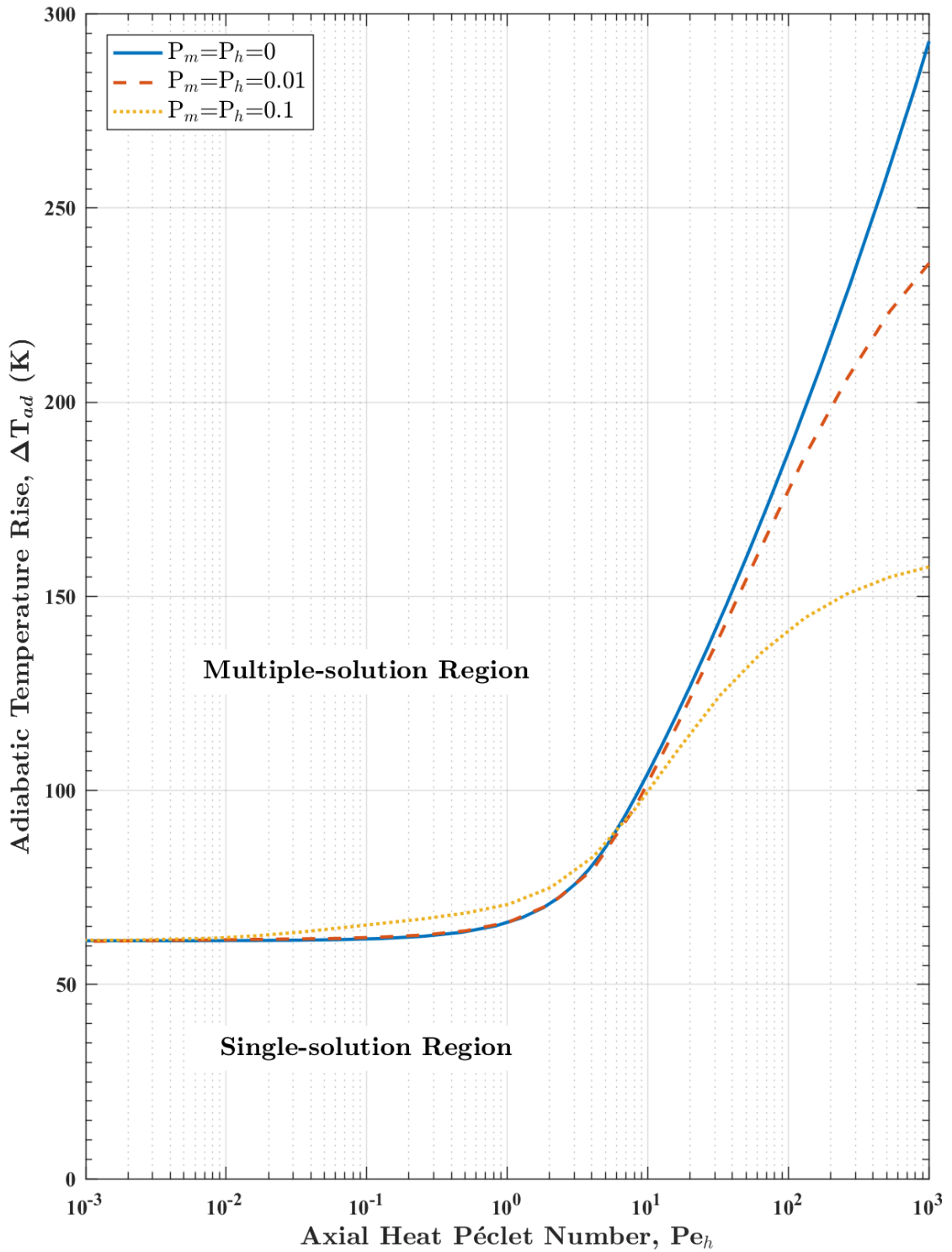


Figure 5.20: Hysteresis loci of adiabatic reactors with first-order kinetics and different transverse Péclet numbers ( $P_m$  and  $P_h$ ) in the  $(\Delta T_{ad}, Pe_h)$  plane. ( $E_a = 100$  kJ/mol,  $Da_0 = 10^{10}$ ,  $Pe_m = \infty$ )

Although a practical reactor is never adiabatic nor isothermal, adiabatic reactors are good approximations for full-scale reactors while lab-scale reactors are closer to isothermal reactors. However, if the adiabatic temperature rise  $\Delta T_{ad}$  is too small in the full-scale or too large in the lab-scale reactor, they will diverge from ideal assumptions. Here, we present a preliminary analysis of the impact of heat loss to surroundings on the scale-up performance of monolith reactors.

In general, when there is heat exchange with the surroundings, the temperature in the monolith varies both in the axial and transverse directions and the analysis cannot be based on a single channel. However, when the transverse dimensions of the monolith are small or the effective conductivity in the radial direction is large (or the so called Biot number is small), it is reasonable to assume that the major part of the temperature drop in the radial direction occurs near the wall. We make this assumption here and examine the case of finite external heat transfer by modification of the energy balance of the pseudo-homogeneous model,

$$\frac{1}{Pe_h} \frac{d^2 \hat{T}}{dz^2} - \frac{d\hat{T}}{dz} + Da_0 (1 - \chi) \exp\left(\frac{-1/\beta}{\hat{T} + \theta^{in}}\right) - \alpha \Delta \hat{T} = 0. \quad (5.10)$$

Here,  $\Delta \hat{T}$  is the temperature gradient (or difference) driving the external heat transfer. Further, if we assume that the external/ambient temperature is the same as the inlet temperature, which is consistent with lab experimental operations, we have

$$\Delta \hat{T} = \frac{T - T^{in}}{\Delta T_{ad}} = \hat{T}.$$

The dimensionless heat loss coefficient  $\alpha$  is given by

$$\alpha = \frac{UaL\delta_s}{\rho_f C_{p_f} \bar{u} R_\Omega},$$

where  $U$  is the overall heat transfer coefficient at the outer boundary,  $a$  is the external

heat transfer area per unit volume of the reactor (For a reactor of circular cross-section,  $a = 4/d_R$ , where  $d_R$  is the reactor diameter). The dimensionless heat loss coefficient  $\alpha$  can also be expressed in terms of characteristic time scales,

$$\alpha = \frac{UaL\delta_s}{\rho_f C p_f \bar{u} R_\Omega} = \frac{\tau}{\tau_h} \frac{\delta_s}{R_\Omega},$$

where

$$\tau_h = \frac{\rho_f C p_f}{Ua}$$

is the overall heat transfer time which has a typical range of 0.1 to 1 s for lab-scale units. The parameter  $\delta_s/R_\Omega$  is a fixed geometric factor which is usually in the range 1/4 to 1/3. Since the typical value for space time  $\tau$  is  $\sim 100$  ms, the dimensionless coefficient  $\alpha$  ranges from 0.03 to 0.3. Since  $\alpha = 0.03$  is usually very close to the adiabatic case,  $\alpha = 0, 0.1, 1$  and  $\infty$  are selected for parametric studies.

The dimensionless heat loss coefficient  $\alpha$  can affect the bifurcation behavior of the reactor. When  $\alpha = 0$ , the reactor is operated adiabatically and exhibits ignition/extinction behavior if the adiabatic temperature rise  $\Delta T_{ad}$  is large enough. When  $\alpha \rightarrow \infty$ , the reactor is isothermal and it does not exhibit bifurcation behavior unless there is nonlinearity in the rate expression, e.g. Langmuir-Hinshelwood kinetics. Shown in Fig. 5.21 are bifurcation diagrams of reactors with  $Pe_h = 1$  and different  $\alpha$  values. For a fixed  $\Delta T_{ad} = 200$  K, the width of the hysteresis region decreases with  $\alpha$  increasing. To better illustrate the effect of external heat transfer, bifurcation sets for different  $\alpha$  are calculated. Shown in Fig. 5.22 are ignition/extinction loci for different  $\alpha$  values. The hysteresis region significantly shrinks with increasing  $\alpha$ . The hysteresis point is also affected by  $Pe_h$  and  $\alpha$ . Shown in Fig. 5.23, are hysteresis loci for different  $\alpha$  values. With increasing external cooling, larger adiabatic temperature rise is needed for ignition/extinction behavior to appear. Ultimately, when  $\alpha \rightarrow \infty$ , the hysteresis locus will disappear since there is no nonlinearity in isothermal reactors

with linear kinetics. The results shown in Figs. 5.21-5.23 indicate that the light-off behavior of laboratory results with different amount of heat losses can be vastly different. This observation is important since most reported laboratory studies do not quantify the heat losses.

As stated earlier, for the case of finite external heat transfer, heat is not well-distributed within the channels and it is best to examine the impact of heat loss by using a two-dimensional model. However, the simpler model analyzed here reveals qualitatively the impact of external heat loss on scale-up. In 5.1 and 5.2, we have shown that even if lab- and full-scale reactors have the same dimensionless heat loss coefficient  $\alpha$  (both zero or both infinity), similarity generally does not exist. In this section, we illustrated that external heat loss can alone invalidate the similarity between the lab-scale and full-scale units when the parameter  $\alpha$  does not match in different scales.

## 5.5 Summary

In this part, we detailedly investigated three of the four main reasons for failure of scale-up in monolith reactors used in catalytic after-treatment. The results of our investigation may be summarized as follows: (i) As illustrated in Figs. 5.1-5.6, in isothermal reactors the conversion or light-off curves can be different in lab- and full-scale reactors when the effective mass Péclet numbers in the two systems are different with numerical values below the cut-off value of about 10. Equivalently, similarity exists in isothermal reactors with all geometric, kinetic parameters and space times matched only if the impact of mass dispersion is negligible, or the axial mass Péclet numbers in the two systems are much larger than 10 (with this cut-off value increasing further for strongly nonlinear kinetics such as the Langmuir-Hinshelwood with large numerical values for the dimensionless adsorption equilibrium constant). (ii) The

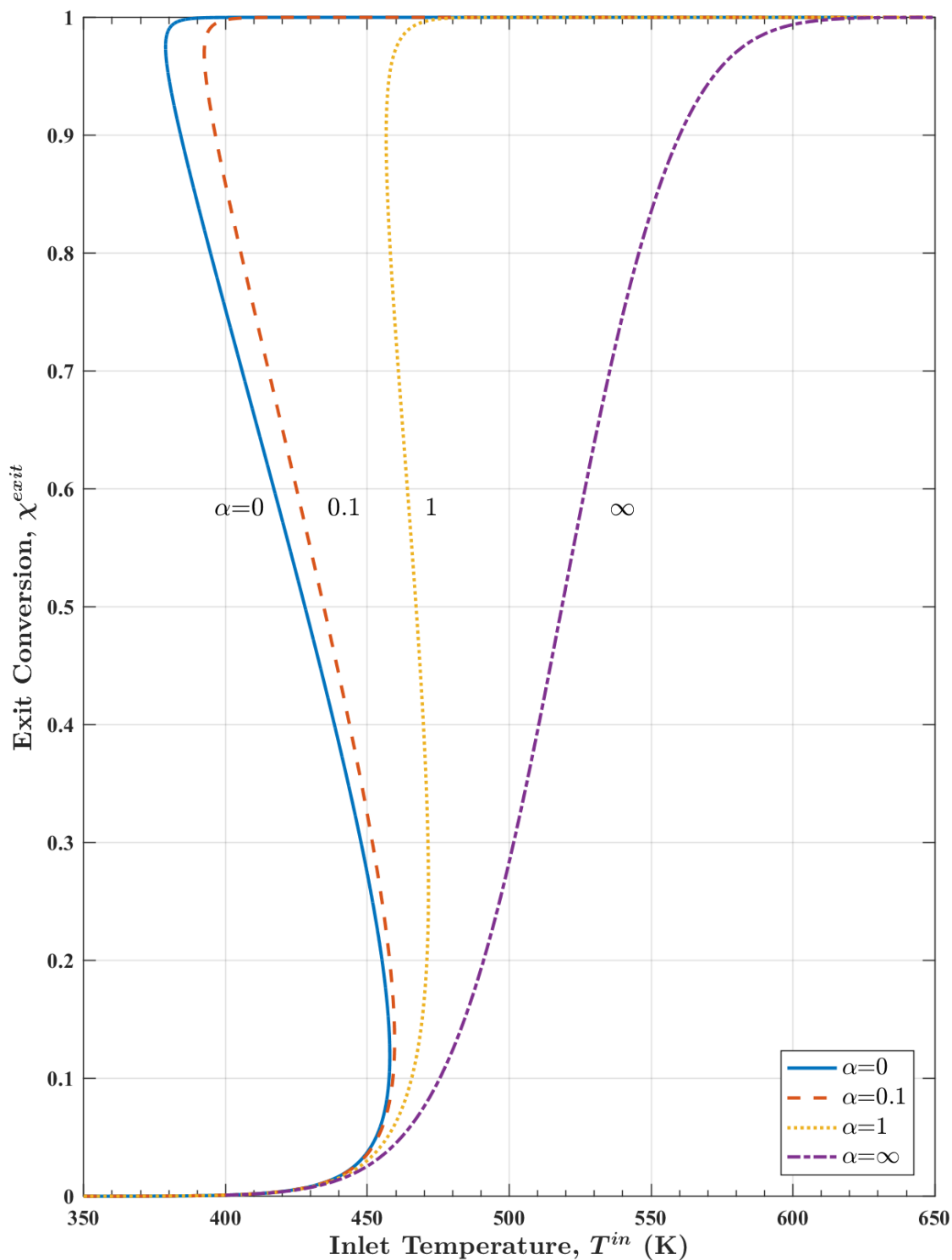


Figure 5.21: Bifurcation diagrams of steady-state exit conversion versus inlet temperature in reactors with first-order kinetics and different heat loss coefficients ( $\alpha$ ). ( $E_a = 100$  kJ/mol,  $Da_0 = 10^{10}$ ,  $\Delta T_{ad} = 200$  K,  $Pe_h = 1$ ,  $Pe_m = 10$ )

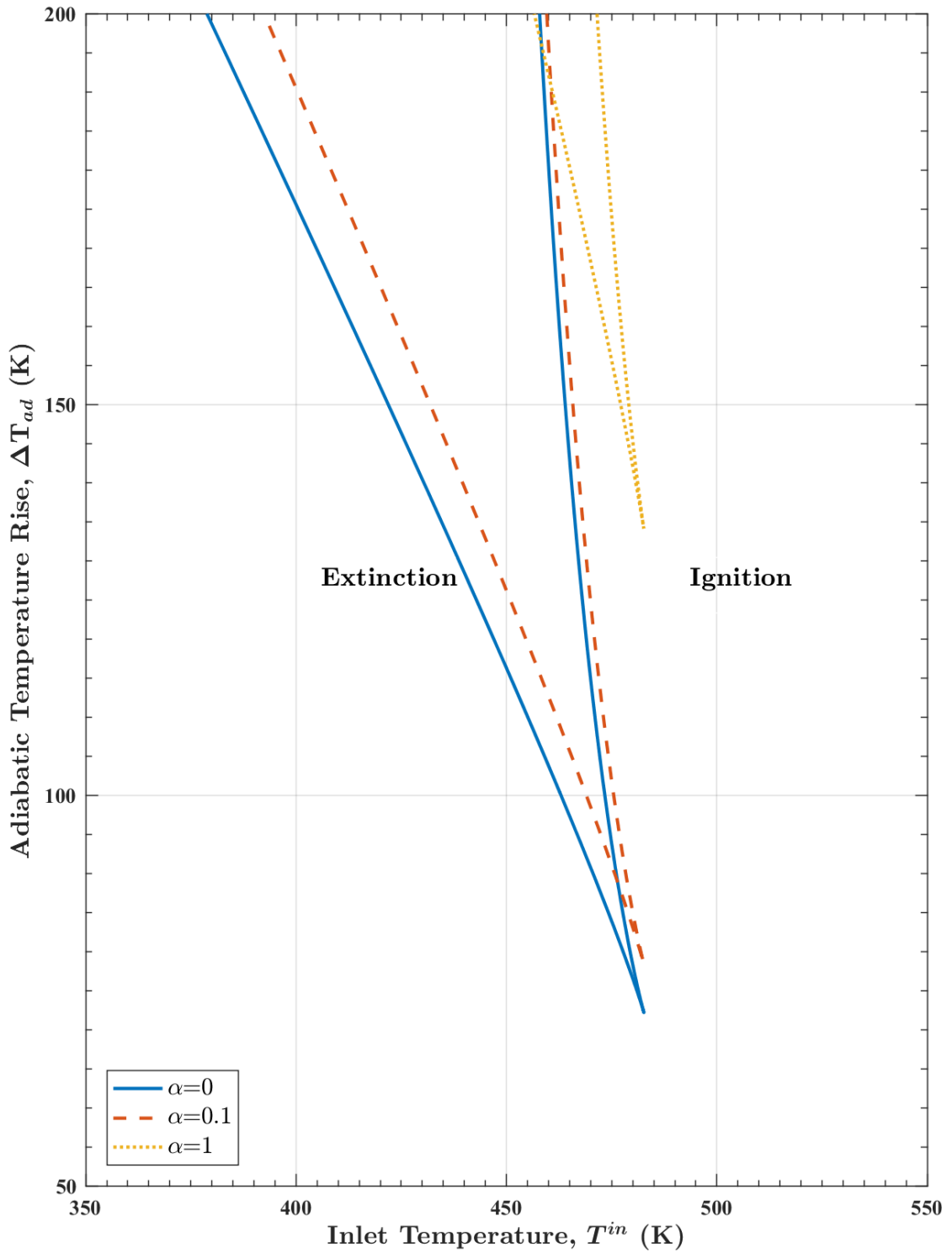


Figure 5.22: Ignition/extinction loci of reactors with first-order kinetics and different heat loss coefficients ( $\alpha$ ). ( $E_a = 100$  kJ/mol,  $Da_0 = 10^{10}$ ,  $Pe_h = 1$ ,  $Pe_m = 10$ )

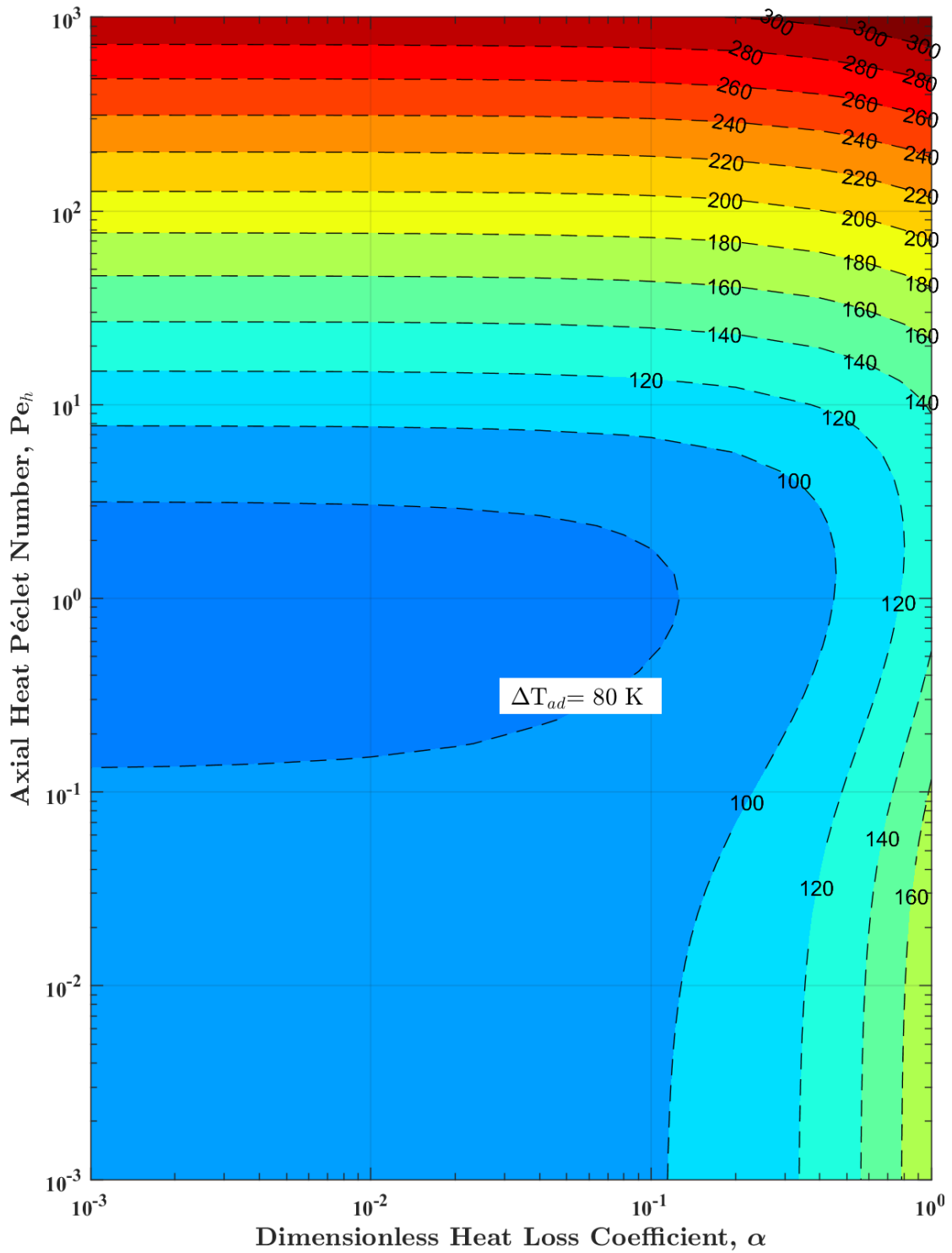


Figure 5.23: Hysteresis loci of reactors with first-order kinetics, different axial heat Péclet numbers ( $Pe_h$ ) and heat loss coefficients ( $\alpha$ ). ( $E_a = 100 \text{ kJ/mol}$ ,  $Da_0 = 10^{10}$ ,  $Pe_m/Pe_h = 10$ )

results shown in Figs. 5.8-5.11 imply that for typical concentrations used in after-treatment systems (with adiabatic temperature rise of about 200 K), the impact of heat dispersion is negligible only if the axial heat Péclet numbers in the two systems exceed the cut-off value of about 100 (and this cut-off value increases exponentially with increase in the adiabatic temperature). (iii) The results in Figs. 5.21-5.23 imply that impact of heat loss or heat exchange with surroundings is similar in the lab- and full-scale reactors only if the dimensionless heat loss coefficient  $\alpha$  is either close to zero (typically  $< 0.1$  indicating near adiabatic conditions in both systems) or close to infinity (typically  $>100$ , indicating near isothermal conditions in both systems). Thus, in the context of catalytic after-treatment reactors, the three parameters ( $Pe_m$ ,  $Pe_h$  and  $\alpha$ ) determine the conditions for similarity. It should also be pointed out that the current practice is such that the conditions for similarity are not satisfied in most cases (mostly because of the mismatch of these three parameters).

## **Part III**

# **Creeping Reaction Zones in Monolith Reactors**

# Chapter 6

## Introduction and Literature Review

One major challenge in exhaust after-treatment is reducing cold start emissions which accounts for a significant fraction of the total emissions. In a cold start, the catalyst is gradually heated by the hot exhaust gas from the ambient temperature to its ignition (or light-off) temperature, during which pollutants such as CO, HC and NO<sub>x</sub> pass through the reactor untreated. To promote reactor light-off and reduce the ignition temperature, the washcoat is loaded with a sufficient amount of Platinum group metals (PGM). Recent developments in advanced combustion strategies such as low temperature combustion (LTC), which result in a lower exhaust temperature and possibly lower pollutant concentrations (lower adiabatic temperature rise), make abating cold-start emissions and meeting environmental regulations even more challenging. In such cases, further increasing the metal loading is both technologically difficult and economically impractical. Thus, it is important to understand the impact of other design parameters and operating conditions on the light-off of monolith reactors.

During a cold start, ignition can occur at the front-end, in the middle or at the back-end of the reactor. Ramanathan et al. (2003) proposed detailed criteria for different types of ignition taking various parameters into account. After the reactor is ignited, it is desired that the reaction zone is maintained close to the inlet so that when small excursions in gas velocity, inlet temperature and concentrations do not quench the reactor. This can be achieved if front-end ignition is possible. In front-end ignition, due to high precious metal loading, high inlet temperature and/or high adiabatic temperature rise ( $B Da \gg 1$ , where  $B$  is the Zel'dovich number and  $Da$  is the Damköhler number), high conversion is achieved as soon as the hot exhaust

enters the reactor and warm up a small region near the inlet, then the generated heat is transported downstream by both conduction and convection. Front-end ignition is ideal for abating cold-start emissions, but it is becoming less practical due to lower exhaust temperature. When inlet temperature is low and precious metal loading is limited ( $BDa \sim 1$ ), ignition occurs near the exit of the reactor (back-end ignition), after which the reaction zone can (i) stay at the exit, (ii) creep upstream and stop in the middle, or (iii) creep all the way to the inlet under different conditions. Only in the third case, our desired ignited state can be achieved. Thus it provides a minimum requirement for reactor design and operation.

Creeping reaction zone is a well-known phenomenon first investigated in detail by Wicke and Vortmeyer (1959) in an adiabatic packed-bed reactor for CO oxidation on platinum catalyst. It was shown that depending on different operating conditions the reaction zone can propagate either downstream or upstream. There has been great interest in studying the creep reaction zones in packed-bed reactors through both experimental and modeling approaches (Vortmeyer and Jahnel, 1972; Eigenberger, 1972; Rhee et al., 1973, 1974). Vortmeyer and Jahnel (1972) conducted parametric studies and proposed empirical correlations for creep velocity and various parameters. Rhee et al. (1973,1974) used several different models to derive a physics-based correlation for the creep velocity. Hlavacek and coworkers studied experimentally the travelling waves in nonadiabatic packed-bed reactors and later used a pseudo-homogeneous model to analyze the phenomenon and develop correlations for the creep velocity (Puszynski and Hlavacek, 1980; Gatica et al., 1987). However, the correlation or criteria proposed in these previous works are either empirical, lacking physical insight; requiring solving the model numerically first, limiting the applicability. Although much work has been done on the subject, only a few applications with industrial relevance are reported in the literature. This is partially due to the fact that packed-bed reactors are usually maintained near a certain steady-state and

the dynamic behavior of creeping reaction zone is usually undesired. One exception is the reverse flow reactor proposed by Matros (1985), where the packed-bed reactors are operated with periodic flow reversal to utilize the dynamics of the reaction zones.

The only transport processes that can affect upstream are axial mass diffusion and heat conduction, between which heat conduction is usually the dominating process. Upstream creeping reaction zone can be explained by local balance of convection and axial heat conduction. When sufficient heat is generated and conduction is strong enough, an adjacent upstream area is ignited and the reaction zone creeps. Thus, we can anticipate that both thermal effects and heat conduction strongly impact this phenomenon. Since monolith reactors have a continuous solid phase, leading to a much larger (effective) thermal conductivity than packed bed reactors, upstream creeping reaction zones are much more common in monolith reactors than packed bed reactors. Due to frequent reactor start-up in after-treatment applications, studying this phenomenon is also of greater significance. However, few related work can be found in the literature. To the best of our knowledge, Yakhnin and Menzinger (2002) are the only investigators reported upstream creeping reaction zones in monolith reactors. Yet, their work is mainly focused on downstream traveling super-adiabatic extinction waves in catalytic combustion of hydrogen and shows a qualitative trend contradicting the one found in packed bed reactors (predicting upstream creeping at high gas velocity and downstream creeping at low gas velocity).

The main goal of this part is to study in some detail the upstream creeping reaction zones in monolith reactors using modeling approach, and address the following problems: (i) When does the reaction zone creeps upstream? (ii) When does the reaction zone creeps all the way to the inlet? (iii) How does the creep velocity depends on various design parameters and operating conditions?

# Chapter 7

## Model Development

In this work, we assume that the monolith reactor can be represented by a single channel. This is usually valid in exhaust aftertreatment reactors since the flow is well-distributed to the various channels through a cone and the reactors are operated almost adiabatically. It is also assumed that channels of various shapes (most commonly square-shaped) can be modeled with an axisymmetric model through proper shape normalization (Bhattacharya et al., 2004). Although the creeping reaction zone is due to axial conduction and dispersion, the reaction rate (and heat generation) can be limited by internal and external diffusion in the radial direction. To capture this effect, we formulated a detailed washcoat diffusion model.

### 7.1 Detailed Washcoat Diffusion Model

The monolith channel is divided into two phases - fluid phase (flow channel) and solid phase (lumping both catalytic washcoat and substrate wall). The feed gas flows axially through the monolith channel while mass and heat are transported in both axial and radial directions by convection and diffusion. The model can be applied to the case of multiple species and reactions, but here we consider only one limiting reactant with one reaction since the focus is to study the reactor's transient behavior instead of kinetic models.

The model equations are derived from species and energy balances in the two phases. The species balance in the fluid phase is given by

$$\frac{\partial C_f}{\partial t} + \langle u \rangle \frac{\partial C_f}{\partial x} = D_f \frac{\partial^2 C_f}{\partial x^2} - \frac{k_{me}}{R_\Omega} (C_f - C_s), 0 < x < L, t > 0. \quad (7.1)$$

Here,  $C_f$  represents the the cup-mixing concentration in the fluid phase ;  $C_s$  is the concentration at the fluid-solid interphase (i.e.,  $C_s = C_{wc}|_{y=0}$ );  $\langle u \rangle$  is the average fluid velocity;  $D_f$  is the molecular diffusivity of the reactant in the fluid phase;  $L$  is the length of the reactor;  $R_\Omega$  is the hydraulic radius of the flow channel (half of the geometric radius for a circular channel);  $k_{me}$  is the external mass transfer coefficient. The species balance in the washcoat is given by

$$\epsilon_{wc} \frac{\partial C_{wc}}{\partial t} = D_{wc} \frac{\partial^2 C_{wc}}{\partial y^2} - R(C_{wc}, T_s), \quad 0 < y < \delta_{wc}, t > 0. \quad (7.2)$$

Here,  $C_{wc}$  and  $D_{wc}$  are the concentration and effective diffusivity in the washcoat, respectively;  $R(C_{wc}, T_s)$  is the reaction rate per unit volume of the washcoat;  $\delta_{wc}$  and  $\epsilon_{wc}$  are the thickness and the porosity of the washcoat, respectively. The initial and boundary conditions for the species balances are given by

$$C_f = C_f^0, C_{wc} = C_{wc}^0 \text{ at } t = 0, \quad (7.3a)$$

$$D_f \frac{\partial C_f}{\partial x} = \langle u \rangle (C_f - C_f^{in}) \text{ at } x = 0, \quad \frac{\partial C_f}{\partial x} = 0 \text{ at } x = L, \quad (7.3b)$$

$$k_{me} (C_f - C_s) = -D_{wc} \frac{\partial C_{wc}}{\partial y} \text{ at } y = 0, \quad \frac{\partial C_{wc}}{\partial y} = 0 \text{ at } y = \delta_{wc}.$$

The energy balance in the fluid phase is given by

$$\rho_f C_p \left( \frac{\partial T_f}{\partial t} + \langle u \rangle \frac{\partial T_f}{\partial x} \right) = -\frac{h}{R_\Omega} (T_f - T_s). \quad (7.4)$$

Since both the washcoat and the substrate wall have large thermal conductivities and small thicknesses, in the energy balance we assume the temperature is radially uniform in the whole solid phase including both the washcoat and the substrate wall. The parameters used for the solid phase can be defined as an effective or averaged

value for the two layers,

$$\delta_s = \delta_w + \delta_{wc}, \quad \delta_s k_s = \delta_w k_w + \delta_{wc} k_{wc},$$

$$\rho_s C_p \delta_s = \rho_{wc} C_p \delta_{wc} + \rho_w C_p \delta_w,$$

Thus, the energy balance in the solid phase is

$$\rho_s C_p \frac{\partial T_s}{\partial t} = k_s \frac{\partial^2 T_s}{\partial x^2} + \frac{h}{\delta_s} (T_f - T_s) + \frac{1}{\delta_s} (-\Delta H) \int_0^{\delta_{wc}} R(C_{wc}, T_s) dy. \quad (7.5)$$

Here,  $T$  represents temperature,  $\rho$  and  $C_p$  are density and specific heat capacity,  $k$  is thermal conductivity and  $\delta$  is thickness. The subscript  $f$  stands for the fluid phase;  $wc$  and  $w$  represent the washcoat and substrate wall, respectively;  $s$  represents the combined solid phase including both the washcoat and the substrate.  $\Delta H$  is the heat of reaction and  $h$  is the fluid-solid heat transfer coefficient. The initial and boundary conditions for the energy balances are given by

$$T_f = T_f^0, \quad T_s = T_s^0 \quad \text{at } t = 0, \quad (7.6a)$$

$$T_f = T_f^{in}, \quad \frac{\partial T_s}{\partial x} = 0 \quad \text{at } x = 0, \quad \frac{\partial T_s}{\partial x} = 0 \quad \text{at } x = L. \quad (7.6b)$$

Theoretically, the initial concentrations and temperatures ( $C_f^0$ ,  $C_{wc}^0$ ,  $T_f^0$  and  $T_s^0$ ) are functions of  $x$ , and they will have influences on the reactor's light-off and transient behavior. However, this infinite-dimensional problem is beyond the scope of this work, so we assume a uniform initial profile ( $C_f^0$ ,  $C_{wc}^0$ ,  $T_f^0$  and  $T_s^0$  become constants). Similarly, in this work we study mainly the creeping reaction zones responding to a step change, thus the inlet conditions ( $C_f^{in}$  and  $T_f^{in}$ ) are considered step functions instead of arbitrary functions of  $t$ .

In this model, the axial molecular diffusion in the washcoat is neglected since the

Table 7.1: Characteristic scales

<i>Scale</i>	<i>Definition</i>	<i>Description</i>
Time	$\tau = L/\langle u \rangle$	Space time (s)
Length	$L$	Reactor length (m)
Transverse length	$\delta_{wc}$	Washcoat thickness (m)
Concentration	$C_f^{in}$	Inlet concentration (mol/m <sup>3</sup> )
Temperature	$T_f^{in}$	Inlet temperature (K)

mass Péclet number in the washcoat is significantly larger than the one in the fluid phase. Similarly, the axial heat conduction in the fluid phase is neglected due to large fluid phase heat Péclet number.

## 7.2 Dimensionless Groups

To facilitate the development of criteria and correlations for creeping reaction zones, a dimensional analysis is conducted. We define characteristic scales as shown in Table 7.1, then non-dimensionalized the variables, operators and inlet conditions accordingly,

$$\hat{t} = \frac{t}{\tau}, z = \frac{x}{L}, \xi = \frac{y}{\delta_{wc}}, \chi = \frac{C_f^{in} - C}{C_f^{in}}, \theta = \gamma \frac{T - T_f^{in}}{T_f^{in}}.$$

The concentrations are non-dimensionalized as conversions. The dimensionless temperature is multiplied by the dimensionless activation energy  $\gamma$ . Substituting the dimensionless variables in the equations, some important dimensionless groups appear in the governing equations and initial/boundary conditions. The model equations may be expressed as

$$\frac{\partial \chi_f}{\partial \hat{t}} + \frac{\partial \chi_f}{\partial z} = \frac{1}{Pe_m} \frac{\partial^2 \chi_f}{\partial z^2} - \frac{Sh_\Omega}{P_m} (\chi_f - \chi_s), \quad (7.7)$$

$$\epsilon \frac{\partial \chi_{wc}}{\partial \hat{t}} = \frac{1}{\Lambda P_m} \frac{\partial^2 \chi_{wc}}{\partial \xi^2} + Da \hat{R}(\chi_{wc}, \theta_s) \exp\left(\frac{\gamma \theta_s}{\theta_s + \gamma}\right),$$

$$\frac{\partial \theta_f}{\partial \hat{t}} + \frac{\partial \theta_f}{\partial z} = -\frac{Nu_\Omega}{P_h} (\theta_f - \theta_s), \quad (7.8)$$

$$\sigma \frac{\partial \theta_s}{\partial \hat{t}} = \frac{1}{Pe_h} \frac{\partial^2 \theta_s}{\partial z^2} + \frac{Nu_\Omega}{P_h} (\theta_f - \theta_s) + BDa \exp\left(\frac{\gamma \theta_s}{\theta_s + \gamma}\right) \int_0^1 \hat{R}(\chi_{wc}, \theta_s) d\xi, \quad (7.9)$$

with initial and boundary conditions,

$$\chi_f = \chi_f^0, \chi_{wc} = \chi_{wc}^0, \theta_f = \theta_f^0, \theta_s = \theta_s^0 \text{ at } \hat{t} = 0, \quad (7.10a)$$

$$\frac{1}{Pe_m} \frac{\partial \chi_f}{\partial z} = \chi_f \text{ at } z = 0, \frac{\partial \chi_f}{\partial z} = 0 \text{ at } z = 1, \quad (7.10b)$$

$$Sh_\Omega \Lambda (\chi_f - \chi_s) = -\frac{\partial \chi_{wc}}{\partial \xi} \text{ at } \xi = 0, \frac{\partial \chi_{wc}}{\partial \xi} = 0 \text{ at } \xi = 1, \quad (7.10c)$$

$$\theta_f = 0, \frac{\partial \theta_s}{\partial z} = 0 \text{ at } z = 0, \frac{\partial \theta_s}{\partial z} = 0 \text{ at } z = 1. \quad (7.10d)$$

The capacitance parameters are defined by

$$\epsilon = \epsilon_{wc} \frac{\delta_{wc}}{R_\Omega}, \sigma = \frac{\rho_s Cp_s \delta_s}{\rho_f Cp_f R_\Omega}.$$

The transverse Péclet numbers (related to molecular diffusion and heat conduction in the transverse direction) are defined by

$$P_m = \frac{\langle u \rangle R_\Omega^2}{D_f L}, P_h = \frac{\langle u \rangle R_\Omega^2}{\alpha_f L},$$

where,  $\alpha_f$  is the thermal diffusivity of the fluid defined by

$$\alpha_f = \frac{k_f}{\rho_f Cp_f}.$$

The diffusivity ratio  $\Lambda$ , which is defined as

$$\Lambda = \frac{D_f \delta_{wc}}{D_{wc} R_\Omega},$$

determines the magnitude of diffusion limitations in the washcoat. The Sherwood and Nusselt numbers are defined as

$$Sh_{\Omega} = \frac{k_{me}R_{\Omega}}{D_f}, \quad Nu_{\Omega} = \frac{hR_{\Omega}}{k_f}.$$

The axial mass and heat Péclet numbers (related to molecular diffusion and heat conduction in the axial direction) are defined by

$$Pe_m = \frac{\langle u \rangle L}{D_f}, \quad Pe_h = \frac{\langle u \rangle L k_f R_{\Omega}}{\alpha_f k_s \delta_s}.$$

The subscripts  $m$  and  $h$  represent mass and heat transfer,  $f$  and  $s$  represent the flow channel and the solid phase, respectively.

The Damköhler number is defined as

$$Da = \frac{\delta_{wc}}{R_{\Omega}} \frac{L}{\langle u \rangle} \frac{R(C_f^{in}, T_f^{in})}{C_f^{in}}.$$

The dimensionless rate expression is defined as

$$\widehat{R} = \frac{R(C_{wc}, T_f^{in})}{R(C_f^{in}, T_f^{in})}.$$

In case of a first-order reaction with rate expression of the form  $R(C, T) = A \exp\left(-\frac{E_a}{R_g T}\right) C$  (where  $E_a$  is the activation energy of the reaction and  $R_g$  is the gas constant),

$$Da = A \frac{\delta_{wc}}{R_{\Omega}} \frac{L}{u} \exp(-\gamma),$$

$$\widehat{R} = 1 - \chi_{wc},$$

where  $A$  is the pre-exponential factor in the Arrhenius equation,  $\gamma$  is the dimensionless

activation energy defined as

$$\gamma = \frac{E_a}{R_g T_f^{in}}.$$

The dimensionless adiabatic temperature rise or the Zel'dovich number  $B$  is defined as

$$B = \frac{E_a}{R_g T_f^{in}} \frac{(-\Delta H) C_f^{in}}{\rho_f C_p T_f^{in}} = \gamma \frac{\Delta T_{ad}}{T_f^{in}},$$

where  $\Delta T_{ad}$  is the adiabatic temperature rise. In this work, we assume constant transport coefficients for simplicity. To apply the criteria discussed in this work, one should evaluate the transport coefficients at the temperature of interest or use average values over a certain range of temperature.

## 7.3 Simplified Models

### 7.3.1 One-dimensional Two-phase Monolith Model

The effectiveness factor is defined as the ratio of actual overall rate of reaction over the rate evaluated at surface concentrations (Fogler, 2005). Assuming no accumulation of reactant in the washcoat, a local balance of diffusion and reaction can be obtained,

$$\frac{k_{me}}{\delta_{wc}} (C_f - C_s) = \eta R(C_s, T_s). \quad (7.11)$$

If the reaction is first-order, the effectiveness factor  $\eta$  can be obtained explicitly by solving the detailed washcoat diffusion model,

$$\eta = \frac{1}{\frac{\Phi}{\tanh \Phi} + \frac{\Phi^2}{\Lambda Sh_\Omega}}, \quad (7.12)$$

where

$$\Phi^2 = \Lambda \phi_s^2 \exp\left(\frac{\gamma \theta_s}{\theta_s + \gamma}\right), \quad \phi_s^2 = P_m Da = \frac{AR_\Omega \delta_{wc}}{D_f} \exp(-\gamma).$$

The Thiele modulus  $\phi_s^2$  determines the importance of external mass transfer compared to reaction. The first term in the denominator ( $\frac{\Phi}{\tanh \Phi}$ ) reflects the impact of internal (washcoat) diffusion, while the second term ( $\frac{\Phi^2}{\Lambda Sh_\Omega}$ ) accounts for external diffusion.

The model is then reduced to a one-dimensional two-phase model,

$$\frac{\partial \chi_f}{\partial \hat{t}} + \frac{\partial \chi_f}{\partial z} = \frac{1}{Pe_m} \frac{\partial^2 \chi_f}{\partial z^2} + \eta Da (1 - \chi_f) \exp\left(\frac{\gamma \theta_s}{\theta_s + \gamma}\right), \quad (7.13)$$

$$\frac{\partial \theta_f}{\partial \hat{t}} + \frac{\partial \theta_f}{\partial z} = -\frac{Nu_\Omega}{P_h} (\theta_f - \theta_s), \quad (7.14)$$

$$\sigma \frac{\partial \theta_s}{\partial \hat{t}} = \frac{1}{Pe_h} \frac{\partial^2 \theta_s}{\partial z^2} + \frac{Nu_\Omega}{P_h} (\theta_f - \theta_s) + \eta BDa (1 - \chi_f) \exp\left(\frac{\gamma \theta_s}{\theta_s + \gamma}\right), \quad (7.15)$$

with initial and boundary conditions,

$$\chi_f = \chi_f^0, \theta_f = \theta_f^0, \theta_s = \theta_s^0 \text{ at } \hat{t} = 0, \quad (7.16a)$$

$$\frac{1}{Pe_m} \frac{\partial \chi_f}{\partial z} = \chi_f \text{ at } z = 0, \frac{\partial \chi_f}{\partial z} = 0 \text{ at } z = 1, \quad (7.16b)$$

$$\theta_f = 0, \frac{\partial \theta_s}{\partial z} = 0 \text{ at } z = 0, \frac{\partial \theta_s}{\partial z} = 0 \text{ at } z = 1. \quad (7.16c)$$

### 7.3.2 Pseudo-homogeneous model

The one-dimensional two-phase model will approach a pseudo-homogeneous limit when  $P_m \ll 1$ ,  $P_h \ll 1$ ,  $\phi_s^2 \ll 1$ . This can be satisfied in catalytic after-treatment reactors with high cell density. In such cases, one can combine mass and heat balances in separate phases by utilizing effective Péclet number  $Pe_{eff}$  which combines the effects of axial dispersion and interphase (radial) gradient. For simplicity, we omit the subscript *eff* in the Péclet numbers.

In the pseudo-homogeneous model, the species balance is given by

$$(1 + \epsilon) \frac{\partial \chi}{\partial \hat{t}} = \frac{1}{Pe_m} \frac{\partial^2 \chi}{\partial z^2} - \frac{\partial \chi}{\partial z} + Da (1 - \chi) \exp\left(\frac{\gamma \theta}{\theta + \gamma}\right). \quad (7.17)$$

The energy balance is

$$(1 + \sigma) \frac{\partial \theta}{\partial \hat{t}} = \frac{1}{Pe_h} \frac{\partial^2 \theta}{\partial z^2} - \frac{\partial \theta}{\partial z} + BDa(1 - \chi) \exp\left(\frac{\gamma \theta}{\theta + \gamma}\right). \quad (7.18)$$

The initial and boundary conditions are

$$\chi = \chi^0, T = T^0 \text{ at } \hat{t} = 0, \quad (7.19a)$$

$$\frac{1}{Pe_m} \frac{\partial \chi}{\partial z} - \chi = 0 \text{ at } z = 0, \frac{\partial \chi}{\partial z} = 0 \text{ at } z = 1, \quad (7.19b)$$

$$\frac{1}{Pe_h} \frac{\partial \theta}{\partial z} - \theta = 0 \text{ at } z = 0, \frac{\partial \theta}{\partial z} = 0 \text{ at } z = 1. \quad (7.19c)$$

In this work, the calculations are conducted using the one-dimensional pseudo-homogeneous model. The model can well capture the reactor behaviors in the kinetics controlled regime and the trends are similar to what has been reported in packed-bed reactors.

# Chapter 8

## Analysis of Upstream Creeping Reaction Zones in Catalytic Monolith Reactors

### 8.1 Transient Behavior of Monolith Reactors

As a result of high precious metal loading, the reaction zone in an exhaust after-treatment reactors are very narrow once it is ignited. Similar to what has been observed in packed-bed reactors (Wicke and Vortmeyer, 1959), this narrow reaction zone reactors can remain stationary or creep in either upstream or downstream direction maintaining a constant shape of the profiles under different conditions. Shown in Fig. 8.1 are examples of a upstream creeping reaction zone at a low gas velocity and a downstream creeping reaction zone at a higher gas velocity. In this example, the inlet temperature is 450 K and the adiabatic temperature rise is 285 K, which corresponds to the oxidation of  $\sim 3\%$  CO or  $\sim 4500$  ppm  $C_3H_6$ . The parameters used for calculations are adapted from a typical 600 cpsi ceramic TWC (Heck et al., 2009; Gundlapally and Balakotaiah, 2013; Kumar et al., 2014), the transport properties are evaluated at 450 K (Table 8.1), where the molecular diffusivity is calculated for CO.

After a fast transient, a steadily creeping reaction zone is established. The conversion profiles are rather straightforward, in Fig. 8.1(a) a back-end ignition happened and the reaction zone creeps towards the inlet until the reactor reaches steady-state; in Fig. 8.1(c) the relatively high initial temperature generates a reaction zone which

Table 8.1: Parameter values

<i>Parameter</i>	<i>Value</i>	<i>Unit</i>
$\epsilon_{wc}$	0.4	
$\delta_{wc}$	30	$\mu\text{m}$
$\delta_s$	80.8	$\mu\text{m}$
$R_\Omega$	220	$\mu\text{m}$
$L$	0.076	m
$D_f$	$4.25 \times 10^{-5}$	$\text{m}^2 \cdot \text{s}^{-1}$
$\rho_f$	0.784	$\text{kg} \cdot \text{m}^{-3}$
$Cp_f$	1020	$\text{J} \cdot \text{kg}^{-1} \cdot \text{K}^{-1}$
$k_s$	2	$\text{W} \cdot \text{m}^{-1} \cdot \text{K}^{-1}$
$\rho_s Cp_s$	$1.8 \times 10^6$	$\text{J} \cdot \text{m}^{-3} \cdot \text{K}^{-1}$
$A$	$10^{12}$	$\text{s}^{-1}$
$E_a/R_g$	12000	K

is slowly swept out of the reactor and a quenched steady-state is reached. On the other hand, the temperature profiles show two traveling temperature fronts. One of the temperature fronts is caused by reaction heat and follows the concentration front. The other wider and faster downstream traveling front is caused by convective heat transport, which is not the focus of this work since no reaction is involved. In Fig. 8.1(b), the temperature rise in the reactor is smaller than the adiabatic temperature rise until the reaction zone creeps to the inlet when a downstream traveling temperature front is generated and brings the temperature to the adiabatic limit. In Fig. 8.1(d), after a super-adiabatic hotspot is generated, both temperature fronts travels downstream with the heating front faster than the reaction front expanding the hot zone till it exits the reactor. This counter-intuitive phenomenon, where a sudden drop of inlet temperature (from  $T^0$  to  $T^{in}$ ) can create a super-adiabatic temperature rise, is commonly referred to as the *Wrong-way Behavior* (Mehta et al., 1981).

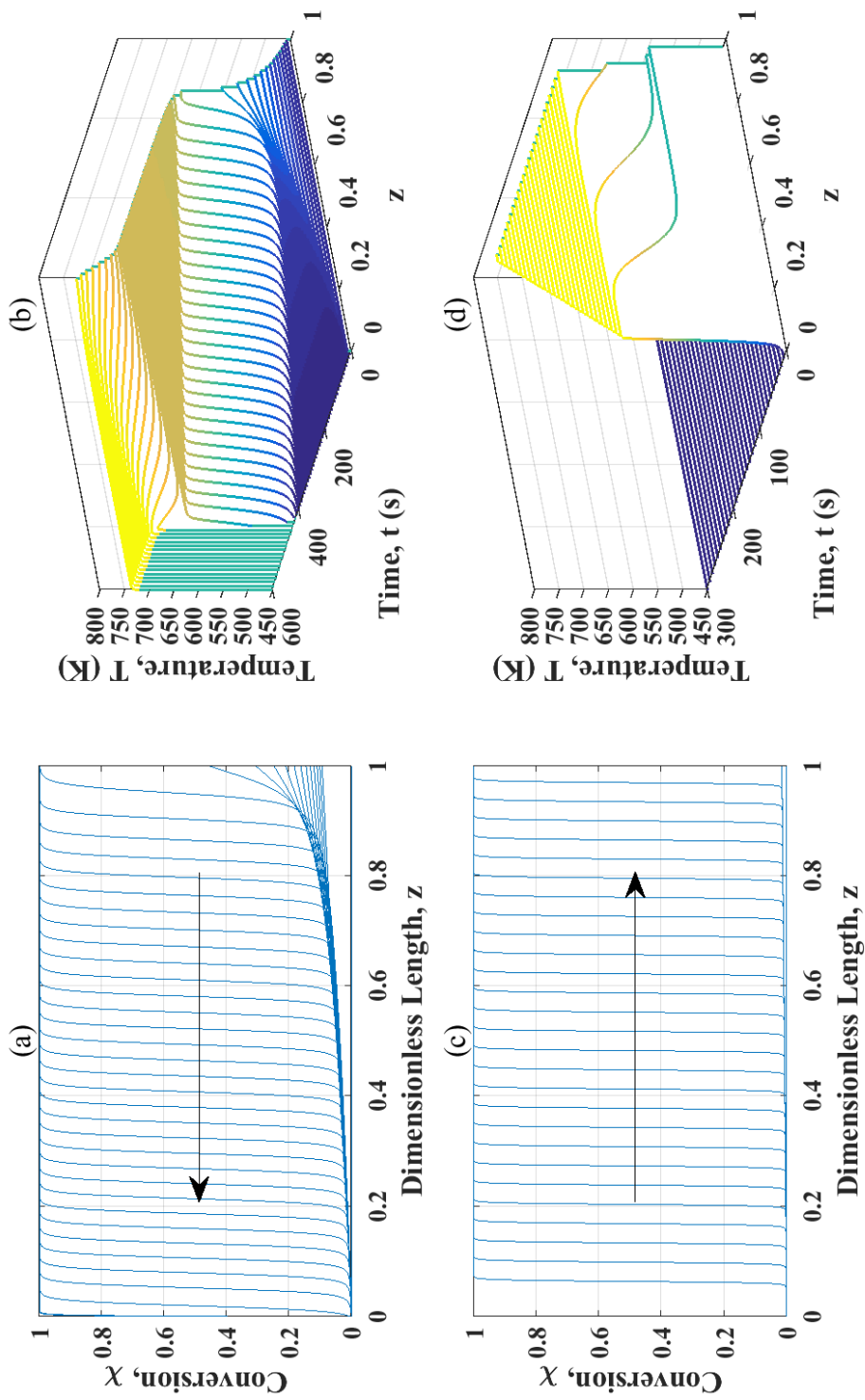


Figure 8.1: Snapshots of transient conversion (a,c) and temperature (b,d) profiles after a step change in inlet temperature. Snapshots are taken every 10 s. [ $\langle u \rangle = 0.5 \text{ m/s}$  in (a) and (b),  $\langle u \rangle = 2 \text{ m/s}$  in (c) and (d)]

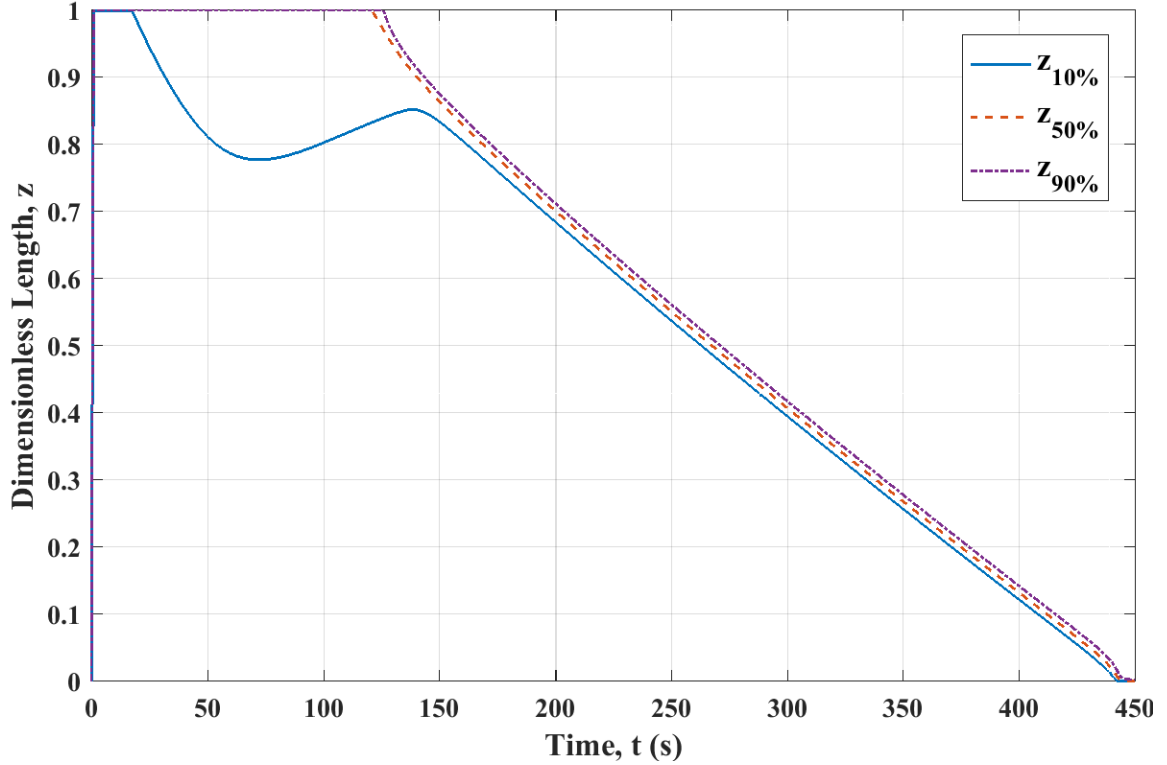


Figure 8.2: Dimensionless lengths to achieve 10%, 50% and 90% conversions as a function of time. ( $\Delta T_{ad} = 285$  K,  $T^{in} = 450$  K,  $\langle u \rangle = 0.5$  m/s)

In Fig. 8.1, until the reaction zone reaches the inlet or exit, a nearly constant creep velocity is maintained. Shown in Fig. 8.2 are dimensionless lengths to achieve 10%, 50% and 90% conversions in the case of  $\Delta T_{ad} = 285$  K,  $T^{in} = 450$  K,  $u = 0.5$  m/s. We can observe that while the reaction zone is steadily creeping, the three curves are very close indicating the reaction zone is narrow; the curves are parallel indicating the shape of the concentration front is unchanged; the curves are almost linear indicating a constant creep velocity. Thus through linearly fitting this region with respect to time and taking the average slope of the three curves, a creep velocity ( $v$ ) can be obtained for every gas velocity at a given inlet temperature as shown in Fig. 8.3(a), or similarly for every inlet temperature at a given gas velocity as shown in Fig. 8.3(b). The creep velocity is negative when the reaction zone creeps upstream. When  $u$  is too small, (leading to small  $Pe_m$  and  $Pe_h$ ) conduction will dominate the process resulting in a wide reaction zone with a changing shape.

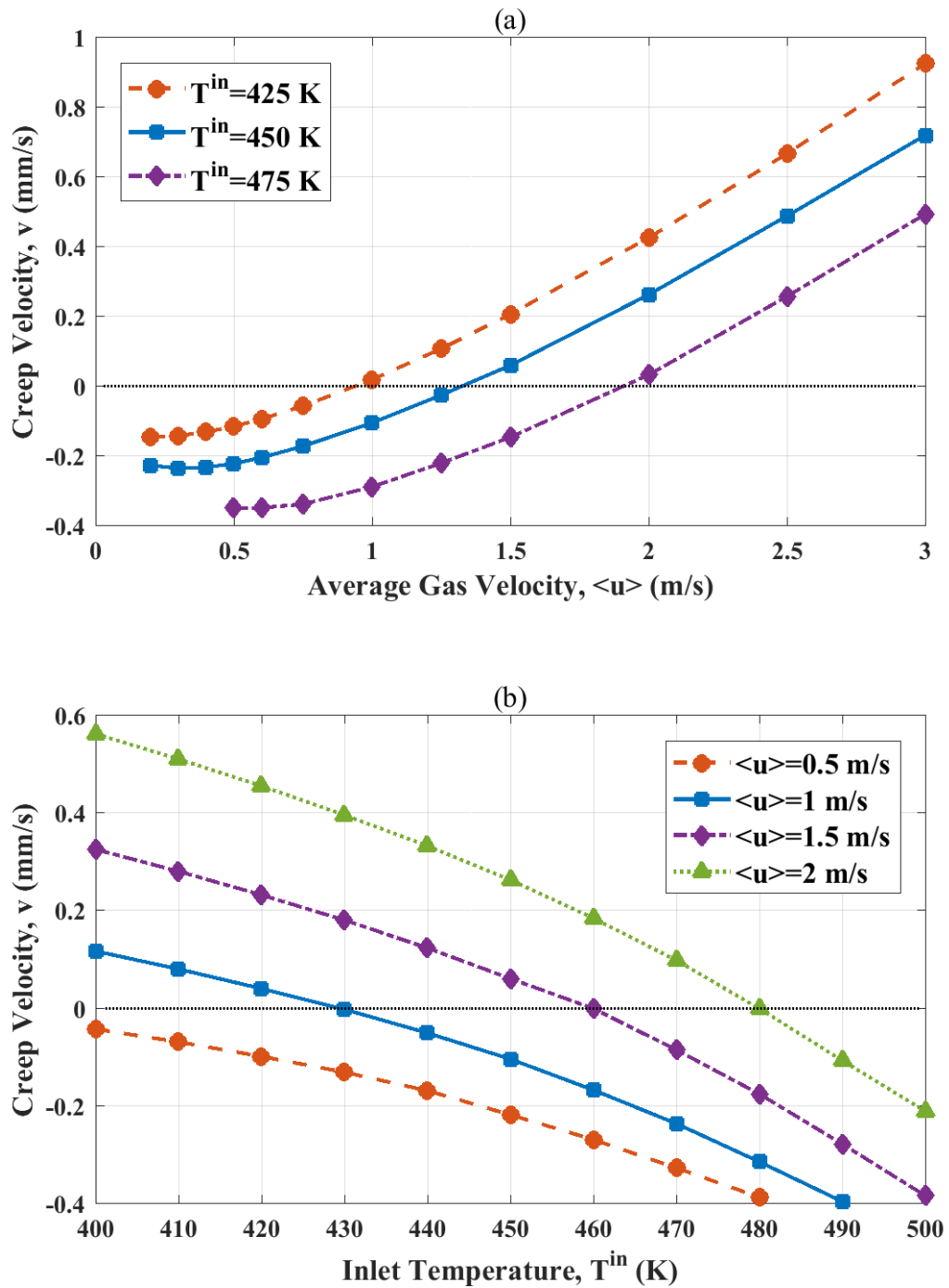


Figure 8.3: Creep velocity as a function of (a) the gas velocity and (b) the inlet temperature.  $[\Delta T_{ad} = 285 \text{ K}]$

## 8.2 Parametric Studies on Creep Velocity

In this section, we study the effects of some important reactor design parameters and operating conditions on the creep velocity. This can provide qualitative insight as well as quantitative data for the development of criteria for upstream creeping reaction zones.

### 8.2.1 Adiabatic Temperature Rise ( $\Delta T_{ad}$ )

Sufficient heat generation is the pre-requisite for upstream creeping reaction zones. The larger thermal effects are, the more heat can be conducted upstream enabling an upstream creeping reaction zone. Shown in Fig. 8.4 are creep velocity as a function of the gas velocity and inlet temperature with different adiabatic temperature rise. It is clear that thermal effects have a very strong impact on the creep velocity. A small variation (17%) in  $\Delta T_{ad}$  significantly changes the crossing point and the values of the creep velocity. Thermal effects also influence the shape of the curves. In Fig. 8.4(a), larger  $\Delta T_{ad}$  makes the non-monotonic trend more pronounced and also reduced the asymptotic slope of  $v$  vs.  $\langle u \rangle$  for large  $\langle u \rangle$ .

### 8.2.2 Solid Thermal Conductivity ( $k_s$ )

Since axial heat conduction is the main transport process that enables upstream creeping reaction zones, the solid conductivity naturally has a strong impact on the creep velocity. Shown in Fig. 8.5 are creep velocity as a function of the gas velocity and inlet temperature with different solid conductivity. Solid conductivity changes the crossing point (although as strong as the impact of thermal effects), but the shape of different curves are almost the same.

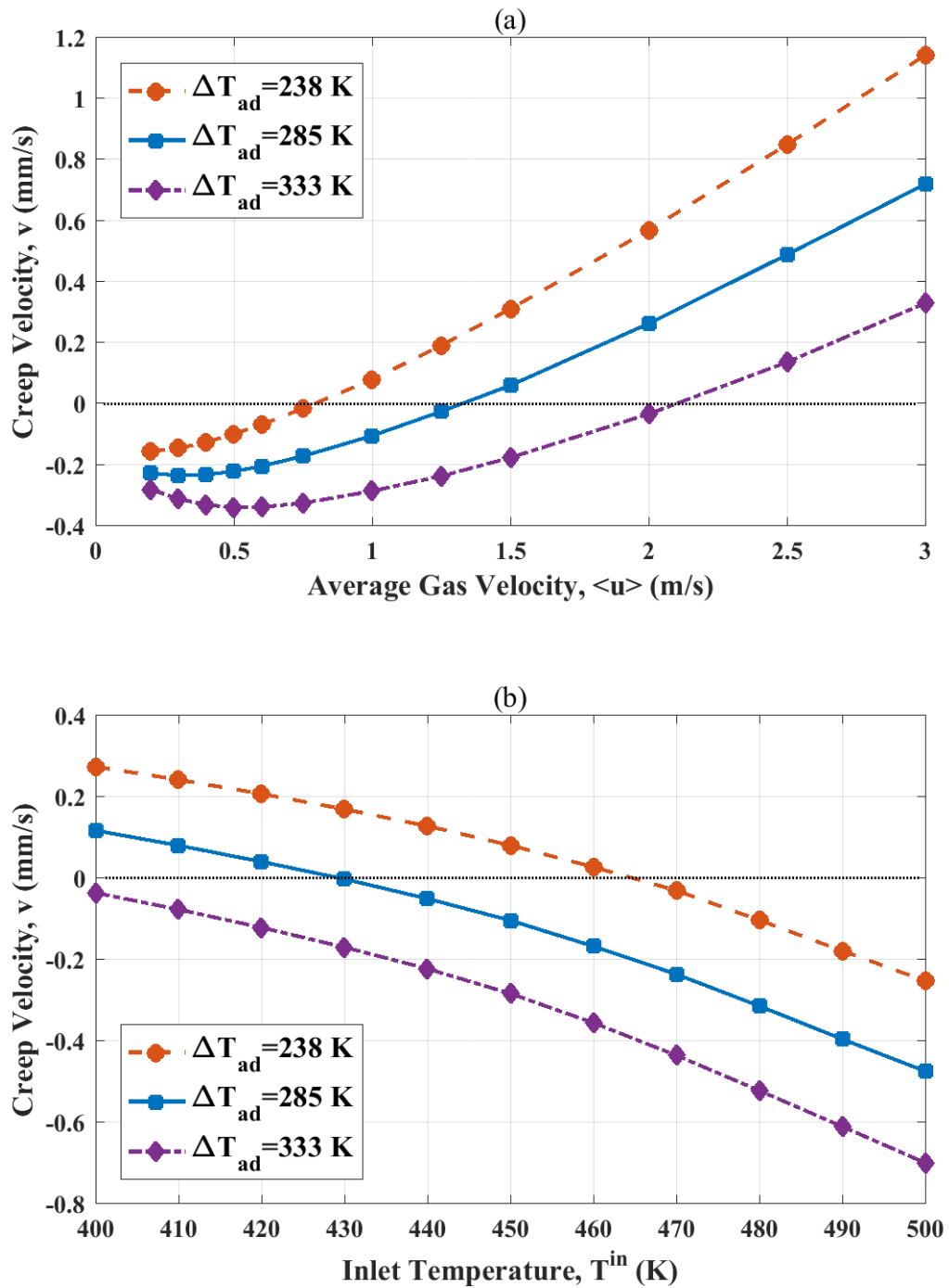


Figure 8.4: Creep velocity as a function of (a) the gas velocity and (b) the inlet temperature with different adiabatic temperature rise. [ $T^{in} = 450$  K in (a),  $\langle u \rangle = 1$  m/s in (b)]

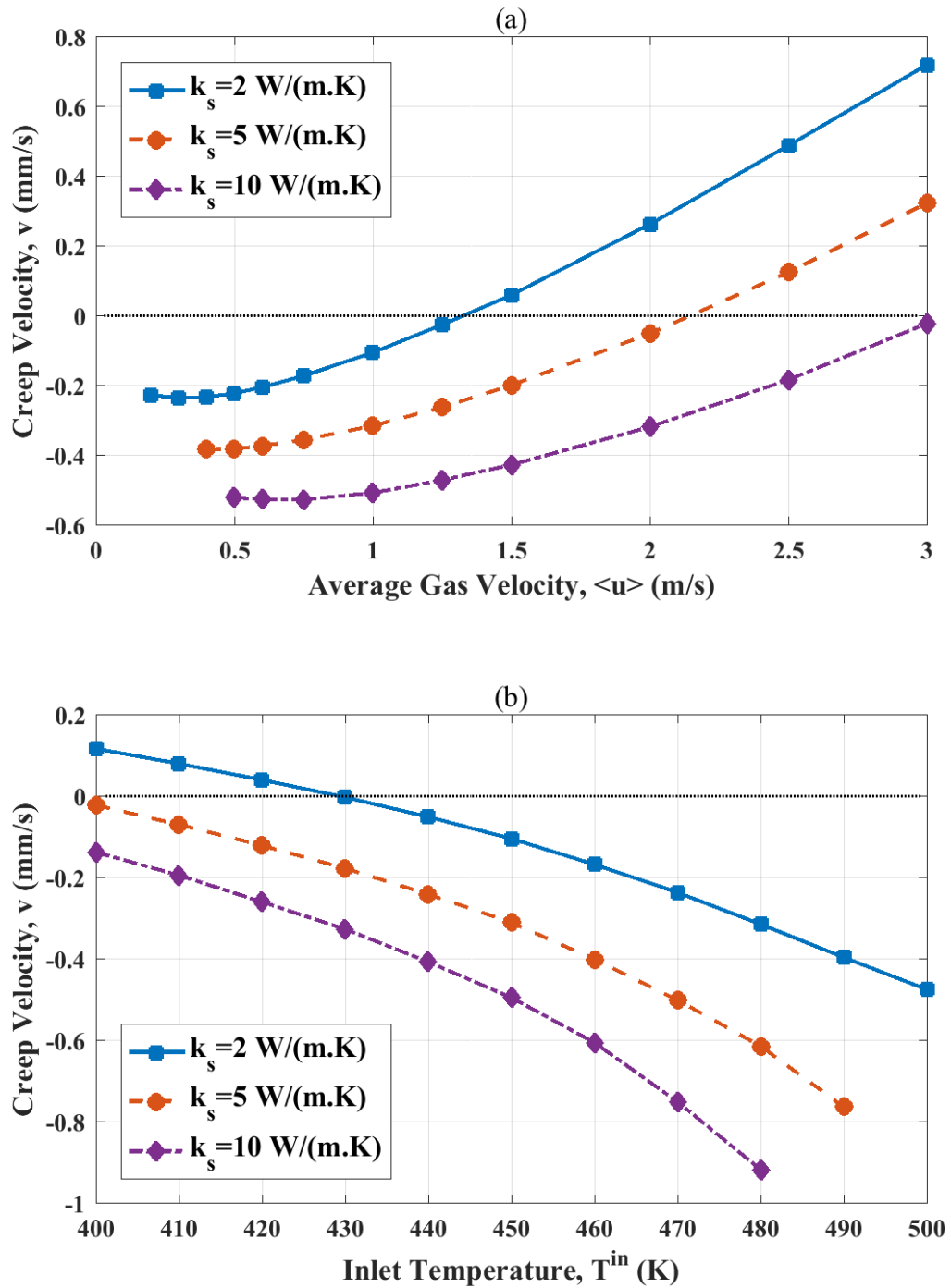


Figure 8.5: Creep velocity as a function of (a) the gas velocity and (b) the inlet temperature with different solid thermal conductivity. [ $\Delta T_{ad} = 285$  K,  $T^{in} = 450$  K in (a),  $\langle u \rangle = 1$  m/s in (b)]

### 8.2.3 Solid Heat Capacity ( $\rho_s C p_s$ )

Shown in Fig. 8.6 are creep velocity as a function of the gas velocity and inlet temperature with different volumetric heat capacity of the solid phase ( $\rho_s C p_s$ ). The curves cross zero at the same point. As will be shown later, this point is related to the steady-state performance, so it is not influenced by the heat capacity which only appears in the transient term. In the figures, we can observe that heat capacity influences the creep velocity as a constant multiplier. A lower heat capacity can accelerate upstream creeping reaction zone, which is desirable. However, it also make the reactor less robust to excursions since it also accelerates downstream extinction wave.

### 8.2.4 Substrate Material

While the physical properties of the washcoat usually remain unchanged, different substrate material with different conductivity, heat capacity and thickness can be used. The effect of substrate material on the creep velocity is a combination of the individual cases. Here as an example, we show the comparison of a ceramic monolith reactor (as used in other sections) and a metallic one (parameters shown in Table 8.2) with the same cell density of 600 cpsi (Heck et al., 2009; Gundlapally and Balakotaiah, 2013). As shown in Fig. 8.7, the higher conductivity significantly promoted upstream creeping phenomenon. Although metallic substrates has a higher volumetric heat capacity than ceramic ones, the smaller thickness leads to a smaller thermal capacitance ratio  $\sigma$  (546 comparing to 840 in the ceramic case) which also accelerates upstream creeping.

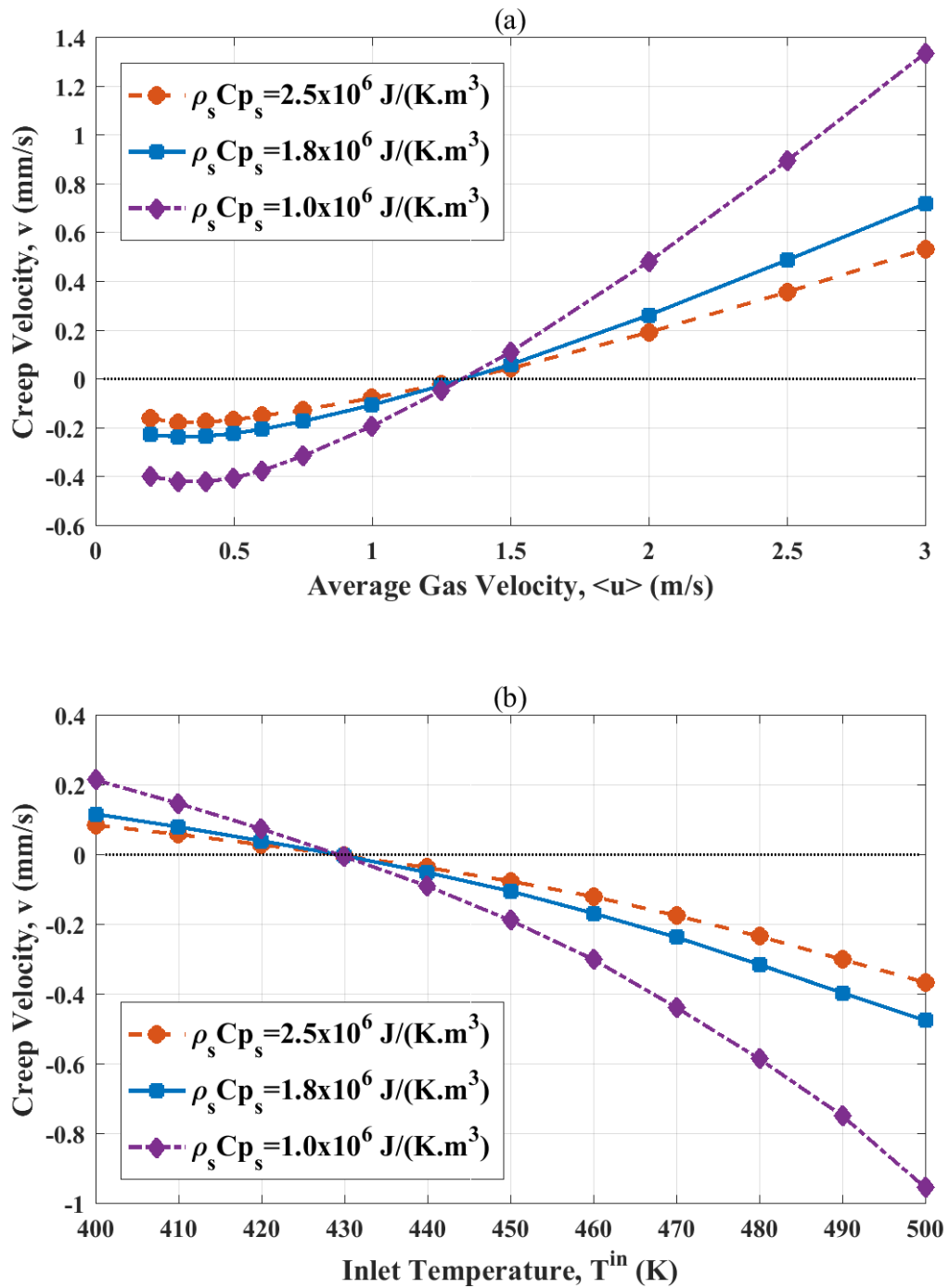


Figure 8.6: Creep velocity as a function of (a) the gas velocity and (b) the inlet temperature with different solid heat capacity. [ $\Delta T_{ad} = 285 \text{ K}$ ,  $T^{\text{in}} = 450 \text{ K}$  in (a),  $\langle u \rangle = 1 \text{ m/s}$  in (b)]

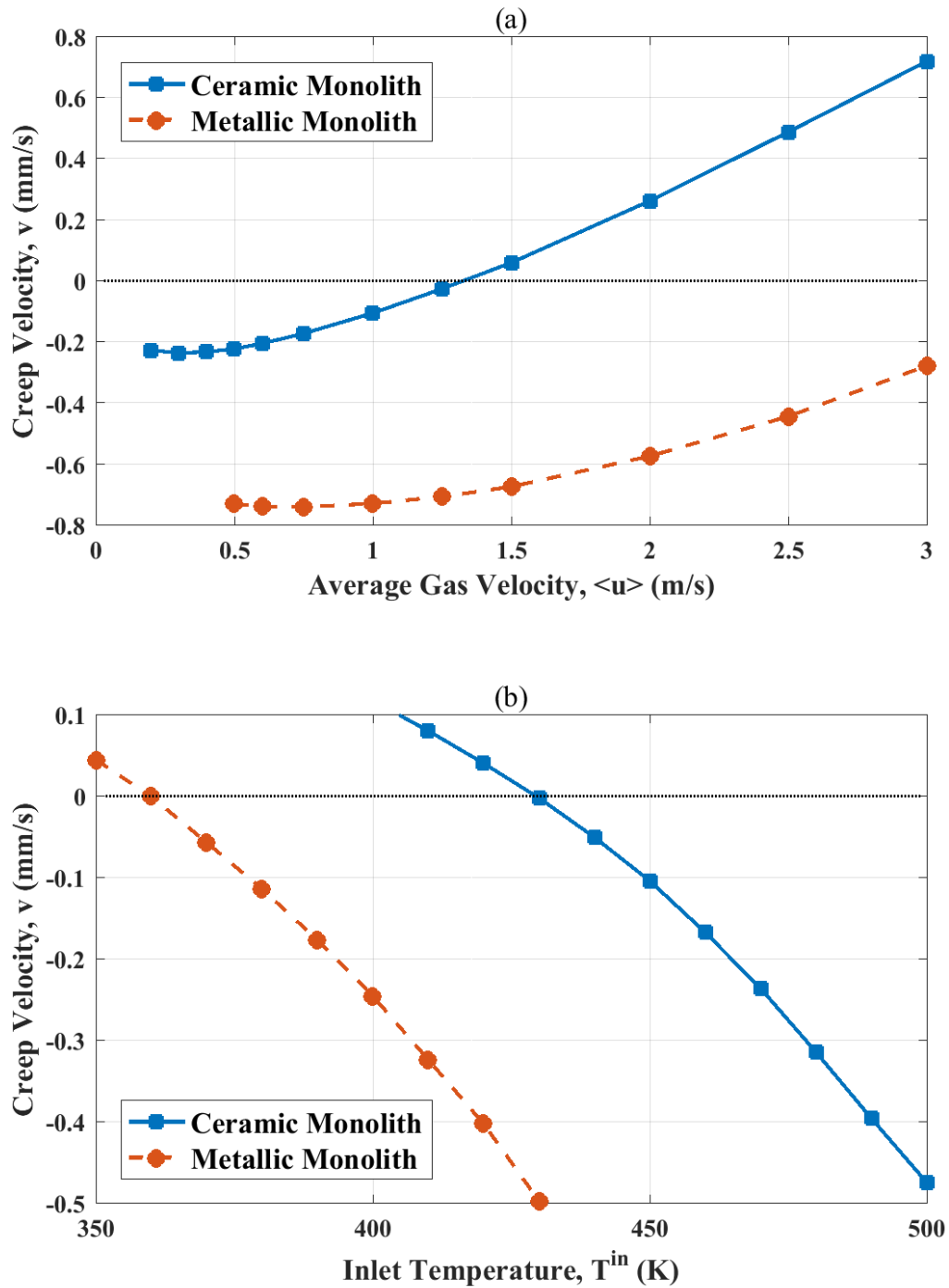


Figure 8.7: Creep velocity as a function of (a) the gas velocity and (b) the inlet temperature with different substrate materials. [ $\Delta T_{ad} = 285$  K,  $T^{in} = 450$  K in (a),  $\langle u \rangle = 1$  m/s in (b)]

Table 8.2: Metallic monolith parameters

<i>Parameter</i>	<i>Value</i>	<i>Unit</i>
$\epsilon_{wc}$	0.4	
$\delta_{wc}$	30	$\mu\text{m}$
$\delta_s$	55.4	$\mu\text{m}$
$R_\Omega$	232	$\mu\text{m}$
$L$	0.076	m
$k_s$	24	$\text{W} \cdot \text{m}^{-1} \cdot \text{K}^{-1}$
$\rho_s C p_s$	$2.4 \times 10^6$	$\text{J} \cdot \text{m}^{-3} \cdot \text{K}^{-1}$

### 8.2.5 Reactor Length

Since the creeping reaction zone phenomena are caused by local balance of convection and axial heat conduction, the total length of the reactor should not strongly influence the creep velocity. In Fig. 8.8, doubling or halving the reactor length only slightly changes the creep velocity, which confirms the analysis. This suggests that reactor length should not appear in the analytical criteria as well as correlations for creep velocity.

### 8.2.6 Nonlinear Kinetics

Langmuir-Hinshelwood mechanism and Voltz kinetics are widely accepted as global kinetic models for  $CO$  oxidation on Pt and other oxidation reactions in after-treatment catalysts (Heck et al., 2009; Voltz et al., 1973). Here we take Langmuir-Hinshelwood kinetics for  $CO$  oxidation as an example, and the rate expression is

$$R = \frac{A \exp\left(-\frac{E_a}{RT}\right) C_{O_2} C_{CO}}{(1 + K_{ads} C_{CO})^2},$$

where  $K_{ads}$  is the adsorption equilibrium constant. When the concentration of  $CO$  is high, the reaction is inhibited by  $CO$  and close to negative first-order with respect to  $CO$ .

We assume that  $O_2$  is in large excess so that  $C_{O_2}$  can be treated as a constant

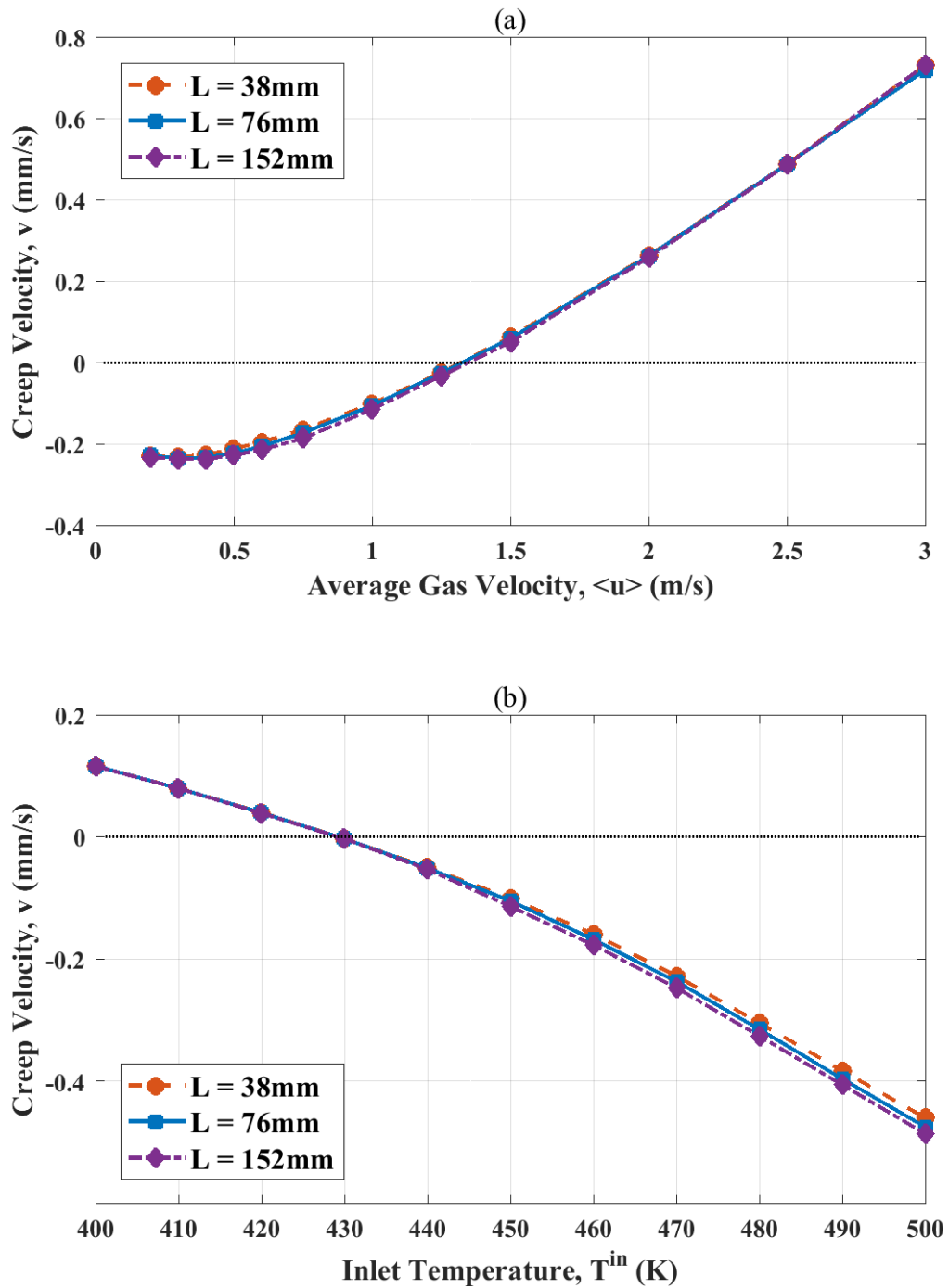


Figure 8.8: Creep velocity as a function of (a) the gas velocity and (b) the inlet temperature with different reactor length. [ $\Delta T_{ad} = 285\text{ K}$ ,  $T^{in} = 450\text{ K}$  in (a),  $\langle u \rangle = 1\text{ m/s}$  in (b)]

and can be lumped into the rate constant. The dimensionless adsorption equilibrium constant  $\kappa$  is defined as

$$\kappa = K_{ads}C_{total},$$

where  $C_{total}$  is total fluid concentration. Then, the Damköhler number for L-H kinetics can be defined as

$$Da^{LH} = \frac{AC_{O_2}}{(1 + \kappa X_{CO}^{in})^2} \frac{\delta_{wc} L}{R_{\Omega} u} \exp(-\gamma).$$

The dimensionless rate expression can be modified as

$$Da^{LH} \frac{(1 + \kappa X_{CO}^{in})^2 (1 - \chi)}{[1 + \kappa X_{CO}^{in} (1 - \chi)]^2} \exp\left(\frac{\gamma\theta}{\theta + \gamma}\right). \quad (8.1)$$

For simplicity,  $\kappa$  is assumed constant versus temperature (typically for CO oxidation  $\kappa \approx 2000$ ). For a fixed Damköhler number and CO inlet fraction ( $X_{CO}^{in} = 0.03$ ,  $\Delta T_{ad} = 285$  K), the creep velocity is calculated for different  $\kappa$  to illustrate the impact of nonlinear kinetics ( $\kappa = 0$  recovers the first-order kinetics). As shown in Fig. 8.9, the creep velocity in a reactor with L-H kinetics shows the same qualitative trend as first-order kinetics. L-H kinetics significantly promote upstream creeping reaction zones. It is because in L-H kinetics, the actual reaction rate increases as reactant is consumed leading to faster heat generation and creeping fronts.

### 8.3 Criteria for Upstream Creeping Reaction Zones

With different design parameters and under different operating conditions, the reaction zone in a reactor can creep either upstream or downstream, either till the middle or all the way to the inlet/exit. Analytical criteria for when the reaction zone creeps upstream and more importantly when it creeps all the way to the inlet can be very useful for design and control of after-treatment reactors.

In the parametric studies, we showed how different parameters affect the magni-

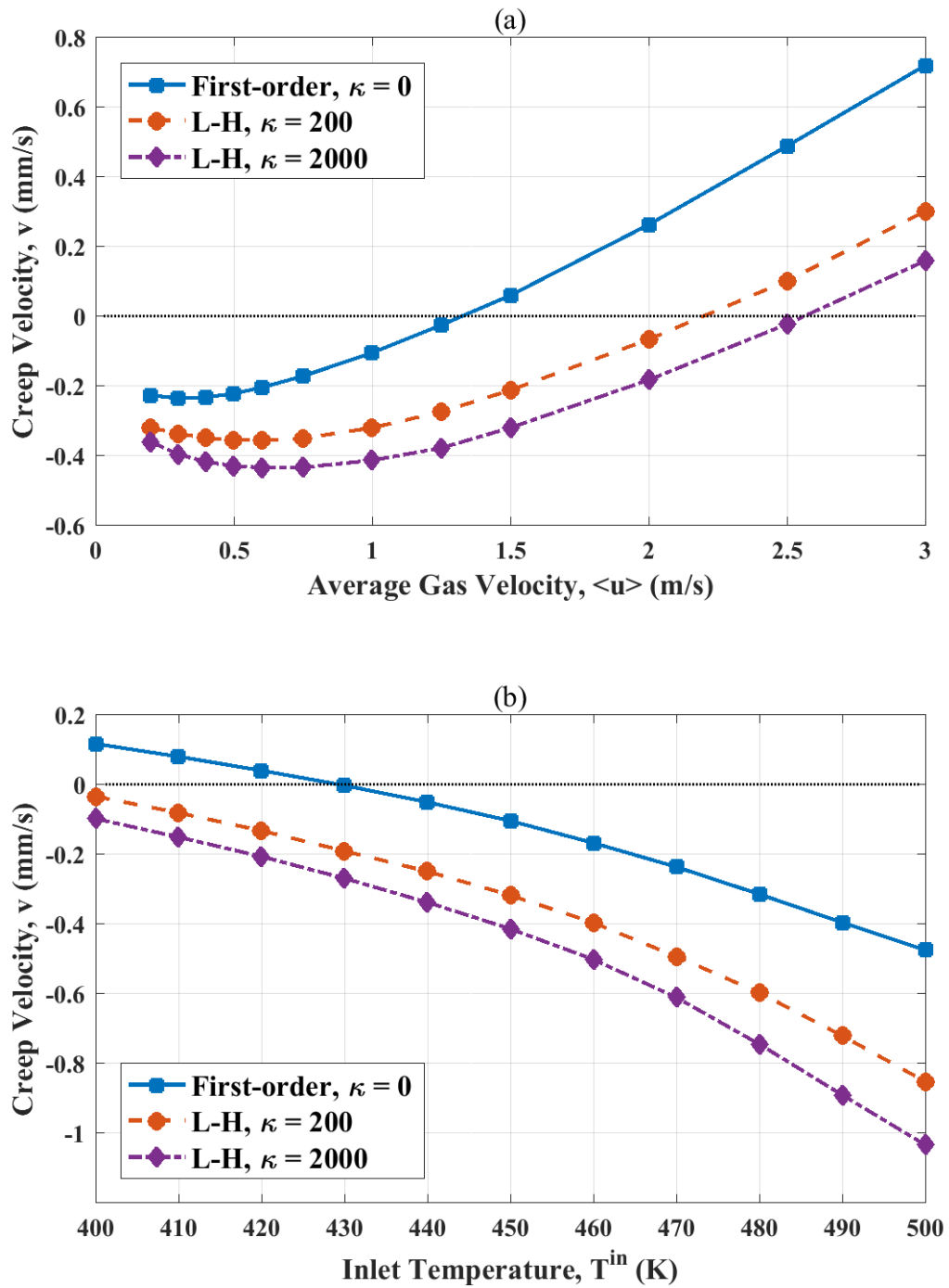


Figure 8.9: Creep velocity as a function of (a) the gas velocity and (b) the inlet temperature with different kinetics. [ $X_{CO}^{in} = 0.03$ ,  $\Delta T_{ad} = 285$  K,  $T^{in} = 450$  K in (a),  $\langle u \rangle = 1$  m/s in (b)]

tude of creep velocity and the critical point where the creep direction changes. There is another critical point, crossing which the reaction zone creeps all the way to the inlet (in this work, we define "all the way to the inlet" as the case when 50% conversion is achieved at 5% of the reactor length).

As an example, we show these critical points in terms of inlet temperature ( $T_{up}$  and  $T_{atw}$ ), assuming other parameters are fixed. When  $T^{in} < T_{up}$ , there can only be a downstream creeping reaction zone; when  $T^{in} > T_{atw}$ , the reaction zone creeps upstream all the way to the inlet. When  $T_{up} < T^{in} < T_{atw}$ , the reaction zone can creep either upstream or downstream depending on the initial temperature. If the initial temperature is relatively low, a reaction zone is established near the exit, creeps upstream and stop in the middle of the reactor. If the initial temperature is high, the reaction zone creeps downstream from the inlet. Thus, in this region we treat the creep velocity as zero.

Although the creeping reaction zone is a dynamic behavior, it is directly related to the steady-states of the reactor. After a reaction zone is established near the exit in a back-end ignition, it is the steady-state profile that determines that the reaction zone will be stationary, creep upstream and stop in the middle or creep all the way to the inlet. In Fig. 8.10, we relate the critical temperatures to the steady-state features in the case of (a) multiple steady-states and (b) unique steady-states. In Fig. 8.10(a), the creep velocity plot is the same as the first curve in Fig. 8.4(b) with more details near the crossing showing the two critical temperatures ( $T_{up} = 461.9$  K,  $T_{atw} = 466.9$  K). When there are multiple steady-states, the creep direction changes exactly at the extinction point ( $T_{up} = T_{ext}$ ). This is expected since the extinction temperature  $T_{ext}$  is the lowest temperature that a high conversion can be achieved. At any  $T^{in} < T_{ext}$ , there's only a quenched steady-state and the reaction zone can only creep downstream until it finally exits the reactor. When there is only a unique steady-state, the creep direction changes exactly at the inflection point ( $T_{up} = 495.0$  K) and

a much higher inlet temperature is needed for the front to creep all the way to the inlet ( $T_{atw} = 547.2 \text{ K}$ ).

For the case of  $\Delta T_{ad} = 238 \text{ K}$ , the critical points are calculated as shown in Fig. 8.11. The bifurcation set (ignition/extinction locus) is also shown in the figure indicating the ignition/extinction temperature (or velocity) as well as the hysteresis point (the intersection of ignition and extinction loci). In the region of multiplicity (to the left of the hysteresis point), the critical temperatures are very close and overlap with the extinction temperature ( $T_{atw} \approx T_{up} = T_{ext}$ ), thus for practical purposes there is no need to distinguish between the two critical temperatures and one criterion is sufficient. However, the two critical temperatures start to diverge near the hysteresis point where  $T_{atw}$  follows the trend of the extinction locus and  $T_{up}$  continues the ignition locus. Therefore, the criteria for  $T_{atw}$  and  $T_{up}$  are essentially approximations for the bifurcation set.

Many analytical formulae are derived for the ignition and extinction loci in the literature. Hlavacek and Hofmann proposed a sufficient condition for unique solution for large  $Pe_h$  which also serves as an approximation for the extinction locus, (Hlavacek and Hofmann, 1970)

$$\frac{Da}{Pe_h} e^B \leq \frac{1}{4}. \quad (8.2)$$

Although Eq. 8.2 usually predicts overly conservative results lacking quantitative accuracy, it provides an inspiring function form relating the important dimensionless groups ( $Da$  for reaction,  $e^B$  for heat generation,  $Pe_h$  for convection and conduction). Basing on the function form in Eq. 8.2, the extinction locus is fitted numerically to give,

$$\frac{Da}{Pe_h} e^{0.4B+1.8} = 1. \quad (8.3)$$

A good approximation for the ignition locus for large  $Pe_h$  is  $B Da = 1$ , or more

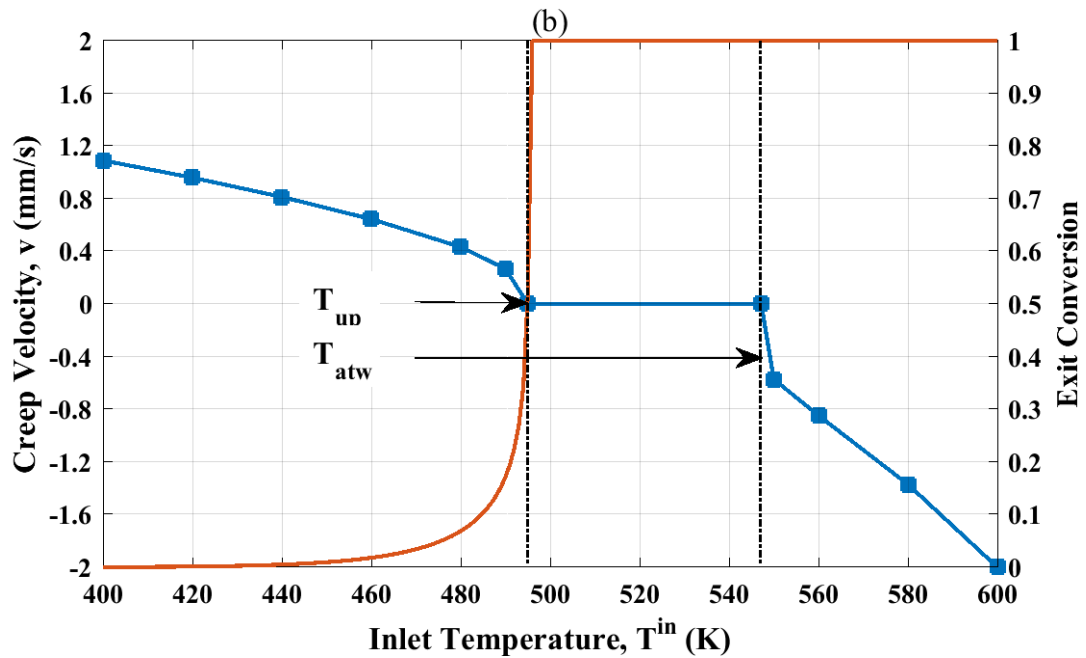
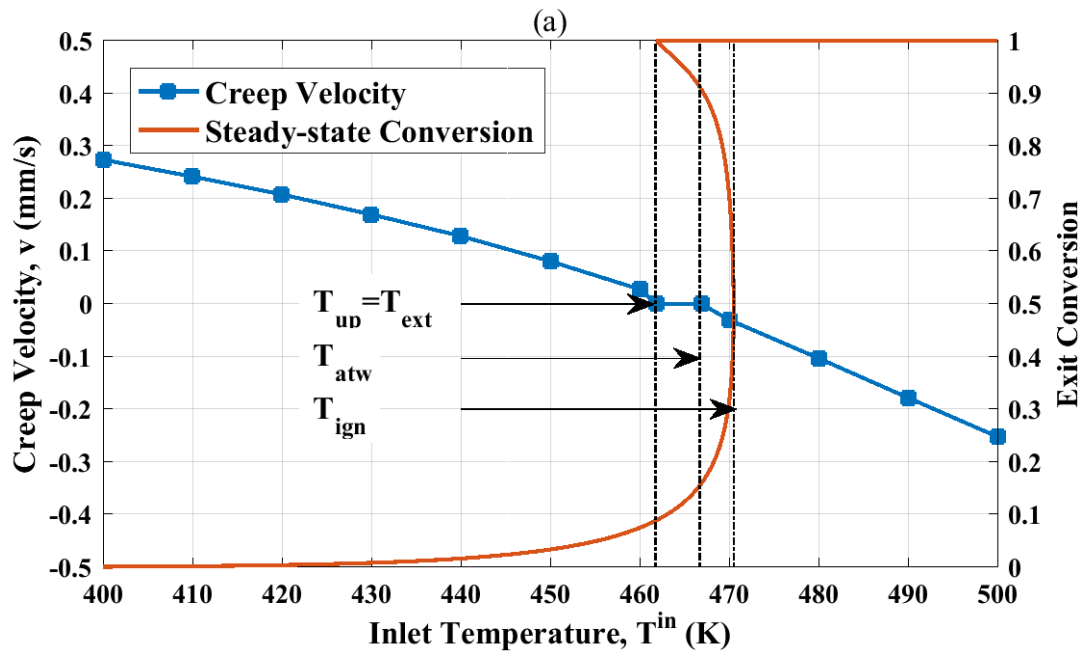


Figure 8.10: Creep velocity and steady-state conversion as a function of the inlet temperature. [ $\Delta T_{ad} = 238 \text{ K}$ ,  $\langle u \rangle = 1 \text{ m/s}$  in (a),  $\langle u \rangle = 3 \text{ m/s}$  in (b)]

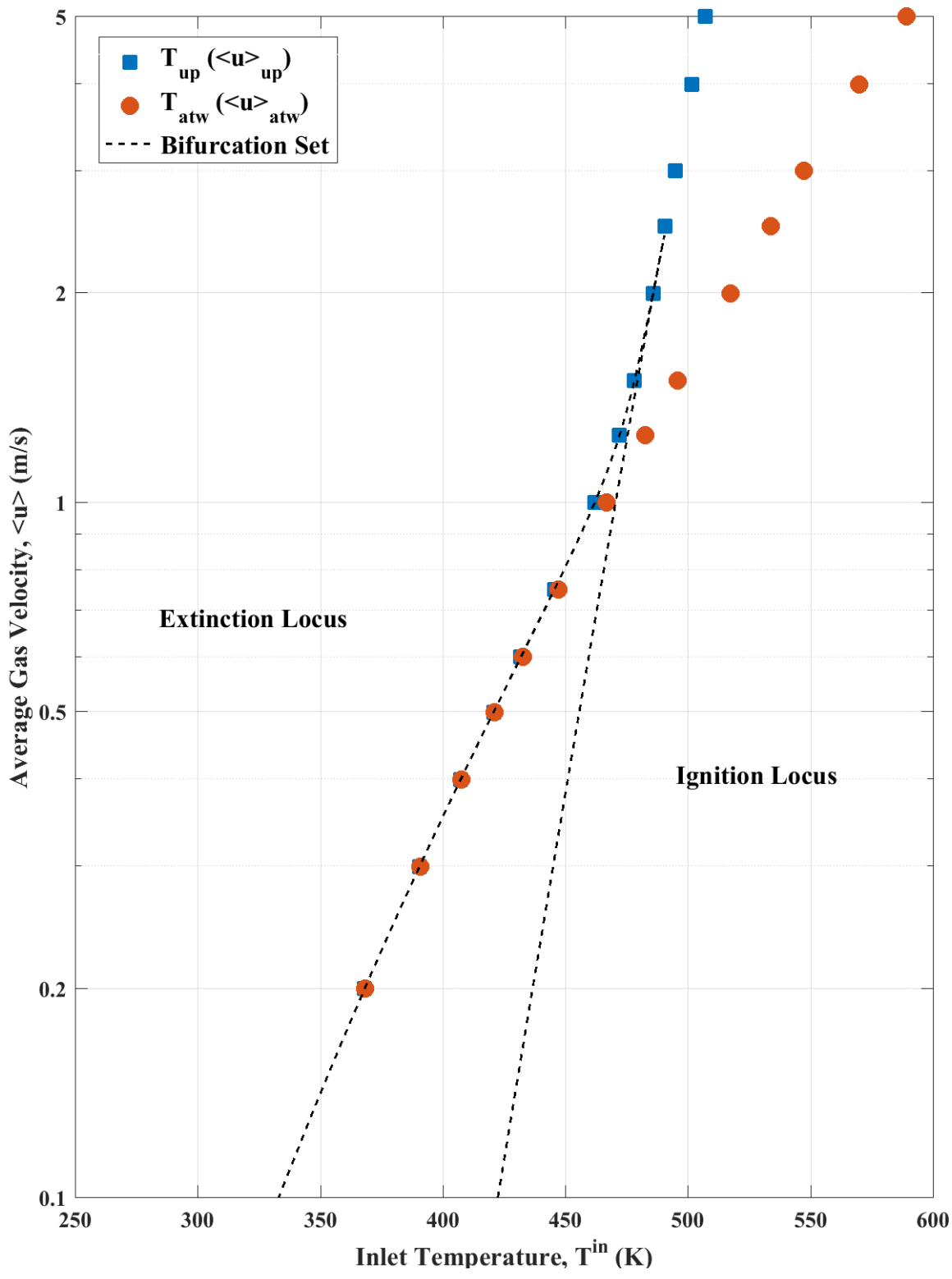


Figure 8.11: Plot of critical points and the bifurcation set. [ $\Delta T_{ad} = 238$  K]

accurately for smaller  $B$ ,

$$(B - 1) Da = 1. \quad (8.4)$$

Using Eq. 8.3 and 8.4, we can develop criteria for upstream creeping reaction zones. As discussed earlier, the critical values for the reaction zone to creep upstream follows the extinction locus in the multiple solution region and continues the ignition locus in the unique solution region, thus

$$\begin{cases} \frac{Da}{Pe_h} e^{0.4B+1.8} > 1 & Pe_h < \frac{e^{0.4B+1.8}}{B-1} \\ (B - 1) Da > 1 & Pe_h \geq \frac{e^{0.4B+1.8}}{B-1} \end{cases}. \quad (8.5)$$

As shown in Fig. 8.12(a), Eq. 8.5 agrees with the exact numerical solutions very well reasonably well. Since  $T_{atw}$  follows the extinction locus, when the left-hand side of Eq. 8.3 is greater than unity, the reaction zone will creep to the inlet. As shown in Fig. 8.12(b), Eq. 8.3 can capture the trend of the critical values with good quantitative accuracy.

## 8.4 Correlation for Creep Velocity

The correlation proposed by Vortmeyer and Jahnel (1972) has a form of (using the notation of this work)

$$v = -a_1 \langle u \rangle^{0.77} (C_f^{in})^{0.5} + a_2 \langle u \rangle,$$

where  $a_1$  and  $a_2$  are constants to be empirically determined.

Basing on the parametric studies and considering the function form of the criteria, we developed an correlation for the creep velocity,

$$\frac{v}{\langle u \rangle} = \frac{0.64}{\sigma} \left[ 1 - \left( \frac{Da}{Pe_h} e^{0.4B+1.8} \right)^{0.25} \right]. \quad (8.6)$$

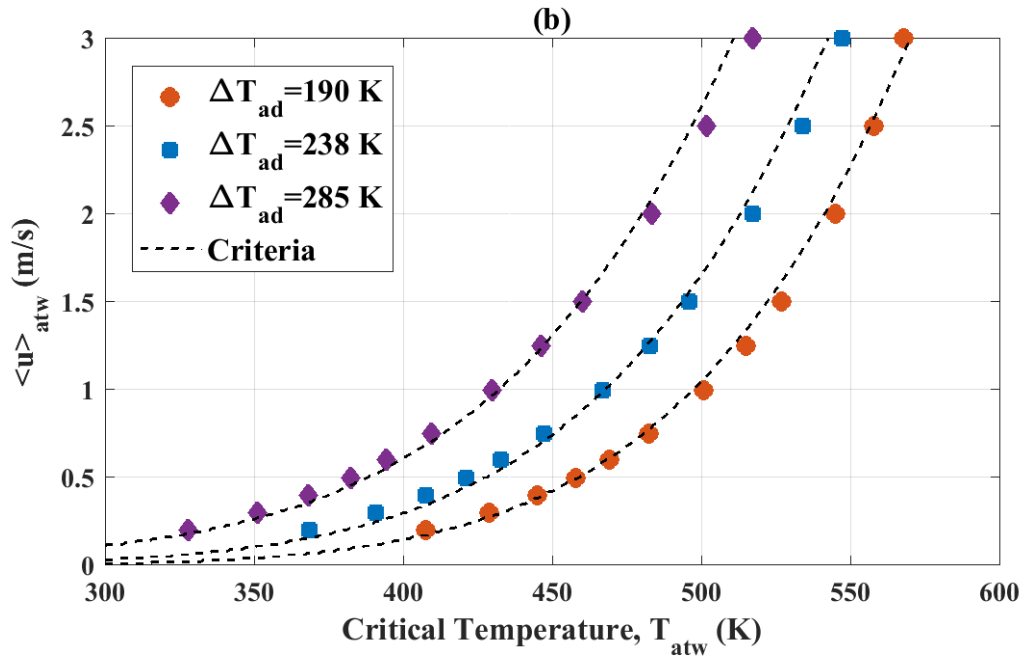
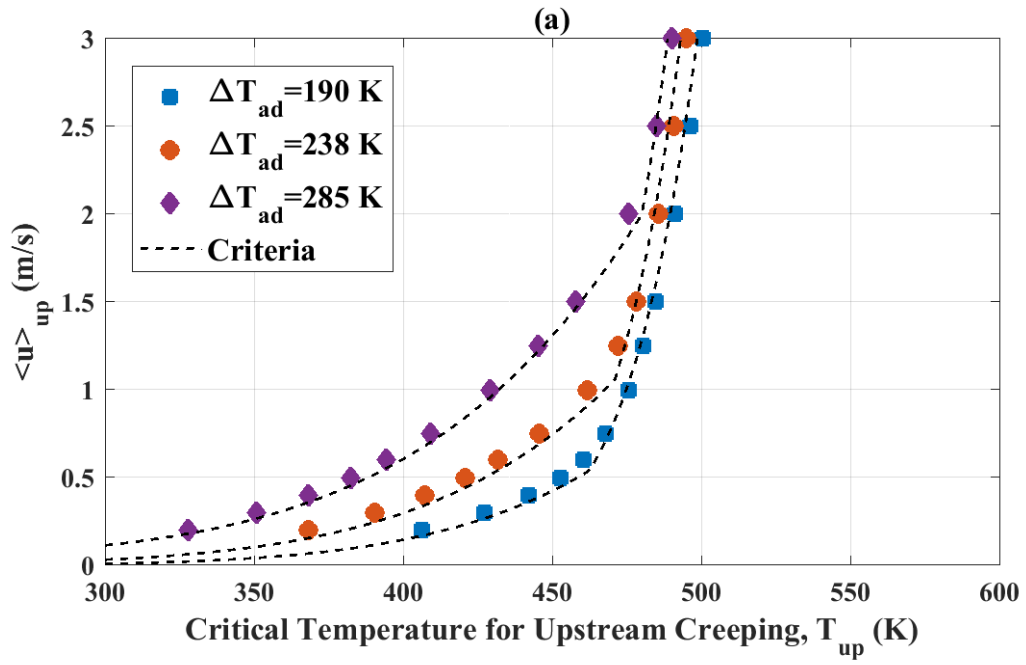


Figure 8.12: Plot of critical points where the reaction zone creeps (a) upstream or (b) all the way to the inlet.

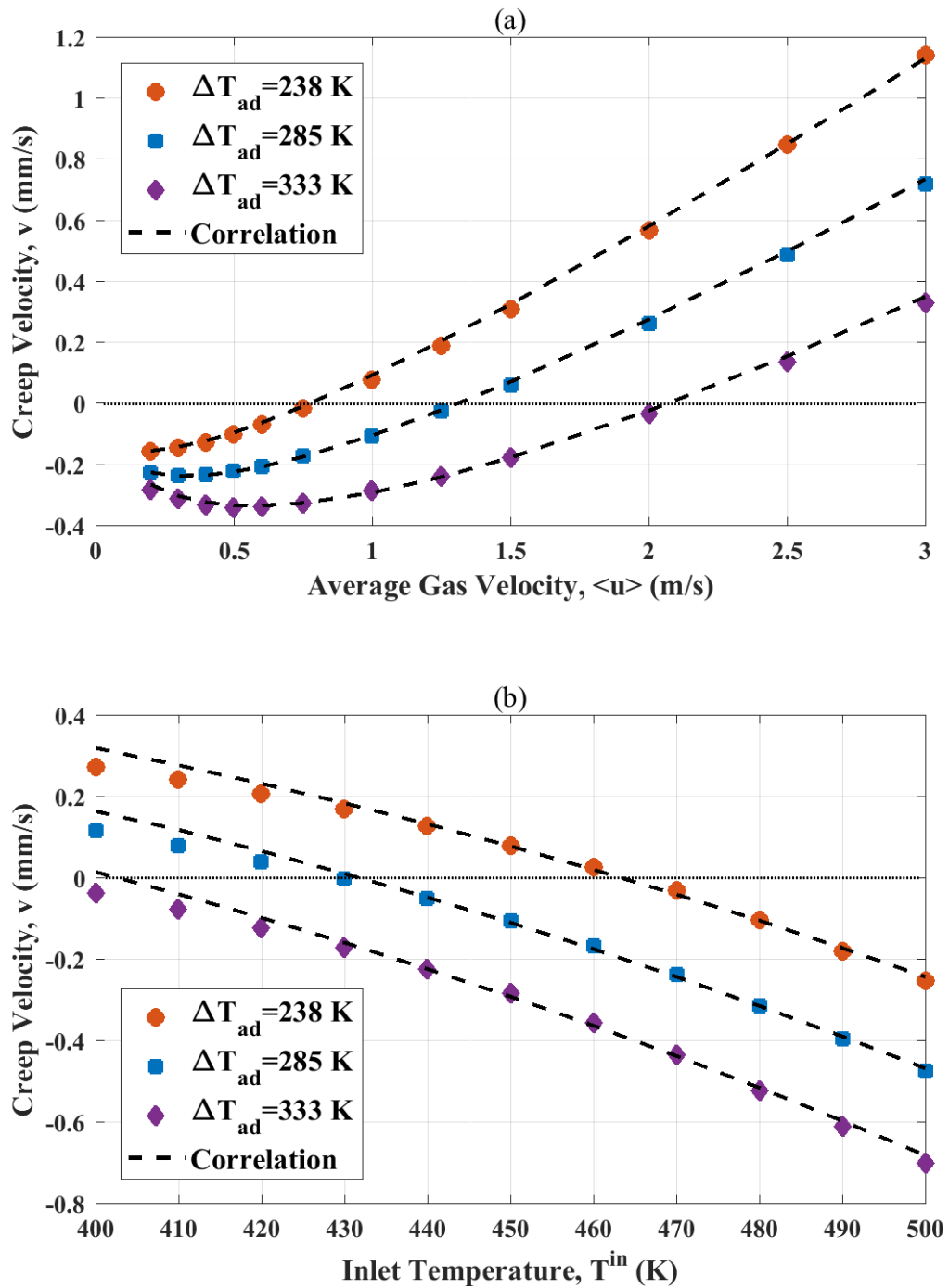


Figure 8.13: Validation of the correlation.

It is easy to verify that this correlation is consistent with the criteria proposed in the previous section (Eq. 8.3). To compare with the correlation by Vortmeyer and Jahnel (1972), Eq. 8.6 can be written as  $v = -b_1^{0.5} \langle u \rangle e^{b_2 C_f^{in}} + b_3 \langle u \rangle$ , where the exponent in the first term is 0.5 instead of 0.77 and the dependence on inlet concentration is exponential. More importantly, Eq. 8.6 includes the influences of various design parameters through the dimensionless groups ( $\sigma$ ,  $Da$ ,  $Pe_h$ ,  $B$ ). As shown in Fig. 8.13, Eq. 8.6 not only captures the qualitative trend of the creep velocity in Fig. 8.4, but also has a very good quantitative accuracy. In Fig. 8.14, we summarize all results with first-order reaction in 8.2 and compare with the predictions from Eq. 8.6 with satisfactory agreement.

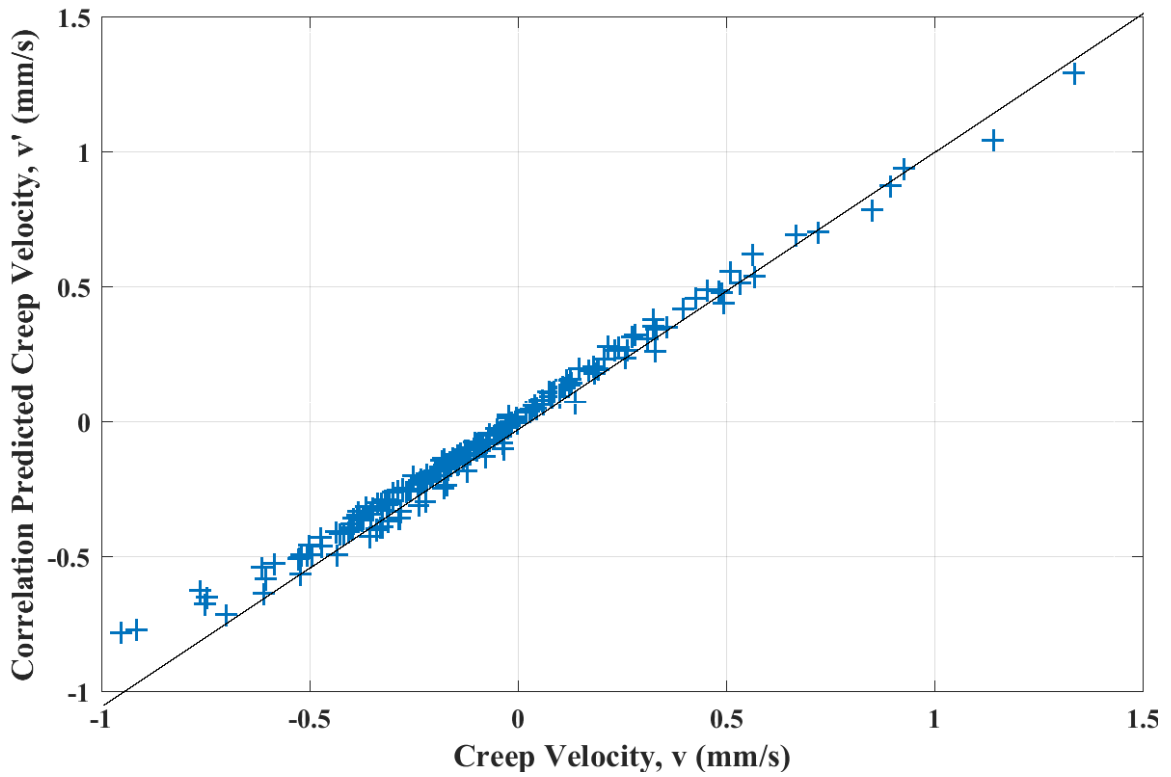


Figure 8.14: Comparison of correlation predicted creep velocity with exact numerical results.

## 8.5 Summary

In this part, the upstream creeping reaction zone is investigated in detail using a modeling approach. In the pseudo-homogeneous or kinetics controlled limit, the effects of various design parameters (including solid thermal conductivity, heat capacity, substrate material and reactor length) and operating conditions (gas velocity, inlet temperature and concentrations) on the creep velocity are determined and summarized as a correlation. Based on simulation results, we also proposed analytical criteria on whether the reaction zone will propagate upstream or downstream, whether creep all the way to the inlet or stop in the middle of the reactor. These criteria and correlation have good agreement with the numerical solutions and can provide guidance for both design and control of catalytic after-treatment systems.

# Chapter 9

## Conclusions and Recommendations for Future Work

### 9.1 Conclusions

The main contributions of this work are the development of physics-based models for catalytic monolith reactors and the detailed analysis of three important spatio-temporal dynamics of the reactors:

In the first part, a reduced order seven partial differential equation model is developed for describing the spatio-temporal dynamics of oxygen storage and release as well as the cold-start behavior of a three-way catalytic converter. The model is validated using emissions data collected in a vehicle over multiple drive cycles including FTP cycles. The internal mass transfer approximation is confirmed by comparing with a detailed washcoat diffusion–reaction model and is observed to be consistent for all practical purposes. This model extends the 0-D model of Kumar et al. (2012) by including the axial variations. As shown in this work, axial gradients in the temperature and stored oxygen profile cannot be neglected during cold start, fast lean to rich cycling or sudden and significant changes in the inlet conditions to the TWC. The differences between the behaviors of the 0-D and 1-D model is usually *qualitative* in such cases.

In the second part, we investigated in detail three main reasons causing different dynamic behaviors in lab- and full-scale monolith reactors: mass dispersion, heat conduction and heat loss. Correspondingly, three dimensionless groups ( $Pe_m$ ,  $Pe_h$

and  $\alpha$ ) determine the conditions for similarity. The common practice is such that the conditions for similarity are not satisfied in most cases, and the difference between lab- and full-scale systems can be *qualitative*. While it is possible to design laboratory reactors such that similarity conditions exist between the two systems, this could make the laboratory experiments somewhat expensive (in terms of consumption of synthetic gases used, amount of catalyst and other resources used). Thus, our view is that it is best to use laboratory experiments to study the kinetics of reactions, evaluate various catalyst formulations, determine reaction mechanisms and so forth. The kinetic models determined from laboratory scale experiments can be combined with estimated (and calibrated) heat and mass transfer parameters to simulate the full scale system, and assess the impact of scale-up on reactor performance.

In the third part, the upstream creeping reaction zone in monolith reactors is studied. Using a modeling approach, the creep velocity is calculated under different operating conditions with different design parameters. From the parametric studies correlations for the creep velocity are summarized. Basing on the relation between dynamic and steady-state behaviors of the reactor, theoretical results from bifurcation studies and numerical solutions are used to develop semi-empirical criteria for the reaction zone to start creeping upstream and for the reaction zone to creep all the way to the inlet. These correlations and criteria can help understand how individual operating conditions and design parameters influence the upstream creeping reaction zone, thus provide guidance for both design and control of catalytic monolith reactors.

## 9.2 Recommendations for Future Work

In practical applications, the states and dynamics of the after-treatment reactors cannot be measured directly. Instead, a downstream sensor is installed to monitor the reactor behaviors. For example, in order to maintain the oxygen storage level of

TWCs, a switch type sensor (HEGO) is used to monitor oxidant breakthrough. Thus it is important to understand how dynamics of the TWC can interact with the HEGO sensor and influence the sensor voltages. The chemical reactions on HEGO sensor are diffusion controlled once the sensor is heated. Since  $H_2$  has a much larger molecular diffusivity than other major species such as  $O_2$  and  $CO$ , it can create a strong offset on the switching point of HEGO sensors. The current simplified TWC kinetics can well capture the oxygen storage and release in the reactor as well as lumped emission breakthrough. However, since  $H_2$  and  $CO$  are lumped as total reductant, the kinetic model cannot predict  $H_2$  breakthrough and will not be compatible with physics-based HEGO models. Thus, a more detailed kinetic model including reactions that can change  $CO/H_2$  ratio (e.g., water-gas shift and steam reforming) is needed. Then an integrated system of engine model/map, TWC model and HEGO model can be obtained to help improve the fueling control to achieve high gas mileage and low emissions.

Our analysis in this work dealt mostly with monolith reactors used in after-treatment systems. However, the scale-up principles elucidated here may potentially be applied for another very common case, namely that of packed-bed catalytic reactors. Here again, similarity may not exist even when one uses the same catalyst composition, particle size and space velocity. The main difference between the monolith and packed-bed reactors is that in the heat and mass transfer correlations used (and hence the formulas for the various effective Péclet numbers). Thus, the main conclusions of this work on scale-up are also applicable to packed-bed as well as other structured catalytic reactors.

In this work, we only examined the pseudo-homogeneous or kinetics controlled limit. While the existence of interphase and washcoat diffusion limitations does not influence the axial conduction, it does strongly inhibit the reaction rates and hence the heat generation rates. During a cold-start, the exhaust after-treatment reactor

may start in the kinetics controlled regime and end up in the internal or external mass transfer controlled regimes. Thus, a thorough analysis and parametric study of creep velocity in different regimes using the two-phase model with washcoat diffusion is needed.

# References

1. Auckenthaler, T. S., Onder, C. H., Geering, H. P., Frauhammer, J. (2004). Modeling of a three-way catalytic converter with respect to fast transients of  $\lambda$ -sensor relevant exhaust gas components. *Ind. Eng. Chem. Res.* 43(16), 4780-4788.
2. Balakotaiah, V. (1996). Structural stability of nonlinear convection-reaction models. *Chem. Eng. Educ.* 30, 234-239.
3. Balakotaiah, V. (2008). On the relationship between Aris and Sherwood numbers and friction and effectiveness factors. *Chem. Eng. Sci.* 63(24), 5802-5812.
4. Bhattacharya, M., Harold, M. P., Balakotaiah, V. (2004). Shape normalization for catalytic monoliths. *Chem. Eng. Sci.* 59(18), 3737-3766.
5. CEPA (California Environmental Protection Agency) (2011). Low-Emission vehicle regulations and test procedures.
6. Eigenberger, G. (1972). On the dynamic behavior of the catalytic fixed-bed reactor in the region of multiple steady states—II. The influence of the boundary conditions in the catalyst phase. *Chem. Eng. Sci.* 27(11), 1917-1924.
7. Chicago
8. Etheridge, J. E., Watling, T. C. (2015). Is reactor light-off data sufficiently discriminating between kinetic parameters to be used for developing kinetic models of automotive exhaust aftertreatment catalysts? The effect of hysteresis induced by strong self inhibition. *Chem. Eng. J.* 264, 376-388.
9. Fogler, H. S. (2005). *Elements of Chemical Reaction Engineering*, fourth ed., Prentice Hall, Upper Saddle River, NJ.

10. Froment, G. F., Bischoff, K. B., De Wilde, J. (2010). *Chemical Reactor Analysis and Design*, third ed., Wiley, New York.
11. Gatica, J. E., Puszynski, J., Hlavacek, V. (1987). Reaction front propagation in nonadiabatic exothermic reaction flow systems. *AIChE J.* 33(5), 819-833.
12. Gundlapally, S. R., Balakotaiah, V. (2011). Heat and mass transfer correlations and bifurcation analysis of catalytic monoliths with developing flows. *Chem. Eng. Sci.* 66(9), 1879-1892.
13. Gundlapally, S. R., Balakotaiah, V. (2013). Analysis of the effect of substrate material on the steady-state and transient performance of monolith reactors. *Chem. Eng. Sci.* 92, 198-210.
14. Hlavacek, V., Hofmann, H. (1970). Modeling of chemical reactors—XVI Steady state axial heat and mass transfer in tubular reactors An analysis of the uniqueness of solutions. *Chem. Eng. Sci.* 25(1), 173-185.
15. Heck, R. M., Farrauto, R. J., Gulati, S. T. (2009). *Catalytic Air Pollution Control: Commercial Technology*, third ed., Wiley, New York.
16. Heywood, J. B. (1988). *Internal Combustion Engine Fundamentals*. McGraw-Hill, Inc., New York.
17. Johnson, T. (2014). Vehicular emissions in review. *SAE Int. J. Engines* 7(2014-01-1491), 1207-1227.
18. Joshi, S. Y., Harold, M. P., Balakotaiah, V. (2010). Overall mass transfer coefficients and controlling regimes in catalytic monoliths. *Chem. Eng. Sci.* 65(5), 1729-1747.
19. Kumar, P., Makki, I., Kerns, J., Grigoriadis, K., Franchek, M., Balakotaiah, V. (2012). A low-dimensional model for describing the oxygen storage capacity

- and transient behavior of a three-way catalytic converter. *Chem. Eng. Sci.* 73, 373-387.
20. Kumar, P., Gu, T., Grigoriadis, K., Franchek, M., Balakotaiah, V. (2014). Spatio-temporal dynamics of oxygen storage and release in a three-way catalytic converter. *Chem. Eng. Sci.* 111, 180-190.
  21. Levenspiel, O. (1998). *Chemical Reaction Engineering*, third ed., Wiley, New York.
  22. Luss, D., Balakotaiah, V. (1984). Steady-state multiplicity features of chemical reactors. In *Frontiers in Chemical Reaction Engineering* (Vol. 1, pp. 66-84). Wiley New Delhi.
  23. Matros, Y. S. (1985). *Unsteady Processes in Catalytic Reactors*, Elsevier, Amsterdam.
  24. Mehta, P. S., Sams, W. N., Luss, D. (1981). Wrong-way behavior of packed-bed reactors: 1. The pseudo-homogeneous model. *AIChE J.* 27(2), 234-246.
  25. Oh, S. H., Cavendish, J. C. (1982). Transients of monolithic catalytic converters. Response to step changes in feedstream temperature as related to controlling automobile emissions. *Ind. Eng. Chem. Prod. Res. Dev.* 21(1), 29-37.
  26. Olsson, L., Blint, R. J., Fridell, E. (2005). Global kinetic model for lean NOx traps. *Ind. Eng. Chem. Res.* 44(9), 3021-3032.
  27. Prikhodko, V. Y., Nguyen, K., Choi, J. S., Daw, C. S. (2009). Axial length effects on Lean NOx Trap performance. *Appl. Catal. B: Environ.* 92(1), 9-16.
  28. Puszynski, J., Hlavacek, V. (1980). Experimental study of traveling waves in nonadiabatic fixed bed reactors for the oxidation of carbon monoxide. *Chem.*

- Eng. Sci.* 35(8), 1769-1774.
29. Ramanathan, K., Balakotaiah, V., West, D. H. (2003). Light-off criterion and transient analysis of catalytic monoliths. *Chem. Eng. Sci.* 58(8), 1381-1405.
  30. Rhee, H. K., Foley, D., Amundson, N. R. (1973). Creeping reaction zone in a catalytic, fixed-bed reactor: a cell model approach. *Chem. Eng. Sci.* 28(2), 607-615.
  31. Rhee, H. K., Amundson, N. R. (1974). Equilibrium theory of creeping profiles in fixed-bed catalytic reactors. *Ind. Eng. Chem. Fundam.* 13(1), 1-4.
  32. Rhee, H. K., Lewis, R. P., Amundson, N. R. (1974). Creeping profiles in catalytic fixed bed reactors. Continuous models. *Ind. Eng. Chem. Fundam.* 13(4), 317-323.
  33. Salomons, S., Hayes, R. E., Votsmeier, M., Drochner, A., Vogel, H., Malmberg, S., Gieshoff, J. (2007). On the use of mechanistic CO oxidation models with a platinum monolith catalyst. *Appl. Catal. B: Environ.* 70(1), 305-313.
  34. Siemund, S., Leclerc, J. P., Schweich, D., Prigent, M., Castagna, F. (1996). Three-way monolithic converter: simulations versus experiments. *Chem. Eng. Sci.* 51(15), 3709-3720.
  35. Subramanian, S., Balakotaiah, V. (1996). Classification of steady-state and dynamic behavior of distributed reactor models. *Chem. Eng. Sci.* 51(3), 401-421.
  36. Voltz, S. E., Morgan, C. R., Liederman, D., Jacob, S. M. (1973). Kinetic study of carbon monoxide and propylene oxidation on platinum catalysts. *Ind. Eng. Chem. Prod. Res. Dev.* 12(4), 294-301.

37. Vortmeyer, D., Jahnelt, W. (1972). Moving reaction zones in fixed bed reactors under the influence of various parameters. *Chem. Eng. Sci.* 27(8), 1485-1496.
38. Yakhnin, V., Menzinger, M. (2002). Stationary and traveling hot spots in the catalytic combustion of hydrogen in monoliths. *Chem. Eng. Sci.* 57(21), 4559-4567.
39. Yu, M., Luss, D., Balakotaiah, V. (2013). Analysis of flow distribution and heat transfer in a diesel particulate filter. *Chem. Eng. J.* 226, 68-78.
40. Wicke, E., Vortmeyer, D. (1959). Zündzonen heterogener Reaktionen in gasdurchströmten Körnerschichten, *Ber. Bunsenges. physik. Chemie* 63(1) 145-152.
41. Zlokarnik, M. (2002). *Scale-up in Chemical Engineering*, Wiley VCH, Weinheim.